Temporal phase and amplitude statistics in coherent radiation

Dean Wright, MSci.

Thesis submitted to the University of Nottingham
for the degree of Doctor of Philosophy

February 2005

Contents.

1. Introduction 6

1.1. An introduction to Gaussian noise. 11
1.2. Introduction to the intensity-weighted phase derivative. 14

2. Computer simulation method

2.1. Underlying theory. 18
2.1.1. The wave equation. 18
2.1.2. The paraxial approximation to (2.3) and solution. 19
2.2. The phase screen technique. 21
2.2.1. Statistics of the phase screen, the Gaussian noise model. 23
2.2.2. The Kolmogorov theory of turbulence. 24
2.2.3. The phase spectrum $\Phi_\phi(\kappa)$. 27
2.3. The simulation technique. 32
2.4. Simulation parameters. 35
2.5. Validation of the simulation technique. 36
2.5.1. Regimes of propagation, Fresnel, focussing and Fraunhofer regimes. 37
2.5.2. Scintillation index curves for Gaussian correlated phase screens. 41
2.5.3. Second order intensity-weighted phase derivative statistics using a Gaussian correlated phase screen. 44
2.6. Conclusions. 47

3. The intensity-weighted phase derivative in a Rician field 49

3.1. Statistical properties of *J* in a Rician field. 50
3.1.1. The pdf of the intensity-weighted phase derivative in a Rician field. 50
3.1.2. Calculation for the characteristic function for the *J* statistic in a Rician field. 55
3.1.3. Comparison of theory with phase screen simulation. 58
3.1.4. Conclusions. 59
3.2. The correlation function of the phase derivative in a Rician field. 60
3.2.1. Analysis. 60
3.2.2. Investigation of $\Omega'(\tau')$ for larger values of ϕ_0. 64
3.2.3. Limit for $\Omega'(\tau')$ as $\tau' \to 0$ for large ϕ_0. 67
3.2.4. Numerical simulation of $\Omega'(\tau')$. 67
3.2.5. Concluding remarks. 70
3.3. Calculation of the second moment of J for a plane wave propagating through a single weak corrugated phase screen. 71
3.3.1. Normalised second moment of *J* for all *z*. 72
3.3.2. Computer simulation. 75
3.3.3. Conclusions. 77

3.4. Conclusions. 77

4. Phase power spectra, 2D models 79

4.1. PPS for propagation through a single, weak, corrugated phase screen. 80
4.1.1. Analysis. 80
4.1.2. Computer simulation. 83
4.1.3. Conclusions. 87
4.2. PPS for propagation through an extended medium, multiple, weak, corrugated phase screens. 87
4.2.1. An overview of Clifford's extended medium theory. 89
4.2.2. Simulation of an extended medium with weak turbulence. 91
4.2.3. Results of simulations. 93
4.2.4. Conclusions. 97
4.3. Propagation problems using stronger turbulence levels in 2D. 98
4.3.1. PPS for propagation through a single, strongly turbulent, corrugated phase screen. 99
4.3.2. PPS for propagation through an extended medium, strong turbulence. 108
4.4. Conclusions. 112

5. LIDAR systems and 3D simulation techniques 114

5.1. Three dimensional simulations in contrast to two dimensions. 115
5.2. Three dimensional simulations, plane waves and extended media. 117
5.3. Beams solutions to the paraxial equation. 120
5.3.1. Beam spreading and wander. 122
5.3.2. Numerical simulations, spreading and wander. 123
5.4. Temporal phase statistics in 3-dimensional simulations. 127
5.4.1. Use of rectangular phase screens in temporal phase statistics. 128
5.5. An alternative to the Kolmogorov pure power law; subharmonics. 130
5.6. Temporal phase spectra, analysis. 136
5.6.1. Beam analysis. 136
5.6.2. Spherical wave analysis. 138
5.7. Simulation results. 141
5.7.1. Plane waves, pure power law spectra. 141
5.7.2. Plane waves, Tatarski spectra. 143
5.7.3. Gaussian Beams, pure power law spectrum. 145
5.7.4. Beam waves, Tatarski spectrum. 147
5.7.5. Gaussian beams in a single phase screen limit. 150
5.8. Experimental work. 154
5.8.1. Intermediate / weak turbulence, 10/02/2003. 155
5.8.2. Strong turbulence, 23 January 2003. 158
5.8.3. Phase power spectra. 161
5.8.4. Conclusions. 163

5.9. Conclusions to chapter 5 164

6. Conclusions 169

Appendix A 172

Appendix B 174

Appendix C 175

References. 176

Abstract.

Interest in coherent remote sensing systems has stimulated investigations in the properties laser propagation through extended atmospheric turbulence. This thesis investigates the statistics of phase, and phase related, observables using analytical and computational techniques, together with experimental results.

The phase screen technique is used to simulate perturbations to the refractive index of a medium through which the radiation propagates. Several different turbulence models (Gaussian correlated noise, Kolmogorov turbulence, Tatarski and Von Karman spectral models) are investigated, and their relative merits for describing experimental conditions and descriptive statistical measures are compared and contrasted.

The phase power spectrum is crucial to an understanding of the practical operation of a coherent imaging system, and later part of the thesis is devoted to the investigation of a LIDAR system in particular. Several turbulence regimes are investigated, from an analytical treatment of a weakly turbulent, extended atmosphere, to large 3D computations designed to simulate experimental arrangements. The 3D simulation technique presented herein has been developed to allow for the investigation of temporal statistics. New power law behaviours are found to appear in temporal frequency spectra which differ from the -8/3 power law form that has been accepted in much of the literature. Strongly turbulent regimes result in a -2 power law while the use of a Gaussian beam profile in an extended medium gives a -11/3 power law under weak turbulence conditions.

1. Introduction

The propagation and interference of electromagnetic waves passing through the atmosphere has long been a key area of research in the field of signals processing [1]. This research has principally been directed towards understanding the origins and size of intensity scintillations in a beam [2, 3, 4, 24 and references therein], because many communications and remote detection systems rely only on variations in the amplitude of the wave to provide useful information [1, 5]. It is sometimes the case though that phase information is required in addition to intensity fluctuations; this is often true in communications systems where frequency demodulation is a principal method for transmitting the signal. This is especially important when the radiation source is coherent (i.e. a laser) [6, 26, 42 and 31] and the received phase can be compared to the initially coherent wave front. The phase screen method is a technique which is used to simulate coherent radiation propagation by using an infinitesimally thin screen to model the effects of turbulence induced fluctuations into the phase (but not the amplitude) of the radiation. Phase fluctuations introduced into the field before propagation are intended to simulate the effect of temperature, and thereby refractive index, fluctuations and motion of the air. The statistical properties of the phase screens are used to characterise the type of turbulence being modelled. Propagation of the field after interaction with the screen then allows intensity fluctuations to build up through diffraction; focusing and caustics in the field arise through propagation. The statistical properties of the intensity and phase statistics are closely related to the statistics of the screen itself. The theoretical development of the phase screen technique, as well as its analytical and numerical applications, will be discussed in chapter 2.

The pioneers of the phase screen method [2, 3] were largely interested in the calculation of intensity statistics for coherent waves passing through idealised phase-changing screens. Indeed these statistics are still of current interest [8, 9]. These studies used Gaussian complex processes to model atmospheric noise; they argue further that this noise be characterised by a Gaussian auto-correlation function. An important focus of these pioneering studies was radio-wave scintillations [2] and light initiating from interstellar sources [48, 49, 10]. A interstellar source can be

considered coherent because of the vast distances between an Earth-bound observer and the stellar object. The calculation of the intensity scintillation curve (σ_I, the second moment of the intensity normalised by the square of the mean) for an idealised Gaussian correlated phase screen in one dimension, obtained by Mercier [3], shows how intensity fluctuations develop over different ranges of propagation. Mercier and Bramley [11, 50] both used approximations to Helmholtz's formula for wave diffraction, they used simple perturbation theory to predict a form for the intensity statistics in regimes characterised by weak turbulence (i.e. weak phase screens). These results predict a reduction to Gaussian statistics with properties as investigated by Rayleigh [12] and Rice [13] at large propagation distances.

Rice [13] investigated the properties of what has become known as the Rician field, which is a field consisting of a constant phasor plus Gaussian noise. It shall be seen, in chapter 3, that the Rician field forms a useful model for a propagated field in the Fraunhofer zone, i.e. in the far field, under certain propagation conditions. The constant phasor represents an unperturbed part of the plane wave while the Gaussian process represents the part of the wave perturbed by propagation beyond the phase screen.

Further work on the form of intensity scintillation curves by Jakeman and McWhirter [4] investigated the effects of different kinds of 'deep' phase screens, i.e. strong scattering, in one dimension. The statistical properties of the diffracted field are characterised by the correlation properties of the screens. Several different autocorrelation functions were considered; they showed the existence of a strong focusing region (including a peak in the scintillation index such that $\sigma_I > 2$) at intermediate propagation distances and a saturated Gaussian speckle regime (where the scintillation index $\sigma_I = 2$) beyond that, in accordance with Mercier's [3] results. This is an important result which is used in benchmarking the numerical simulation technique in chapter 2.

Attempts were made by Buckley [14] to derive a full probability distribution for the complex electromagnetic field beyond an exponentially correlated phase screen. The exponential correlation gives a fractal quality to the phase screens which can be seen

in atmospheric propagations. This 'fractal' quality manifests itself as a self-similar appearance in the resulting intensity images (see figures 2.5 and 2.6). This approach considered plane-wave illumination of a screen and resulted in the required probability distribution being obtained from the solution to a Fokker-Plank equation for the Fourier transform of the complex field. The results are analytically and numerically formidable, and have not provided much insight into the problem.

Theoretical work that produces usable results is often restricted to simple perturbation methods or an assumption of far field. It can be shown (section 2.1) that Maxwell's laws for the behaviour of electromagnetic field yield a wave equation describing the propagation of E/M waves. Assuming short wavelengths the equation is reduced to a simpler form:

$$\nabla^2 U + k^2 n^2(r) U = 0 \qquad (1.1)$$

such that U is a scalar representing a component of the field. A perturbation method can be used to solve equation (1.1). The Born approximation, $U = U_0 + U_1 + U_2 \ldots$, where $U_i >> U_{i+1}$, is used as a simple additive perturbation to the field. The Rytov approximation, $U = U_0 \exp(\Psi)$ where $\Psi = \Psi_1 + \Psi_2 + \ldots$ and $\Psi_i >> \Psi_{i+1}$, is a multiplicative perturbation technique used on the phase. Both these approximations require weak turbulence conditions. Under the Born approximation a system of equations is obtained that can each be solved by the use of a Green's function method, i.e.

$$U_m(r) = 2k^2 \int_{all\ s} G(r,s) n_1(s) U_{m-1}(s) d^3 s \qquad (1.2)$$

where $G(r,s)$ is the free-space Green's function. Second order moments are defined under the Rytov approximation in terms of Ψ_1 and Ψ_2:

$$E_1(r) = \langle \Psi_2(r,L) \rangle + \frac{1}{2}\langle \Psi_1^2(r,L) \rangle$$
$$E_2(r_1,r_2) = \langle \Psi_1(r_1,L)\Psi_1^*(r_2,L) \rangle \quad . \qquad (1.3)$$
$$E_3(r_1,r_2) = \langle \Psi_1(r_1,L)\Psi_1(r_2,L) \rangle$$

From these one can form linear combinations which give all the moments of interest in laser propagation problems [38].

A similar perturbation method can be applied to the amplitude and phase of the wave, i.e. instead of applying perturbations to the field *U*, write $U = A\exp(iS)$ and approximate $S = S_0 + S_1 + ...$ and $\log A = \log A_0 + \chi$. This geometric optics formulation is considered in more detail in section 2.2.3 where it is used to derive a useful result. Ishimaru [72] also used this method to derive an important result for phase spectra; this is considered in more detail in chapter 5.

In the light of this failure to obtain significant results for the statistics of a propagated field in anything other than the simplest of cases, attention has shifted to numerical simulation. The term 'numerical simulation' is understood to mean the stochastic modelling of the wave propagation as opposed to numerical solution of the governing equations. In an early paper on the numerical simulation of wave propagation through phase screens, Buckley [57] discusses the theoretical basis behind the use of phase screens and why one should expect good results from simulation. He provides simulation results in the form of probability density functions, moments and power spectra for the intensity. Whale [56] performs a similar analysis, looking at anisotropic (i.e. where the correlation length is dependent upon the direction) screens. He performs some simple calculations concluding that analytical results involving strong levels of turbulence are difficult to produce and that the study of the intensity scintillation index is important in investigating such regimes. A similarly complete analysis of the theory behind wave propagation exists in a paper published by Prokhorov et al. [42] where the paraxial approximation is discussed (section 2.1.2) and the spreading and wander of a propagated beam considered.

Simulations have been performed using one-dimensional screens (i.e. a two-dimensional simulation) [16] and two-dimensional screens [8, 15 and many more] (three-dimensional simulation). Macaskill and Ewart's paper [19], comparing forward difference methods and fast Fourier transform (FFT) methods for beam propagation, provides a theoretical basis for the use of the FFT method in simulation. Much work has also been directed at atmospheric turbulence and the development of credible methods for simulating it [27, 28, and 29]. Ways that one can numerically model this turbulence through the use of phase screens have been examined by several authors [20, 23]. Lane, Glindemann and Dainty [20] considered the simulation of a pure power law spectrum at small frequencies in an attempt to solve difficulties in the discrete sampling of such spectra, these ideas shall be discussed in greater detail in chapter 5. Frehlich [23] investigated the simulation of a Kolmogorov spectrum[1] for very strong propagation regimes, he used an extension of the method presented by Lane et al. with the goal of introducing a new FFT algorithm.

The main thrust of investigation into intensity scintillations in recent years has involved the use of faster and more powerful computers to make predictions about results that do not yield to analytical treatment. There has also been greater concentration on the use of two-dimensional screens (i.e. simulations that model a full three-dimensional situation). Studies by Martin, Flatte and Gerber [8, 15, 27] have investigated the possibility of using simulations in this way. These methods also allow relatively quick and easy investigation of different types of phase screens and beam profiles. One of the questions currently under debate in the literature is the relative merits of using single and multiple phase screens. The single screen method has been shown to be valid under certain conditions [62], while its validity has been questioned under others [61] where the extended medium gives different results (see section 4.2 for a more detailed discussion).

More recently, interest has focused on the intensity weighted phase statistic [16, 21], an increasingly important measure in the field of laser communications. This interest is a result of current research into the use of phase statistics. The development of heterodyne detection systems (see chapter 5), where a local oscillator is used for

[1] See section 2.2.2 for a description of the Kolmogorov theory of turbulence.

comparison with a received signal, allows for the practical use of phase statistics in remote detection systems. In this case the laser comes into its own; part of the power of the coherent wave front can be diverted to setting up a frequency-shifted reference signal in the lab to serve as a local oscillator. Systems using incoherent beams (direct detection) are only able to measure intensity statistics.

The phase derivative and phase spectrum allow the use of phase statistics. Both these methods are investigated in the chapters that follow. Chapters 4 and 5 look at the numerical modelling of phase spectra. Work on the properties of phase statistics in propagated laser beams has not been extensively developed since early work performed by Clifford [30] and Ishimaru [70, 71, 72] in the 1970s. In those studies the properties of the phase power spectrum were investigated for several beam profiles in weak scattering regimes.

The focus of this thesis is a broad investigation of the properties of phase and phase derivative statistics in coherent radiation propagation. Work is presented that concentrates on computer simulation and analysis of phase and phase derivative statistics.

1.1. An introduction to Gaussian noise.

The concept of Gaussian noise was alluded to first by Lord Rayleigh [12] in his celebrated work of 1880. This work was carried out in response to the work of Verdet [reference within 12] and looked at the expected resultant of a large number of constant phasors with arbitrary phase. Upon consideration of the probability density function, Rayleigh calculates that the pdf for the amplitude r in such a system will be proportional to $\exp(-r^2)$.

Noise in a system that arises as a result of such a large number of independent scatterers was first noted after the advent of lasers as a coherent source of fixed-wavelength light. Experimental work showed the existence of a granular or ‘speckle’ pattern present when the beam was reflected from an apparently smooth surface. This noise is due to imperfections in the surface on a scale similar to the wavelength of the

radiation. The need to describe the speckle pattern leads to a stochastic formulation of light reflection, as an attempt to describe such a rough surface deterministically is an impossibly complex task. It is the sum of many constructive and destructive interferences from scattered waves from the surface that cause the speckle pattern. Indeed one can show that the intensities of such a sum are distributed negative exponentially while the phase is uniform over the range $\theta \in (0, 2\pi]$.

Wherever a large number of noise sources act as random phasors, one might expect to be able to characterise the noise as a Gaussian random process [64]. This arises from the central limit theorem, which states that the resultant of a large number of independent random processes, $x_i(t)$, will have Gaussian statistics. I.e, a statistic defined as $X = \frac{1}{N}\sum_{i=1}^{N} x_i$ will have mean $\langle X \rangle = \langle x_i \rangle$, variance $\sigma_X^2 = \langle x_i^2 \rangle / N$ and be distributed normally such that

$$P(X) = \frac{1}{\sigma_x \sqrt{2\pi}} \exp\left\{ -\frac{(\langle X \rangle - X)^2}{2\sigma_X^2} \right\}. \tag{1.4}$$

The resultant of multiple scatterings in an atmospheric layer can therefore be said to constitute a complex circular Gaussian process $X(t) + iY(t)$. These processes, $X(t)$ and $Y(t)$, will have Gaussian statistics as noted above. These multiple scatterers, i.e. the noise, are also characterised by an auto-correlation function $\rho(\tau) = \langle X(t)X(t+\tau) \rangle$. Gaussian noise generated randomly (by a random number generator for example) is characterised as 'white', i.e. the autocorrelation function is uniformly zero. Noise encountered in atmospheric propagation will not be white, it will have certain statistical properties, several models for which have been proposed by several groups. An overview of such models follows in the next chapter. One can impose an arbitrary autocorrelation function for the purposes of analytical work, some popular models include the Gaussian

$$\rho(\tau) \sim \exp\left(-\frac{\tau^2}{\xi^2} \right), \tag{1.5}$$

the exponential

$$\rho(\tau) \sim \exp\left(-\frac{|\tau|}{\xi}\right), \tag{1.6}$$

and the truncated parabolic

$$\rho(\tau) \sim \left\{\begin{array}{ll} 1-\frac{\tau^2}{\xi^2} & |\tau| < \xi \\ 0 & otherwise \end{array}\right\}. \tag{1.7}$$

As well as determining the properties of the auto-correlation function for the circular Gaussian process, one can derive several statistical properties of the process itself. The joint pdf for X, Y, $\dot{X}$ and $\dot{Y}$ (where the dot represents a temporal derivative)

$$P\left(X, Y, \dot{X}, \dot{Y}\right) = \frac{1}{4\pi^2 b_0 b_2} \exp\left\{-\frac{1}{2b_0 b_2}\left[b_2\left(X^2+Y^2\right)+b_0\left(\dot{X}^2+\dot{Y}^2\right)\right]\right\} \tag{1.8}$$

can be determined from a consideration of the characteristic function and used to determine the pdf for the intensity $I = X^2 + Y^2$ and the phase derivative $\dot{\theta} = \tan^{-1}(Y/X)$. Note that $b_0 = \left\langle X^2 \right\rangle$ and $b_2 = \left\langle \dot{X}^2 \right\rangle$. Assuming that the phase is distributed uniformly one can show that

$$P(I) = \frac{1}{\langle I \rangle} \exp\left\{-\frac{I}{\langle I \rangle}\right\} \tag{1.9}$$

and

$$P\left(\dot{\theta}\right) = \frac{\tau_c}{2\left(1+\tau_c^2\dot{\theta}^2\right)^{3/2}}. \tag{1.10}$$

where $\tau_c = \sqrt{b_0/b_2}$. Thus the intensity has a negative exponential distribution (as expected) while the phase derivative takes on a student-*t* distribution (equation 1.10) and exhibits a -3 power law behaviour in its tails.

1.2. Introduction to the intensity-weighted phase derivatives.

The intensity-weighted phase derivative, $J = I\dot{\theta}$ where the phase derivative is a derivative in time, was proposed [16] as a statistic that can be used in the retrieval of accurate frequency data in received, initially coherent radiation. This is especially important in LIDAR (LIght Detection And Ranging) systems. The phase derivative is a useful method for demodulating the frequency from the carrier wave in a LIDAR system, as well as having applications in chemistry [17]. These laser ranging systems will be discussed in detail in chapter 5. A received signal is written as

$$E(t) = A(t)\exp(i\theta(t) + ift), \tag{1.11}$$

where $A(t)$ is the amplitude and $\theta(t)$ a noise term introduced in to the system by the action of stochastic process in the atmosphere. Frequency information *f* is retrieved by taking the temporal derivative and averaging such that

$$\ddot{p} = \langle f \rangle + \langle \dot{\theta} \rangle. \tag{1.12}$$

The noise introduced by this phase derivative term, $\dot{\theta}$, is a zero-mean random process and so a simple average should be sufficient to filter it out and leave only the frequency information.

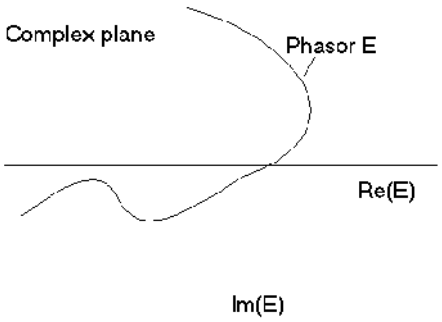

Figure 1.1: This sample phasor shows the difficulty of measuring the phase derivative. As the phasor approaches the origin in the complex plane the phase derivative increases rapidly. The amplitude is close to zero at this point, thus amplitude weighting is used.

The problem in using this simple averaging is that the phase derivative is prone to undergoing extremely large departures from zero when the phasor, representing the received field in the complex plane, approaches the origin. The phase derivative can be weighted with the amplitude in order to remove these large departures, see figure 1.1. While departures in $\dot{\theta}$ become large as the phasor approaches the origin, the value of the amplitude approaches zero and so one is assured of using a weighting that reduces fluctuations in the temporal derivative. It has been shown [16] that the most efficient means of weighting the phase derivative - where 'efficiency' is defined in terms of a minimisation of the variance of J - is by using the intensity. Thus the intensity-weighted phase derivative produces a statistic with the same features as $\dot{\theta}$ but without the same large, sudden deviations that cause problems in averaging. This use of the intensity-weighted phase derivative is discussed in greater detail in [76] with reference to a series of controlled experiments in which a thermal plume is used to crudely simulate the effects of a strongly turbulent atmosphere. Figures presented in the study show clearly how the intensity weighting improves the signal to noise ratio (SNR) of the received beam. It is noted, however, that the use of intensity weighting in a situation where the SNR is already high will not necessarily further improve accuracy.

The properties of J have been studied in some detail in the case of a circular Gaussian process [21]. Defining the field as $E = X + iY$, where X and Y are independent Gaussian processes, $I = X^2 + Y^2$ and $\dot{\theta} = \frac{d}{dt}\tan^{-1}\left(\frac{Y}{X}\right)$ results in $J = X\dot{Y} - Y\dot{X}$.

From this definition one can write down the characteristic function of *J* and thus show the probability density function to be

$$P(J) \sim \exp\left\{-\frac{2\tau_c|J|}{\langle I\rangle}\right\}, \tag{1.13}$$

where $\tau_c = \sqrt{\frac{b_0}{b_2}}$ is a parameter related to an amplitude correlation as defined above. Consider the second moment of *J*,

$$\langle J^2\rangle = \langle X^2\hat{Y}^2\rangle + \langle Y^2\hat{X}^2\rangle - 2\langle X\hat{Y}\rangle\langle Y\hat{X}\rangle. \tag{1.14}$$

noting now that as *X* and *Y* are independent Gaussian processes, $\langle X\rangle\langle Y\rangle = \langle XY\rangle = 0$, while $\langle \hat{X}^2\rangle = \langle \hat{Y}^2\rangle$, therefore

$$\langle J^2\rangle = (\langle X^2\rangle + \langle Y^2\rangle)\langle \hat{X}^2\rangle = \langle I\rangle\langle \hat{X}^2\rangle, \tag{1.15}$$

such that in the case of a plane wave, $\langle J^2\rangle = \langle \hat{X}^2\rangle$. It is also clear from this that one can write $J = \mathrm{Im}\left(E^* \frac{dE}{dt}\right)$, this expression will be used in section 3.3.

In chapter 2 several of the results of Gaussian noise theory are used to benchmark the computer simulation method. Chapter 3 considers the *J* statistic in the Rician field, i.e. a field characterised by a constant phasor plus a Gaussian process. The pdf for *J*, moments in the far field and the normalised second moment for all propagation distances *z* are derived in this general case. Two-dimensional models for phase power spectra simulations for plane waves are considered in chapter 4, while three-dimensional beam simulations are investigated in chapter 5.

2. Computer simulation method

The numerical simulation of coherent radiation propagation has become an increasingly important area of research in recent years as refinements to models for atmospheric turbulence become more difficult to treat analytically. Such refinements to turbulence models are designed to account for atmospheric effects that have been observed in experiment. When these models are defined in terms of spectral components and the required Fourier transform (the auto-correlation, required in the modelling of phase screens, function is defined as the Fourier transform of the spectrum of the turbulence) does not exist in analytical terms – it can often be hard or impossible to make progress with analytical work. Thus, the investigation of the properties of complex turbulence models lies outside the realm of analytical work, falling instead to numerical simulation. A large body of work on the statistics resulting from propagation through mathematically simple turbulence exists in the literature. It is possible to refine a numerical simulation technique by comparing analysis with numerics before investigating turbulence models that cannot be treated analytically. The computer simulation technique is therefore very important in this field; stochastic simulations are used rather than attempting a deterministic solution to the governing equations of wave propagation. This is done because the nature of turbulence is inherently random, and many of the ways in which coherent radiation is measured in experiment are statistical. It therefore makes sense to cast simulations in a stochastic form, and use statistics in the interpretation of results.

In this chapter the phase screen method is introduced, this is a technique that models atmospheric turbulence by the introduction of phase perturbations on to a coherent wave front. The technique can be used in both numerical and analytical work, and allows fluctuations in the amplitude of the beam to build up as the beam propagates. The Kolmogorov theory of turbulence is also introduced, this model uses a method of dimensional analysis to cast atmospheric turbulence in terms of a spectrum of refractive index fluctuations. Several validations of the phase screen method are also considered, using a comparison of numerical simulation results with analytical theory.

2.1. Underlying theory of wave propagation.

The numerical simulation technique involves the numerical propagation of a field through atmospheric turbulence. In order to do this, a numerical discretisation of the theory behind wave propagation is required. A model is also needed for the turbulence itself. The behaviour of electromagnetic radiation is governed by Maxwell's field equations. The phase screen model, which attempts to simulate turbulence through the use of a thin, phase-changing screen, is discussed in more detail. A discretisation of the phase screen model is also considered.

2.1.1. The wave equation.

The behaviour of an electromagnetic field ($\underline{E}$ the electric field and $\underline{B}$ the magnetic field) is described by Maxwell's field equations

$$\begin{aligned}
&\underline{\nabla}.\underline{E} = \frac{\rho}{\varepsilon_0} \\
&\underline{\nabla}.\underline{B} = 0 \\
&\underline{\nabla}\times\underline{E} = -\frac{\partial \underline{B}}{\partial t} \\
&\underline{\nabla}\times\underline{B} = \frac{1}{c^2}\frac{\partial \underline{E}}{\partial t} + \mu_0 \underline{j}
\end{aligned} \qquad (2.1)$$

where $\underline{j}$ is a free current, ρ the free charge, μ_0 and ε_0 the permeability and permittivity of magnetic and electric fields respectively. Manipulation of the third and first of the above laws leads to a wave equation describing the propagation of an electric field in a non-homogeneous medium:

$$\nabla^2 \underline{E} + \underline{\nabla}\left(\underline{E}.\underline{\nabla}\ln\xi\right) = \xi\mu\frac{\partial^2 \underline{E}}{\partial t^2}. \qquad (2.2)$$

Looking for solutions that vary sinusoidally in time (i.e. $E(\underline{r},t) = E_0(\underline{r})e^{-i\omega t}$) allows the reduction of equation (2.2) to

$$\nabla^2 \underline{E} + \underline{\nabla}(\underline{E}.\underline{\nabla} \ln n(\underline{r})) = k^2 n^2(\underline{r})\underline{E}\,. \qquad (2.3)$$

Here the refractive index $n^2 = \xi\mu$ and k is the wave number (equal to the frequency of the wave divided by its speed). This is the wave equation; it is used in the simulations in this thesis that model the propagation of a coherent radiation source. As has already been noted, the model will involve phase perturbations by a screen, the actual propagation of the wave will be through a vacuum. It is possible to reduce this equation yet further, assuming that the field is simply a propagating wave in space, and that the refractive indices for electric and magnetic propagation are constants (n = 1 in a vacuum), the spatial and temporal evolution of this wave or packet of waves is described simply by

$$\nabla^2 u + k^2 u = 0 \qquad (2.4)$$

which is the standard Helmholtz equation [31] where u is the scalar field.

2.1.2. The paraxial approximation to (2.3) and solution.

The simulations presented in this thesis are concerned only with the propagation of coherent radiation, therefore one can assume parallel propagation of the beam. Simplification of the wave equation is therefore possible via the paraxial approximation. This is done by assuming the propagation distance of the beam, z, is always much greater than any beam spreading that occurs. Assuming that radiation is in the optical or infrared range, it can been shown [82] that it is possible to neglect the middle term of the wave equation (2.3)[2]. Assume now a form for E and redefine the refractive index n in terms of the refractive index in free space plus a small perturbation n_1, i.e. $n = (1 + n_1)$. The form taken for E assumes a slow variation in the z co-ordinate (where z is the direction of propagation), i.e.

$$E = E(x, y, z)\exp[ikz]. \qquad (2.5)$$

[2] Radiation scattered by large fluctuations in the refractive index is scattered at an angle no greater than $\lambda / l_0 \sim 10^{-4}$ for optical and infra red light. Hence one can neglect the middle term in (2.3).

Substituting into equation (2.3), neglecting the $\frac{\partial^2 E}{\partial z^2}$ term[3] and assuming $(1+n_1)^2 \approx 1+2n_1$ results in the paraxial approximation to the wave equation:

$$2ik\frac{\partial E}{\partial z}+\left(\frac{\partial^2}{\partial y^2}+\frac{\partial^2}{\partial x^2}\right)E+2k^2 n_1{}^2 E=0. \qquad (2.6)$$

The *z* direction is the direction of propagation while the *x* and *y* co-ordinates are perpendicular to the beam's length. Equation (2.6) is the one that is used to simulate wave propagation between phase screens. As the space between each screen is assumed to be a vacuum, one can set $n_1 = 0$.

Two different methods for solving (2.6) numerically are suggested by Macaskill and Ewert [19]: a finite difference formulation; and a fast Fourier transform method. Although they present a method for making a finite difference solution manageable and fast, they conclude that the preferred method to solve (2.6) is the fast Fourier transform. They show that one can transform the electric field *E* into the Fourier domain, solve the resulting differential equation and then transform back into the real space domain to obtain

$$\frac{\partial \overline{E}(\kappa_x,\kappa_y,z)}{\partial z}=-i\frac{\kappa^2}{2k}\overline{E}(\kappa_x,\kappa_y,z), \qquad (2.7)$$

which is the required result. Equation (2.7) is the form of equation (2.6) in Fourier transform space, where $\overline{E}(\kappa_x,\kappa_y,z)$ is the 2-dimensional Fourier transform of $E(x,y,z)$. κ_x and κ_y are the frequency space co-ordinates, where $\kappa^2=(\kappa_x^2+\kappa_y^2)$. This is a simple linear ODE whose solution is easy to find. Given an initial condition on *z*, i.e. $z = z_0$ initially,

[3] Because $\frac{\partial^2 E}{\partial z^2} << \frac{\partial E}{\partial z}$ under the assumption of slow variation in the *z* direction.

$$\overline{E}(\kappa_x, \kappa_y, z) = \overline{E}(\kappa_x, \kappa_y, z_0)\exp\left\{-i\frac{\kappa^2(z-z_0)}{2k}\right\}. \quad (2.8)$$

A simple inverse Fourier transform yields the field in real space. The computational procedure required to simulate the propagation of a laser beam through free space is clear. A fast Fourier transform method is used, first to transform the field data into its spectral components $\overline{E}(\kappa_x, \kappa_y, z)$, then to Fourier invert back into the real space after the propagation term, $\exp\left[-i\frac{\kappa^2(z-z_0)}{2k}\right]$, has been applied. The real space result being the electric field at some observation plane located at $z = L$, i.e. $E(x, y, L)$.

2.2. The phase screen technique.

The discussion to this point has focused on the propagation of a wave or wave packet through a vacuum. Indeed the presence of a vacuum is a crucial assumption in the reduction of the wave equation to its paraxial form. The simulation of atmospheric propagation requires the simulation of the medium through which the beam propagates. This is done by the well-documented phase screen method, as introduced in chapter 1.

A laser beam (i.e. a coherent radiation source) is characterised by its initial profile, the 'phase screen' [2, 3, 7, 8 and others] method is then employed to simulate the extended medium (i.e. the Earth's atmosphere) into which the beam propagates. The phase screen method numerically represents the random medium as one or more infinitesimally thin 'screens' transverse to the direction of propagation, each of which imparts a phase shift onto the field. It is possible to calculate the field resultant from such a propagation of the beam by several methods; two that are employed here are the Huygens Fresnel integral for analytical treatment, and a fast Fourier transform algorithm for numerical treatment as discussed above. These phase fluctuations result in amplitude fluctuations that build up in the field as a result of the propagation. This gives features such as focussing and caustics in the beam.

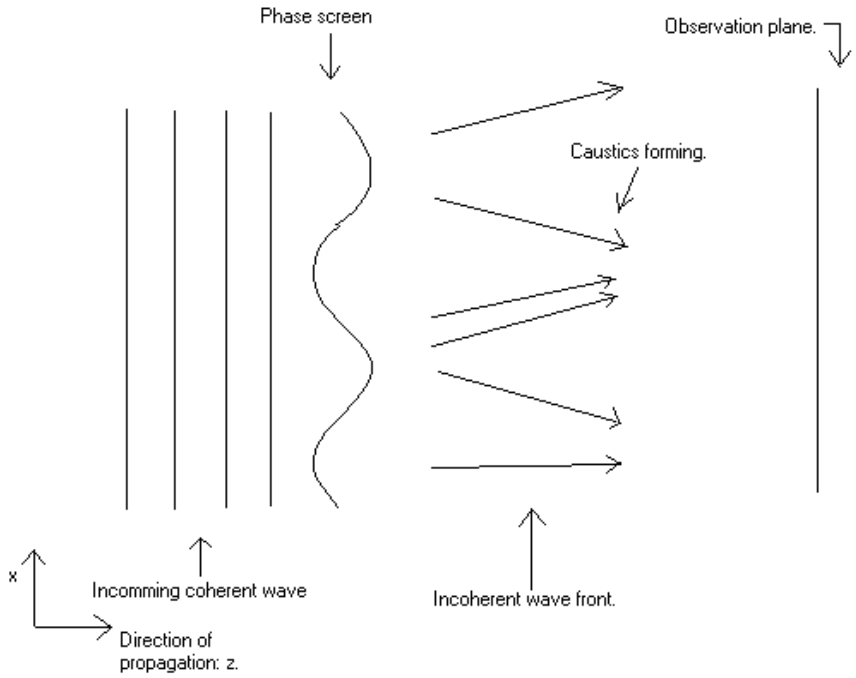

Fig. 2.1: Diagrammatic representation of the phase screen method.

The phase screen is essentially a method of creating statistically-correlated phase changes in a wave front. These phase fluctuations introduced into the beam's path are intended to simulate the effects of temperature (i.e. refractive index) fluctuations in the atmosphere, as well as the motion of the air. This is very similar to the effect of a sheet of misted glass, or a swimming pool, on the light reflecting off, or refracting through, it. The variation in the refractive index of the material causes phase fluctuations in the light.

The computer simulation of a phase screen involves the generation of an array of pseudo-random complex Gaussian numbers, then filtering this data to include the desired statistical properties. One achieves this by the application of a fast Fourier transform algorithm, and an idealised filter function (which is a Fourier pair with the auto-correlation function) that gives the screen the desired statistics. The specific method, which employs the Weiner-Khintchine relations [18], employs a convolution of the spectral components of the noise with those of the autocorrelation function. After a subsequent inverse Fourier transform, the real and imaginary parts of the resulting correlated noise constitute phase screens with the required statistical properties.

2.2.1. Statistics of the phase screens, Gaussian noise model.

Statistical correlation of a phase screen is required in order that it be considered a valid model for atmospheric turbulence, an array of independent pseudo-random numbers constituting white noise is not sufficient to be such a phase screen.

The simplest auto-correlation function for the phase screen data is the Gaussian. Booker et al. argued in their seminal paper [2] on phase screen techniques that the screen should have a Gaussian correlation as a result of the central limit theorem applying to the build up of small-size turbulent eddies in the atmosphere. It has since been shown that the Gaussian screen, although useful for analytical work, is not an accurate model for atmospheric turbulence. It is, however, not a model that should be ignored; its simplicity of use in analytical work makes it a useful tool for investigating the validity of simulation. Indeed, it is with that goal in mind that it is employ it in this thesis. The Gaussian auto-correlation function of the phase fluctuations ϕ is defined, in real space, as

$$\rho_\phi(\underline{r}) = \langle \phi(r_1)\phi(r_1 - r) \rangle = \phi_0^2 \exp\left(\frac{-|\underline{r}|^2}{\xi^2} \right), \tag{2.9}$$

where $\phi(r)$ is the phase screen data, $\langle \mathrm{K} \rangle$ an ensemble average and ξ the correlation length. There is also a strength parameter ϕ_0, which determines the mean square value of the phase fluctuations introduced by the screen (also referred to as the 'depth'). Figures 2.2 and 2.3 show examples of phase screens using Gaussian-correlated data. As has already been noted, one can define the correlation properties of the phase screen in terms of the spectral components of the noise such that

$$\Phi_\phi(\kappa) \sim \int_{-\infty}^{\infty} \rho_\phi(r) \exp(-ikr) dr \,. \tag{2.10}$$

The spectral form of the auto-correlation function (2.9) is also a Gaussian, and therefore can easily be defined in frequency space, in as opposed to real space.

This definition of the auto-correlation function in real space will only be possible for simple models. Other turbulence models may have to be defined solely by the power spectrum $\Phi_\phi(\kappa)$ in κ-space. Possible correlation models defined in real space have been noted in chapter 1 (see equations (1.5), (1.6) and (1.7)). None of these are viable models for real atmospheric turbulence; rather they are useful in the comparison of simulation techniques against simple theory.

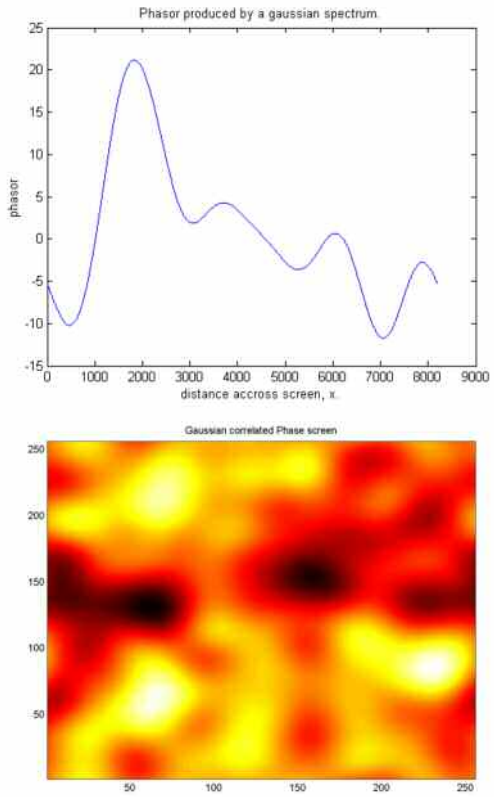

Figs 2.2 and 2.3: Gaussian phase screens in 1 and 2 dimensions respectively. In fig. 2.2, the depth ϕ_0 = 10 while ξ = 1000; in fig. 2.3 ϕ_0 = 10 and ξ = 30.

The above figures show two examples of Gaussian-correlated phase screens. Note the smooth contours on the screens, this is a characteristic feature of 'idealised' noise.

2.2.2. The Kolmogorov theory of turbulence.

The Kolmogorov cascade theory of turbulence is based on certain assumptions about the structure of a viscous fluid and the way that energy dissipates in it; the theory can

be used to develop an auto-correlation function that is used to accurately model atmospheric turbulence in a phase screen simulation. The main assumption underpinning Kolmogorov's theory is that there exist certain outer (L_0 which corresponds to an inner scale $\kappa_I \sim (1/L_0)$ in κ-space) and inner (l_0 which corresponds to an outer scale $\kappa_O \sim (1/l_0)$ in κ-space) scales which characterise the size of turbulent eddies. Energy is injected into the atmosphere at large scales by the action of the wind and large-scale convection currents; this causes eddies to form in the atmosphere whose sizes are characterised by the outer scale L_0. Smaller eddies are formed via the transfer of energy through the system; the smallest possible size for an eddy corresponds to the inner scale l_0. Once this scale is reached, the fluid moves into what is known as the viscous dissipation regime; turbulent eddies remaining in the system dissipate, and energy is lost as heat. The dissipation rate is assumed to be distributed in a lognormal form, although this has been challenged by several researchers [41] as the model disagrees with certain experimental results. Kolmogorov used dimensional analysis to show that the structure function for wind velocities should have a particular form [29, 31]. The structure function is defined as

$$D_x(r_1, r_2) = \left\langle [x(r_1) - x(r_2)]^2 \right\rangle \tag{2.11}$$

and is an important statistic in stochastic processes. Because the structure function is independent of whether the process is stationary or not, it can be used to define general properties about the process. Kolmogorov showed that $D_v(r_1, r_2)$ - the structure function for the wind velocities in the atmosphere - has a 2/3 power law; i.e.

$$D(R) = C_v^2 R^{\frac{2}{3}}, \tag{2.12}$$

where C_v is the structure constant, and is related to the energy dissipation rate of the fluid. The structure function is related to the power spectrum of the velocities via [36]

$$\Phi_v(\kappa) = \frac{1}{4\pi^2\kappa^2} \int_0^\infty \frac{\sin(R\kappa)}{R\kappa} \frac{d}{dR}\left[R^2 \frac{d}{dR} D_v(R) \right] dR \tag{2.13}$$

such that when equation (2.12) is applied the power spectrum follows a $-11/3$ power law form in κ. Similar analyses exist for both temperature and refractive index fluctuations in the atmosphere, each giving a $-11/3$ power law for the power spectrum. Thus Kolmogorov proposed $-11/3$ power law spectrum as a form for the spectral components of the refractive index fluctuations in the 'inertial subrange', (i.e. being the range of κ between the outer and inner scales). Note here that the inner scale, while forming a cut-off for short length behaviour in real space, corresponds to a cut-off at high-frequencies behaviour in κ-space. Thus the upper limit of the inertial subrange in frequency space corresponds to the lower range in real space, and vice versa for the outer scale in real space.

The form for the Kolmogorov spectrum in three dimensions is

$$\Phi_n(\kappa) = 0.033 C_n^2 \kappa^{\frac{-11}{3}}, \kappa_I = \frac{1}{L_0} << \kappa << \frac{1}{l_0} = \kappa_O \qquad (2.14)$$

where, as has been discussed, κ_I and κ_O define the inner and outer limits of the inertial subrange and C_n^2 is the structure constant for the refractive index in units of $m^{-2/3}$. Experimental data indicates that for the atmosphere the outer scale is of the order of metres in size while the inner scale is of the order of millimetres or centimetres depending on the specific turbulence conditions [31]. Regions of the spectrum outside the inertial subrange must be sampled in order to discretely model the turbulence. This problem has been addressed by several researchers. Tatarski suggested an extension to the Kolmogorov model to extend it into the viscous dissipation regime. The application of an arbitrary exponential factor effectively cuts the spectrum off at high frequencies. One unfortunate property of the Kolmogorov theory is that as the frequency approaches zero, the spectrum blows up to infinity. Von Karman proposed a second adjustment to the spectrum which would account for this. He suggested adding the inner scale to the frequency such that as κ approaches zero, the spectrum approaches a value proportional to $\kappa_I^{-11/3}$. The full modified Von Karman spectrum is then

$$\Phi_n(\kappa) = 0.033 C_n^2 \frac{\exp\left(\frac{-\kappa^2}{\kappa_O^2}\right)}{\left(\kappa^2 + \kappa_I^2\right)^{\frac{11}{6}}}, 0 < \kappa < \infty \qquad (2.15)$$

which is valid over all κ-space and can be used to model the Kolmogorov theory in a phase screen. Further refinements to the Kolmogorov model in addition to those above have been proposed in the light of additional experimental data concerning the nature of atmospheric turbulence. Voitsekovich [39] performed an analysis of the differences between various models for the outer scale, while experimental evidence from Hill and Clifford [27], showing the possible presence of a 'bump' in the spectrum at high wave numbers close to the outer scale (in κ-space), motivated Andrews [31] to propose a modification to the Von Karman spectrum,

$$\Phi_n(\kappa) = 0.033 C_n^2 \left[1 + 1.802\left(\frac{\kappa}{\kappa_O}\right) - 0.254\left(\frac{\kappa}{\kappa_O}\right)^{\frac{7}{6}}\right] \frac{\exp\left(\frac{-\kappa^2}{\kappa_O^2}\right)}{\left(\kappa^2 + \kappa_I^2\right)^{\frac{11}{6}}}, 0 < \kappa < \infty . \qquad (2.16)$$

In this 'modified Von Karman spectrum' the terms in the square brackets dominate at high wave numbers and introduce the 'bump' into the spectrum.

Several different spectral models of turbulence will be considered in more detail in the case of three-dimensional simulations in chapter 5.

2.2.3. The phase spectrum, $\Phi_\phi(\kappa)$.

The refractive index spectrum cannot be used immediately in the correlation of phase screen data. This is because the phase screen process uses fluctuations in the phase of the wave front to induce diffraction and focusing effects into the beam, whereas Kolmogorov theory refers to refractive index fluctuations. Thus the refractive index spectrum must be converted into a phase spectrum for use in phase screens.

The relationship between the refractive index and the phase can be derived from a simple geometric optics formulation. Starting from the Helmholtz equation (equation (2.4)) and assuming that the solution is of the form $U = Ae^{i\phi}$, a system of two equations can be derived [36]

$$\begin{aligned} &\nabla^2\phi + 2\nabla \log A.\nabla\phi = 0 \\ &(\nabla\phi)^2 = k^2 n^2(r) \end{aligned} \tag{2.17}$$

that describe the behaviour of the amplitude A and phase S. Assuming small perturbations in A and S, such that $\phi \approx \phi_0 + \phi_1$ and $\log(A) \approx \log(A_1) + \chi$, the refractive index fluctuations over the path of the beam and the phase changes are related by the path integral

$$\phi(x, y, L) = k\int_0^L n(x, y, z)dz \tag{2.18}$$

where n is the refractive index, k the wave number for the propagation, L the total propagation distance and ϕ the phase change along that path. From (2.18) the refractive index spectrum can be related to the phase spectrum. To do this one writes the correlation function, $\rho_\phi(x - x', y - y')$, for the phase ϕ in terms of the correlation function for the refractive index fluctuations $\rho_n(x - x', y - y')$

$$\begin{aligned} \langle \phi(x, y)\phi(x', y') \rangle &= \rho_\phi(x - x', y - y') \\ &= k^2 \int_0^L dz' \int_0^L dz \langle n(x, y, z)n(x', y', z') \rangle \quad . \\ &= k^2 \int_0^L dz' \int_0^L dz \rho_n(x - x', y - y', z - z') \end{aligned}$$

Changing to sum and difference variables $u = z - z'$ and $v = z + z'$, integrating out v and taking the Fourier transform gives

$$\int_{-\infty}^{\infty}\int_{-\infty}^{\infty}\rho_\phi(x'',y'')\exp\{-i(x''\kappa_x+y''\kappa_y)\}dx''dy'' \\ = k^2L\int_{-\infty}^{\infty}dx''\int_{-\infty}^{\infty}dy''\int_{-L}^{L}du\rho_n(x'',y'',u)\exp\{-i(x''\kappa_x+y''\kappa_y)\} \tag{2.19}$$

where $x-x'\to x''$ and $y-y'\to y''$. Using (2.19) gives

$$\Phi_\phi(\kappa_x,\kappa_y)=2\pi k^2L\Phi_n(\kappa_x,\kappa_y,0). \tag{2.20}$$

This relationship can be used for the formulation of the statistics of the phase screens. Applying this to the Von Karman spectrum for refractive index fluctuations in the atmosphere, one can determine a two- dimensional form for $\Phi_\phi(\kappa)$ which can be used to build two-dimensional screens for use in three-dimensional simulations:

$$\Phi_\phi(\kappa_x,\kappa_y)=0.207Lk^2C_n^2\frac{\exp\left(\frac{-\kappa^2}{\kappa_O^2}\right)}{\left(\kappa^2+\kappa_I^2\right)^{\frac{11}{6}}},\ \kappa^2=\kappa_x^2+\kappa_y^2,\ 0<\kappa_x,\kappa_y<\infty. \tag{2.21}$$

A one-dimensional form can now be calculated for the Von Karman spectrum for use in two-dimensional simulations. Integrating out the κ_y dependence [21] leaves

$$\Phi_\phi(\kappa_x)=0.696Lk^2C_n^2\frac{\exp\left(\frac{-\kappa_x^2}{\kappa_O^2}\right)}{\left(\kappa_x^2+\kappa_I^2\right)^{\frac{4}{3}}},\ \ 0<\kappa_x<\infty, \tag{2.22}$$

which is valid where κ_O is large. This is a valid approximation as one can always assume the turbulence has a small inner scale. Note that the phase spectrum has a -8/3 power law in the inertial subrange (plotted in figure 2.4 below).

The range of values that are used to sample κ-space need to be defined such that the fast Fourier algorithm performs properly. Given the particular coding used in these simulations, the κ-space region over a range must be defined over an area which is a

multiple of $\{-\pi, \pi\}$. Defining the size (in a physical sense) of the beam as L_x by L_y metres, the sample sizes used in the simulation in κ-space will be $d\kappa_x = 2\pi/L_x$ and $d\kappa_y = 2\pi/L_y$. Given that the number of samples taken is *N*, the range of values in κ-space is $\{-\pi L/N, \pi L/N\}$.

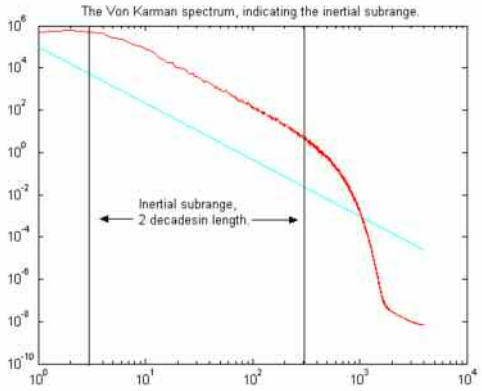

Fig. 2.4, the Von Karman filter (2.22) function in 1 dimension with the inertial subrange indicated, note the -8/3 power law behaviour within that range.

This range of values sampled in κ-space places a natural limit on the inner and outer scales that can be chosen for the simulation. The inner scale l_0 can be no smaller than the sample size, while the outer scale L_0 can be no larger than the physical size of the simulation. Note the way the spectrum flattens off at low and high frequencies, while in the inertial subrange a -8/3 power law behaviour is present. This spectrum is sampled numerically over κ-space and then transformed it into a real space correlation function using an inverse fast Fourier transform algorithm.

These screens (figures 2.5 and 2.6 below) were obtained by filtering the same white noise as was used in figures 2.2 and 2.3. A Von Karman filter was used rather than a Gaussian auto-correlation function. Notice the extra 'detail' in the screens indicating the existence of self-similar fractal behaviour in the pattern, a characteristic of Kolmogorov turbulence.

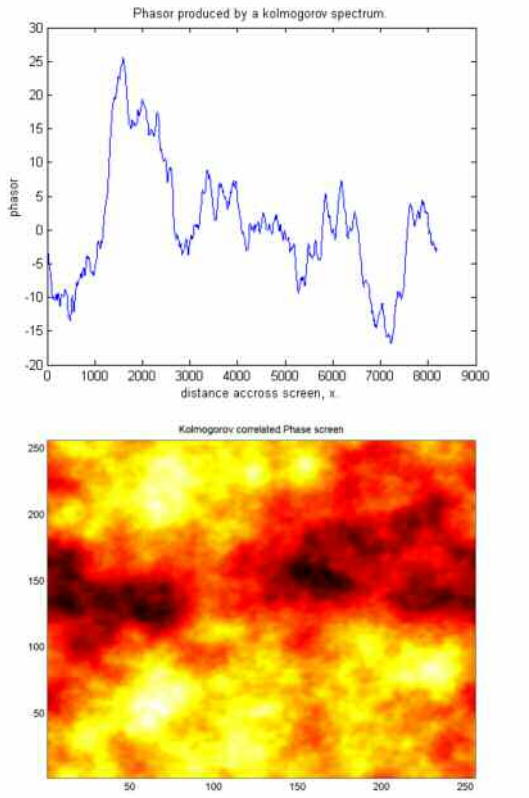

Figs 2.5 and 2.6: Phase screens characterised by a Von Karman filter.

The analytical form of the Fourier transform of equation (2.22) cannot be calculated, and as a result a fast Fourier transform algorithm must be used. One can, however, calculate the 'depth' of a phase screen filtered by such a Von Karman spectrum. The 'depth', or strength, of a phase screen is determined by the mean square phase shift in the screen; this corresponds to the value of the correlation function at $x = y = 0$ in real space. For the Gaussian correlation function (equation 2.9), this value is ϕ_0^2. For the Von Karman autocorrelation function, this value is calculated by performing the inverse Fourier transform of the spectrum at $x = 0$ (in the 1D case). The real space correlation function is

$$\rho_\phi(x) = \frac{1}{2\pi}\int_{-\infty}^{\infty} \Phi_\phi(\kappa)\exp(i\kappa x)d\kappa \tag{2.23}$$

at $x = 0$, the screen depth is then

$$\rho_\phi(0) = \frac{1}{2\pi}\int_{-\infty}^{\infty} \Phi_\phi(\kappa)d\kappa\,, \tag{2.24}$$

substituting the Von Karman phase fluctuation spectrum gives

$$\rho_\phi(0) = \frac{0.696Lk^2C_n^2}{2\pi}\int_{-\infty}^{\infty}\frac{\exp\left(\frac{-\kappa_x^2}{\kappa_O^2}\right)}{\left(\kappa_x^2+\kappa_I^2\right)^{\frac{4}{3}}}d\kappa \tag{2.25}$$

which can be expressed in terms of hypergeometric functions [32] as

$$\rho_\phi(0) = \left\langle \phi_0^2 \right\rangle = \frac{0.696Lk^2C_n^2}{2\pi}\left\{\frac{2.24\,{}_1F_1\left(\frac{1}{2},\frac{1}{6},\frac{\kappa_I^2}{\kappa_O^2}\right)}{\kappa_I^{5/3}} - \frac{6.68\,{}_1F_1\left(\frac{4}{3},\frac{11}{6},\frac{\kappa_I^2}{\kappa_O^2}\right)}{\kappa_O^{5/3}}\right\}. \tag{2.26}$$

Hence, given values of C_n^2, L, κ_I and κ_O, one can determine the strength of the phase screen.

2.3. The Simulation technique.

An algorithm for performing numerical simulations of wave propagation through turbulence characterised by phase screens can now be written down:

- Numerically set up the coherent wave front to be propagated; the front can be in 1 or 2 dimensions.
- Set up the desired auto-correlation function for the phase screens that will be used in the simulation. This is done either in real space (Gaussian) or in κ-space (Kolmogorov / Von Karman) as required.
- Set up the phase screen(s) using the Weiner-Khintchine method of correlating pseudo-random complex Gaussian numbers. The phase screens need to be of size greater than or equal to the wave front.
- The wave interacts with the phase screen; this occurs by the phase screen data acting as a phase shift on the wave itself.

- A Fourier transform algorithm is used to solve the wave equation (2.8) and propagate the beam through a vacuum to the observation screen (or next phase screen).
- Further phase screen interactions and propagation occur (extended medium, i.e. multiple phase screens, case only).
- An inverse Fourier transform is performed at the observation screen the result is the final propagated wave.

There are a number of further technical points which need to be discussed before considering a validation of the simulation technique against published results. The fast Fourier transform is a process that transforms a set of *N* data points into a second set of data containing *N* elements. If one increases the size of the data set by M , then the length of time taken for the fast Fourier transform process to finish increases by $M\log(M)$. The use of an ever-increasing number of data points in the phase screen will lead to simulations that take a very long time to complete. It is perhaps preferable to perform several realisations of smaller sized screens and wave fronts rather than single large simulations in order to produce accurate statistics. Note that this $M\log(M)$ behaviour is still preferable to the increase in time that would occur if one were to use a forward difference method for solving the wave equation, in that case the a time increase would be an order no less than M^2 [19].

These time considerations are very important when it comes to simulations in three-dimensions; in these cases one can set up phase screens of the form $2^N \times 2^N$ in order to preserve the efficiency of the fast Fourier transform algorithm. The difference in time taken to perform a simulation using $N = 8$ and $N = 9$ is quite large, because there are four times as many data points in the screen.

The second point is concerned with boundary conditions. This is an issue considered by Ewert and Macaskill [19]; they concluded that one useful aspect of the fast Fourier transform method is that it requires no boundary conditions to be arbitrarily set. This is due to the periodic nature of the FFT process. Thus one edge of the screen is wrapped around and connected to the opposite edge during the fast Fourier transform. Although this saves the task of setting up arbitrary boundary conditions, it leaves a

problem of aliasing. Aliasing occurs when a part of the beam diffracting off the screen on one side of the simulation is brought back on to the screen on the far side of the simulation. This only becomes a problem when an element of the beam has diffracted so far off one side of the screen that it returns on the other side and interferes with itself again. There are two main ways to keep this possible source of error under control; use of 'padding' or restricting the propagation range of the simulations.

'Padding' introduces a region of blank space around the beam profile, which gives the beam some space to diffract into without returning to the far side of the simulation as a result of the periodicity. Restricting the propagation range works by first calculating the average distance over which propagation will have to occur for aliasing to happen; then restricting propagation geometries to ranges less than that value. In this thesis a system of padding is preferred, as this places fewer restrictions on the simulation.

The third matter, which applies mainly to Gaussian-profile beam propagations, is beam spreading and wander. These phenomena occur as a result of diffraction and interaction with the propagation medium. Generally, beam wander is a result of large scale movements of air across the front of the beam, while spreading occurs due to diffraction effects. Wander can be characterised by the variance of the displacement of the beam from the initial centre. Churnside and Lataitis [47] discuss a geometric derivation of the above statistic for a Gaussian beam propagating in weak Kolmogorov type turbulence. They produce results valid for both collimated and focused Gaussian beams, showing that the wander parameter depends on the initial beam diameter and the path length.

Beam spreading and wander are matters discussed at length by Belmonte [7]. The expression [52]

$$W^2(z) = W_0^2\left[1+\left(\frac{z}{z_0}\right)^2\right] + 2\left(\frac{4z}{kr_{0,S}}\right)^2 \qquad (2.27)$$

gives the beam intensity radius *W(z)* at a propagation distance *z*, given an initial beam radius W_0. The $4z/kr_{0,S}$ term here is approximately equal to the outer scale of the turbulence spectrum, L_0. $r_{0,S}$ is the spherical wave coherence diameter, defined by

$$r_{0,s} = \left[0.42k^2 \int_0^L C_n^2(z) \left(\frac{z}{L} \right)^{\frac{5}{3}} dz \right]^{-\frac{3}{5}}. \tag{2.28}$$

In a vacuum a beam is expected to undergo an angular spreading of order λ / W, such that λ is the wavelength and W the beam diameter. The use of 'padding' around the beams in simulations is therefore crucial, as it allows free space for spreading and wander to occur without causing aliasing. Spreading and wander are discussed in greater depth in chapter 5.

2.4. Simulation parameters.

In the numerical simulations presented in this thesis there are two different ways that one can define the parameters used. One can either use real values in terms of standard S.I. units, or values normalised to the sample size Δx of the simulations. The use of real values is important in the comparison of simulations to experimental data or to theory cast in physical terms. The use of a mathematically idealised set of parameters is useful for checking the simulation technique against simple theory.

The difference between these two methods of defining the parameters is most clear when looking at the strength of the turbulence used. The level of the turbulence is defined subtly differently in the case of the two most important turbulence models, the Gaussian (2.9) and the Von Karman (2.22). In (2.9) the mean square phase shift, defined by $\langle \phi^2(r) \rangle = \phi_0^2$, is imposed on the wave front. This is the same regardless of any other parameters such as the propagation distance or the wavelength. In the derivation of (2.21) the refractive index structure parameter C_n^2 defines the level of the turbulence. Equation (2.26) shows that the strength of the turbulence is dependent on not only C_n^2, but on *z*, *k* and the inner and outer scales. Therefore, given a constant

value for C_n^2, the effective $\langle \phi^2(r) \rangle$ changes depending on several other factors. This is indeed how beam propagation in the physical world works (i.e. a beam of a shorter wavelength λ will experience a greater level of scintillation for a given C_n^2 and propagation distance). The use of $\langle \phi^2(r) \rangle$ is a simplification of reality; it is used in simulations only as a means to relate work to simple analysis.

Many simulations require the introduction motion into the medium. This is done by moving the phase screens within the simulation. In this case a temporal co-ordinate Δt is defined, such that the velocity of the screen is $v = \Delta x / \Delta t$. This will become important, and will be discussed again at greater length, when looking at temporal phase spectra in chapters 4 and 5.

2.5. Validation of the simulation technique.

The simulation technique is designed with the ultimate goal of modelling atmospheric turbulence numerically to provide a basis from which one can test theory against experimental data. As discussed above, the Kolmogorov theory of turbulence and Von Karman spectrum provide a theoretical base on which to build our simulations; it is useful though to test the simulation technique against simpler and more analytically accessible models for atmospheric turbulence, namely the Gaussian correlation model (equation (2.9)). There are several different statistics that can be used to interpret simulation results, they are, as noted in chapter 1, the intensity *I*, the phase θ and the intensity-weighted phase derivative *J*. These simulations are used to justify the validation of the simulation technique.

2.5.1. Regimes of propagation; Fresnel, focussing and Fraunhofer regimes.

It is well known that 3 distinct regimes exist in the propagation of coherent laser radiation; a Fresnel zone, a focussing regime and a Fraunhofer zone. In the Fresnel zone diffraction has yet to cause features such as caustics. In the focussing regime the formation of caustics and peaks in the field causes a maximum in the value of the

scintillation index $\sigma_I = \langle I^2 \rangle / \langle I \rangle^2$. In the Fraunhofer zone the intensity statistics approach a saturation limit and the σ_I approaches a constant. These regions are investigated by looking at the probability density functions for three statistics, the intensity *I*, the phase derivative $\dot{\theta}$ and the intensity-weighted phase derivative *J*. The pdf for the phase θ not considered as one expects to see to a uniform distribution for sufficiently large turbulence. The propagation of a coherent radiation source[4] into increasingly large propagation distances is considered.

One can model the pdf of the intensity fluctuations by a lognormal distribution. Under the Rytov perturbation technique (as described in chapter 1), it can be shown that the logarithm of the intensity in the far field under weak turbulence conditions is governed by a Gaussian distribution [24, 31]

$$p(I) = \frac{1}{2I\sigma_\chi\sqrt{2\pi}} \exp\left(-\frac{\left(\ln\frac{I}{I_0} - 2\langle\chi\rangle \right)^2}{8\sigma_\chi^2} \right), \tag{2.29}$$

where $\chi = \frac{1}{2}\ln(I/I_0)$, I_0 is the initial intensity of the beam at $z = 0$ and σ_χ^2 is the variance of χ. This approximation is valid for weak propagation regimes, and so should be valid in the Fresnel zone. In the far field regime the phase derivative is described by a student - *t* distribution (equation (1.10)) as the field is characterised as a Gaussian circular process. Thus a -3 power law is expected in the tail of the probability distribution.

[4] Simulations in this chapter use a plane wave as a coherent radiation source.

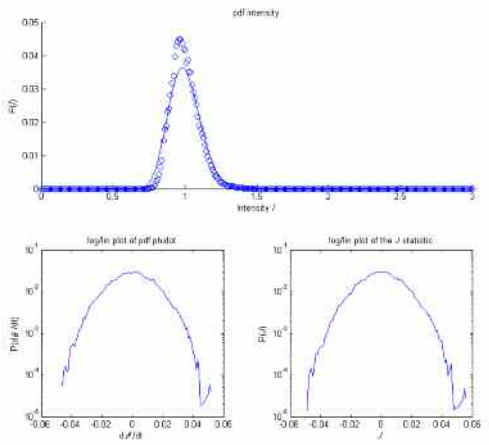

Fig. 2.7, pdfs of *I*, $\hat{\theta}$ and *J* in the Fresnel zone, -ln(*q*) = -2.

Figure 2.7 illustrates pdfs for the three statistics. A two-dimensional simulation propagation is used with a normalised distance $-\ln(q) = -2$ where $q = \frac{k\xi^2}{2L\phi_0\sqrt{6}}$ [4], this allows the same simulation to be performed for different values of *k*, *L*, ξ and ϕ_0. The simulations make use of a single Gaussian filtered (equation (2.9)) phase screen. Phase derivative data is obtained from the propagated wave by calculating the phase across the wave front, unwrapping and then taking the difference between each data point and the next in order to create a spatial derivative that equates to the temporal derivative. 'Unwrapping' the phase data involves removing any jumps in the data from 2π to -2π (i.e. places where the phasor passes the positive real axis in the complex plane), in order to smooth the phase derivative. Taking phase derivative statistics in this way tacitly assumes that the phase screen is effectively moving across the wave front at 'unit speed', i.e. one spatial unit per temporal unit. This allows one to equate the spatial co-ordinate to the temporal one and find the time derivative of the phase by taking the spatial one. Note, from fig. 2.7, that *P(I)* is centred on 1 as the propagation of the beam into the near regime has had little effect on the intensity. Note also that the pdfs for *J* and $\hat{\theta}$ (plotted in a log-linear format so as to make the tails visible) are almost identical, this is expected as the intensity is almost uniformly equal to 1 across the wave front and therefore $J = I\hat{\theta} \approx \hat{\theta}$.

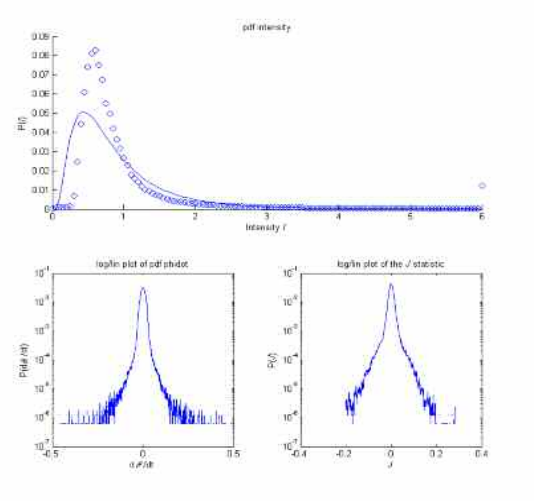

Figure 2.8, pdfs of *I*, $\dot{\phi}$ and *J* in the focussing regime, -ln(*q*) = 0.

Figure 2.8 gives the equivalent pdfs as figs 2.7 for a plane wave propagated into the focussing regime. In terms of the normalised propagation parameter *q*, this amounts to setting $-\ln(q)=0$. Note now a discernable difference between the plots for the $\dot{\phi}$ and *J*; there is less 'noise' in the tail of the plot for *J*, an indication of the 'smoothing' effect that the weighting is intended to have on the phase derivative. The exact fit seen between the simulations and theory in the pdf for *I* in fig. 2.7 is no present in fig. 2.8. This is a clear indication that the propagation regime has moved beyond the Fresnel zone, and that the Rytov assumptions are no longer valid in the focussing regime.

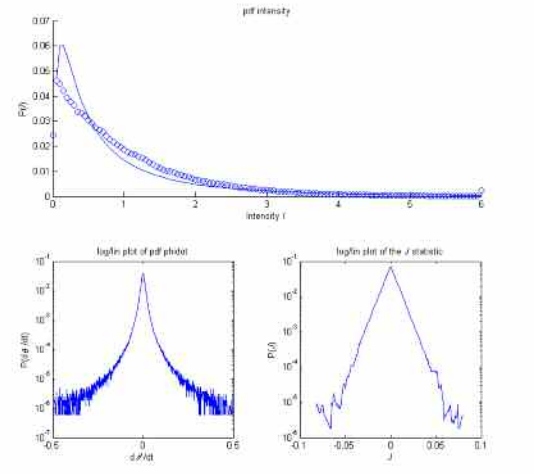

Figure 2.9, pdfs of *I*, $\dot{\phi}$ and *J* in the Fraunhofer zone, -ln(*q*) = 4.

Figure 2.9 shows that the pdf for the intensity has become a negative exponential; this is because the field is in the Fraunhofer zone and consistent with Gaussian noise theory. It is clear also that the log normal model does not match the simulation data in this regime. The pdf for J has taken on a $\exp(-|J|)$ form (equation (1.13)). Chapter 3 will look at the form of the pdf of J in the more general case of the Rician field.

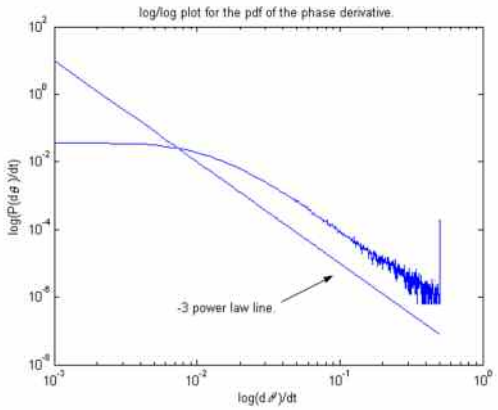

Figure 2.10, log/log plot for the pdf of $\hat{\theta}$ in fig. 8, the -3 power law tail is clear.

Figure 2.10 gives a log / log plot of the pdf of $\hat{\theta}$, a -3 power law in the tail of the distribution can be seen as predicted in equation (1.10). Three basic regimes of the propagation are clearly present in the simulations. Consider now a validation against the scintillation index.

2.5.2. Scintillation index: curves for Gaussian correlated phase screens.

The form of the scintillation index σ_I curve for a 'deep' screen was calculated by Jakeman and McWhirter [4] for several different forms of correlated phase screen. The scintillation index plot shows the differing regions of propagation. Figure 2.11 gives the scintillation indices for four different strengths of phase screen (all deep, i.e. $\phi_0 > 1$) using single Gaussian correlated phase screens similar to those used in the simulations in section 2.5.1. The Fresnel zone is characterised by a value of $\sigma_I \approx 1$, while the saturation regime has $\sigma_I = 2$.

The focussing regime is characterised by a peak in σ_I for strong turbulence propagations. In the case of weak turbulence, there is no focussing regime, and the saturation regime doesn't correspond to Gaussian statistics in the intensity, rather σ_I approaches a value of $2-\exp\left(-2\phi_0^2\right)$ as calculated by Mercier [3].

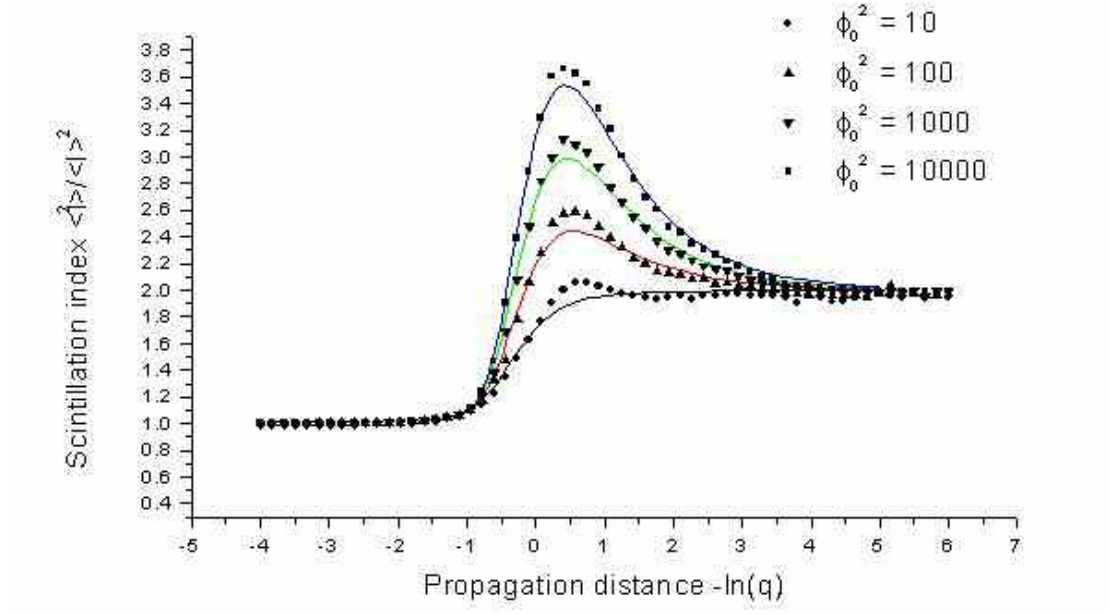

Fig. 2.11; scintillation index curves for plane waves propagated through deep, Gaussian-correlated, corrugated phase screen. Solid lines indicate theory [4] symbols are numerical simulation.

One can calculate a form for the scintillation index curve for a weak screen using a simple Huygens-Fresnel integral approach, similar to that used in [4]. This can then be used to test weak turbulence simulations. The calculation in 1 dimension using a Gaussian correlated phase screen begins with the definition of the electric field *E* propagated in one dimension beyond a phase screen $\phi(x)$ to a distance *L* as

$$E(L)=\sqrt{\frac{k}{2\pi L}}\int_{-\infty}^{\infty}dx\exp\left\{\frac{ik}{2L}x^2+i\phi(x)\right\}, \tag{2.30}$$

where *k* is the same as defined above and *x* a dummy integration variable in the plane of the phase screen. The second moment of the intensity is

$$\left\langle I^2 \right\rangle = \left\langle (EE^*)^2 \right\rangle = \left(\frac{k}{2\pi L}\right)^2 \int_{-\infty}^{\infty} \prod_{i=1}^{4} dx_i \exp\left(\frac{ik}{2L}\left[x_1^2 - x_2^2 + x_3^2 - x_4^2\right]\right) \times \mathrm{K}$$
$$\mathrm{K}\left\langle \exp\left(i\left[\phi(x_1) - \phi(x_2) + \phi(x_3) - \phi(x_4)\right]\right)\right\rangle \tag{2.31}$$

where x_i are the integration variables. Now employ a well-known sum and difference co-ordinate change [3, 4, 16, 21]

$$\begin{aligned} y_1 &= \frac{1}{2}\left((x_1 - x_2) + (x_3 - x_4)\right) \\ y_2 &= \frac{1}{2}\left((x_1 - x_2) - (x_3 - x_4)\right) \\ y_3 &= \frac{1}{2}\left((x_1 + x_2) + (x_3 + x_4)\right) \\ y_4 &= \frac{1}{2}\left((x_1 + x_2) - (x_3 + x_4)\right) \end{aligned} \tag{2.32}$$

and the fact that for a Gaussian variable A one can write $\left\langle \exp(iA)\right\rangle = \exp\left(-\frac{1}{2}\left\langle A^2\right\rangle\right)$, to give

$$\left\langle I^2 \right\rangle = -\left(\frac{k}{2\pi L}\right)^2 \int_{-\infty}^{\infty} \prod_{i=1}^{4} dy_i \exp\left(\frac{ik}{L}\left[y_1 y_3 + y_2 y_4\right]\right) \times \mathrm{K}$$
$$\mathrm{K}\exp\left\{-\phi_0^2\left[\begin{array}{l} 2 - \rho(y_1 + y_2) - \rho(y_4 - y_1) - \rho(y_1 - y_2) \\ -\rho(y_1 + y_4) + \rho(y_2 + y_4) + \rho(y_4 - y_2) \end{array}\right]\right\} \tag{2.33}$$

where $\rho(x)$ is the correlation function. The integral of equation (2.33) over y_3 gives a delta function in y_1, the resulting integral in y_1 then gives

$$\left\langle I^2 \right\rangle = \frac{-k}{2\pi L}\int_{-\infty}^{\infty} dy_2 dy_4 \exp\left(\frac{ik}{L} y_2 y_4\right)\exp\left[-\phi_0^2\left[\begin{array}{l} 2 - 2\rho(y_2) - 2\rho(y_4) + \mathrm{K} \\ \mathrm{K} + \rho(y_2 + y_4) + \rho(y_4 - y_2) \end{array}\right]\right] \tag{2.34}$$

which can now be solved by assuming a Gaussian form (2.9) for the auto-correlation functions $\rho(x)$ and a weak phase screen (i.e. $\phi_0^2 < 1$) such that

$\exp\left(-\phi_0^2 F(t)\right) \approx 1-\phi_0^2 F(t)$. Integrating over y_2 and y_4 is now a matter of calculating Gaussian integrals, resulting in the final expression

$$\left\langle I^2 \right\rangle = 2\phi_0^2 + 1 - 2\phi_0^2 \cos\left(\frac{1}{2}\arctan\left[\frac{4L}{k\xi^2}\right]\right) \Bigg/ \left(1+\left(\frac{4L}{k\xi^2}\right)^2\right)^{\frac{1}{4}}. \qquad (2.35)$$

This expression is now used to test the one-dimensional simulation technique in weak turbulence conditions.

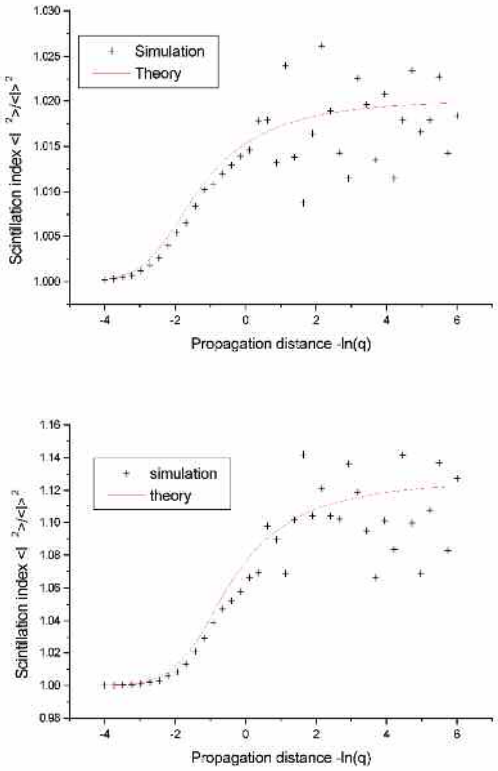

Figs 2.12 (ϕ_0 = 0.1) and 2.13 (ϕ_0 = 0.25), showing the scintillation index for weak phase screen propagations.

Figures 2.12 and 2.13 show that the simulation results agree reasonably well with the theoretical calculation (equation (2.35)). Note the existence of a large amount of noise in the scintillation index for large propagation distances q despite the use of 1000 realisations in an attempt to reduce error. This kind of noise has been found to occur regularly in weak turbulence simulations; this issue is discussed in more detail

in the next chapter. Note that the saturation (i.e. far field) value of the scintillation index corresponds to Mercier's value of $2-\exp\left(-2\phi_0^2\right)$ in each case.

2.5.3. Second order intensity weighted phase derivative statistics using a Gaussian correlated phase screen.

As already discussed, the intensity-weighted phase derivative is an important statistic in coherent radiation propagation. The second moment of this statistic $\left\langle J^2\right\rangle$ is a measure of the level of scintillation in the beam in a similar way to the scintillation index. Theory which predicts the form for the second moment of *J* in a strongly turbulent regime is developed in [16]. The statistic is normalised, such that $\left\langle J^2\right\rangle\Big/\left\langle J^2\right\rangle_{z=0}$. In the case of plane wave propagation this is a valid normalisation as the intensity-weighted phase derivative at the screen (i.e. at $z = 0$) is equal to the phase derivative. This normalisation is in contrast to the normalised second moment of the intensity statistic (i.e. the scintillation index), which is normalised by the square of the first moment. Such normalisation would be inappropriate for the *J* statistic, as its odd moments are all zero (see section 3.1.2).

The *J* statistic is calculated from simulation data by retrieving the phase derivative as discussed in section 2.5.1 and weighting it with the appropriate intensity value; normalisation of the second moment of the *J* statistic occurs by calculating the second moment of the phase derivative of the phase screen itself. It is clear that one expects to see $\left\langle J^2\right\rangle\Big/\left\langle J^2\right\rangle_{z=0}=1$ for $-\ln(q)<<1$ (i.e. short propagation distances), and one can show (below) that $\left\langle J^2\right\rangle\Big/\left\langle J^2\right\rangle_{z=0}=0.5$ for longer distances as the propagation enters the saturation regime.

For a plane wave, assume that initially the intensity is unity; thus *J* is exactly equal to the phase derivative ϕ, therefore $\left\langle J^2\right\rangle_{z=0}=\left\langle \phi^2\right\rangle=-\dfrac{\partial^2}{\partial t^2}\langle\phi(0)\phi(t)\rangle_{t=0}$. For a Gaussian variable (i.e. in the far field where there is a Gaussian saturation regime),

$\left\langle J^2 \right\rangle = \left\langle \dot{X}^2 \right\rangle = -\frac{\partial^2}{\partial x^2}\left\langle X(0)X(x)\right\rangle_{x=0} = -\frac{1}{2}\frac{\partial^2}{\partial x^2}\left\langle E(0)E(x)\right\rangle_{x=0}$ [21],[5] one can now calculate the correlation function of the electric field E in the far field using the Huygens Fresnel technique in terms of the phase fluctuation ϕ. The correlation function for the electric field is

$$\left\langle E(0)E^*(x)\right\rangle = \frac{1}{(\lambda z)^2}\int_{-\infty}^{\infty}\exp\left[\frac{ik}{2z}\left(|\underline{r}|^2 - |\underline{r}' + x|^2\right)\right]\left\langle \exp(\phi(\underline{r}) - \phi(\underline{r}'))\right\rangle d^2\underline{r}\, d^2\underline{r}'. \qquad (2.36)$$

Using the fact that $\left\langle \exp(iA)\right\rangle = \exp\left(-\frac{1}{2}\left\langle A^2\right\rangle\right)$ and transforming to sum and difference co-ordinates, $\underline{r} = \underline{q} + \underline{p}$ and $\underline{r}' = \underline{q} - \underline{p}$, gives

$$\left\langle E(0)E^*(x)\right\rangle = \frac{1}{(2\lambda z)^2}\int_{-\infty}^{\infty}\exp\left[\frac{ik}{2z}(2\underline{p} - x)(2\underline{q} + x)\right]\exp\left(-\frac{1}{2}\left\langle\left[\phi(0) - \phi(\underline{p})\right]^2\right\rangle\right)d^2\underline{p}\, d^2\underline{q}$$

from which the integral over $\underline{q}$ gives a delta function,

$$\begin{aligned}\left\langle E(0)E^*(x)\right\rangle &= \int_{-\infty}^{\infty}\exp\left(-\frac{1}{2}\left\langle\left[\phi(0) - \phi(\underline{p})\right]^2\right\rangle\right)\delta(\underline{p} - x)d^2\underline{p} \\ &= \exp\left(-\frac{1}{2}\left\langle\left[\phi(0) - \phi(x)\right]^2\right\rangle\right)\end{aligned}. \qquad (2.37)$$

The second moment of the J statistic can now be written in terms of this expression

$$\begin{aligned}\left\langle J^2\right\rangle &= -\frac{1}{2}\frac{\partial^2}{\partial x^2}\exp\left[\left\langle\phi(0)\phi(x)\right\rangle - \left\langle\phi^2\right\rangle\right]_{x=0} \\ &= \frac{1}{2}\left\langle\dot{\phi}^2\right\rangle \\ &= \frac{1}{2}\left\langle J^2\right\rangle_{z=0}\end{aligned}.$$

$$\therefore \quad \left\langle J^2\right\rangle \Big/ \left\langle J^2\right\rangle_{z=0} = 1/2$$

[5] X is defined in section 1.1 as the real part of the field such that $E = X + iY$. Also see equation (1.15).

Figure 2.14 gives four plots of the normalised second moment of the *J* statistic for the same four phase screen depths as used in figure 2.11. The normalised distance parameter *q* is used. The statistic is looked at over a range of propagation distances and for several different turbulence strengths. Notice a peak in the statistics in the focussing regime, the saturation of the statistic to a value of ½ in the Fraunhofer zone as predicted above and the initial value at unity in the Fresnel zone. The theoretical curves given in figure 2.14 seem to be slightly over-estimating the values of the statistic calculated by simulation; this is a minor artefact though, which has been noted in other simulation results [16].

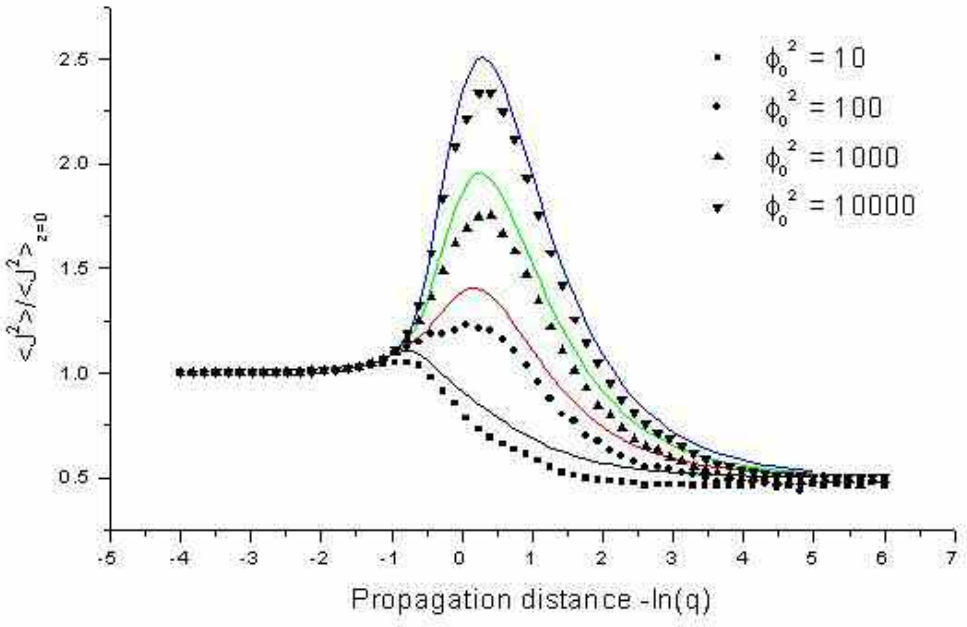

Fig. 2.14, the second moment of the *J* statistic for a deep, one-dimensional, Gaussian correlated single phase screen; simulation is symbols, theory [16, 21] is the lines.

The two sets of scintillation curves, for σ_I and $\langle J^2 \rangle / \langle J^2 \rangle_{z=0}$, presented in this section form a strong validation for the simulation technique. Three distinct regions of propagation exist in the statistics, the statistics also converge to their saturation values in the far field. The focusing regime is an area for which little theory exists and the match between simulation and theory here shows that numerical simulation techniques may be the best way to investigate this region.

2.6. Conclusions.

This chapter has looked at the theoretical development of the phase screen technique as a method for the numerical simulation of coherent radiation propagation. The phase screen method has allowed for the modelling of phase fluctuations incurred by a propagating beam (due to refractive index fluctuations and wind shearing) as a thin phase-changing screen. The phase fluctuations are imposed on the beam at the start of the propagation path and at locations along the path where screens are located. Although a forward difference method solution is possible for the paraxial wave equation (equation (2.6)), a fast Fourier transform method is superior in speed and easier to code. The Kolmogorov theory of turbulence was also considered, including the theoretical background to the underlying assumptions and development of the power spectrum for use in correlating a complex circular Gaussian process for use in phase screens. It is clear that the Kolmogorov theory of turbulence is only the first step on the path to finding a viable method for modelling atmospheric turbulence, several developments to the theory have been alluded to, namely the Tatarski and Von Karman spectra modifications which include scale effects (albeit in an arbitrary manner).

The practicalities of performing numerical simulations have also been considered, such as simulation parameters other technicalities like ‘padding’ to allow for beam spreading and aliasing. Two different methods for determining the strength of the turbulence in the simulation were considered. The difference between defining the phase perturbation to be applied to the wave and defining the refractive index structure parameter C_n^2 is important and a distinction between these two will continue to be made throughout the thesis.

In addition to developing the simulation technique, several validations of it have also been made. Numerical data was matched to several simple analytical calculations, with good results. Three distinct zones were found to be present in the propagation geometry, applicable results were matched to the appropriate probability density functions in each region. Further to these numerical results, simple analysis has been

used to provide a justification for the asymptotic behaviour of the normalised second moment of the *J* statistic and the Huygens Fresnel principle was used to derive the form for the scintillation index in a weak corrugated phase screen problem.

With these techniques, and appropriate validation of these techniques, at our disposal, they can be used to model wave propagations in more complex situations. The next chapter will provide an investigation of the properties of the *J* statistic in the case of a constant phasor plus a Gaussian field (this is known as the Rician field). A combination of analysis and numerical techniques will be used.

3. The Intensity-weighted phase derivative in a Rician field.

A Rician field is characterised as a coherent signal in the presence of noise whose statistics are described by a circular Gaussian process. One can model a field that has been propagated into the Fraunhofer zone as being Rician in nature; identifying the constant part of the field with the unperturbed wave components and the Gaussian with the diffracted wave. The properties of the phase, phase derivative and intensity weighted phase derivative in such a field are considered in this chapter. This is a subject that has received little attention in the literature.

Jakeman et al [16] considered the properties of the *J* statistic in a Gaussian process, they calculated the probability density function and normalised second moment under strong turbulence conditions. In this chapter the Rician process is considered, which is a more general case. The circular Gaussian process is a subset of the Rician field, and for strong levels of turbulence one expects to recover Gaussian statistics. The properties of *J* in a Rician field are investigated, in doing this Rice's work of 1943 [13] is extended to include a phase screen formulation. The autocorrelation function of the phase derivative in a Rician field is also looked at; which, being the Fourier transform of the power spectrum, is a useful measure in systems that use phase derivative statistics. Finally, in this chapter, the profile for the normalised second moment of the *J* statistic is derived under weak turbulence conditions.

Care is taken to compare and contrast results with numerical simulations. Two-dimensional simulations are used and restricted to plane wave propagation. Phase derivative statistics are obtained by equating the phase difference in the spatial domain with the derivative in the temporal domain.

The chapter commences with a derivation of the joint pdf for the amplitude *A* and the intensity-weighted phase derivative *J*. Rice [13] showed that the joint probability distribution for the amplitude *A* and phase derivative $\dot{\theta}$, of Gaussian noise coherently added to a constant phasor, is

$$P\left(A,\dot{\theta}\right)=\frac{A^2}{2\pi b_0}\sqrt{\frac{2\pi}{b_2}}\exp\left[-\left(\frac{1}{b_0}+\frac{\dot{\theta}^2}{b_2}\right)\frac{A^2}{2}-\frac{Q^2}{2b_0}\right]I_0\left(\frac{AQ}{b_0}\right), \tag{3.1}$$

where, following the notation of Rice, Q is the amplitude of the constant phasor, b_0 the variance of the total field b_2 the derivative of the correlation function of the total field and I_0 the modified Bessel function of the first kind. The intensity weighted phase derivative is $J = I\dot{\theta} = A^2\dot{\theta}$ (section 1.2), and so equation (3.1) can be rewritten in terms of A and J:

$$P(A,J)=P\left(A,\dot{\theta}\right)\times\left\|J_{A,\dot{\theta}}\right\| \tag{3.2}$$

where the Jacobian

$$\left\|J_{A,\dot{\theta}}\right\|=\begin{Vmatrix}\frac{\partial A}{\partial A} & \frac{\partial A}{\partial J}\\ \frac{\partial\dot{\theta}}{\partial A} & \frac{\partial\dot{\theta}}{\partial J}\end{Vmatrix}=\begin{Vmatrix}1 & \frac{A}{2J}\\ \frac{-2J}{A^3} & \frac{1}{A^2}\end{Vmatrix}=\frac{2}{A^2} \tag{3.3}$$

$$\Rightarrow P(A,J)=\frac{1}{\pi b_0}\sqrt{\frac{2\pi}{b_2}}I_0\left(\frac{AQ}{b_0}\right)\exp\left[-\frac{1}{2}\left(\frac{A^2}{b_0}+\frac{J^2}{A^2b_2}\right)-\frac{Q^2}{2b_0}\right]. \tag{3.4}$$

3.1. Statistical properties of *J* in a Rician field.

In this section several results that characterise the J statistic in a Rician field will be derived, namely the pdf of J and the moments of the statistic. The results are in terms of phase screen parameters, allowing quantitative matching between simulation and theory.

3.1.1 The pdf of the intensity-weighted phase derivative in a Rician field.

The marginal distribution for J is obtained by integration the joint distribution (3.4) over all amplitudes

$$P(J)=\int_0^\infty P(A,J)dA=\frac{1}{\pi b_0}\sqrt{\frac{2\pi}{b_2}}\exp\left[-\frac{Q^2}{2b_0}\right]\int_0^\infty \exp\left[-\frac{1}{2}\left(\frac{A^2}{b_0}+\frac{J^2}{A^2b_2}\right)\right]I_0\left(\frac{QA}{b_0}\right)dA\,. \quad (3.5)$$

This can be evaluated by noting that [32]

$$I_0(x)=\sum_{n=0}^{\infty}\frac{x^{2n}}{4^n n!^2} \quad (3.6)$$

and integrating term by term

$$P(J)=\frac{1}{\pi b_0}\sqrt{\frac{2\pi}{b_2}}\exp\left[-\frac{Q^2}{2b_0}\right]\sum_{n=0}^{\infty}\left\{\left(\frac{Q}{2b_0}\right)^{2n}\times \mathrm{K}\ \mathrm{K}\frac{1}{n!^2}\int_0^\infty A^{2n}\exp\left[-\frac{1}{2}\left(\frac{A^2}{b_0}+\frac{J^2}{A^2b_2}\right)\right]dA\right\}. \quad (3.7)$$

The following integral:

$$\int_0^\infty A^{2n}\exp\left[-\frac{1}{2}\left(\frac{A^2}{b_0}+\frac{J^2}{A^2b_2}\right)\right]dA=K_{n+\frac{1}{2}}\left(\sqrt{\frac{J^2}{b_0b_2}}\right)\left(\frac{1}{b_0}\right)^{-\frac{1}{4}(1+2n)}\left(\frac{b_2}{J^2}\right)^{-\frac{1}{4}(1+2n)} \quad (3.8)$$

where K_i is the modified Bessel function of the second kind of order i, and enables the pdf of J in a Rician field to be written as

$$P(J)=\frac{1}{\pi b_0}\sqrt{\frac{\pi}{2b_2}}\exp\left[-\frac{Q^2}{2b_0}\right]\sum_{n=0}^{\infty}\left\{K_{n+\frac{1}{2}}\left(\sqrt{\frac{J^2}{b_0b_2}}\right)\left(\frac{Q}{2b_0}\right)^{2n}\frac{1}{n!^2}\left(\frac{b_2}{b_0J^2}\right)^{-\frac{1}{4}(1+2n)}\right\}. \quad (3.9)$$

To test computer simulation with theory, the parameters appearing in equation (3.9) must be expressed in terms of quantities appearing in phase screen models. The phase screen parameters are the mean squared phase shift imparted by the screen ϕ_0, and the correlation length of the screen ξ. The three parameters characterising the Rician field are Q, b_0 and b_2, which can be written as

$$Q = \left|\left\langle E^{+}\right\rangle\right| = \exp\left(-\frac{\phi_0^2}{2}\right) \tag{3.10}$$

$$b_0 = Var\left(\mathrm{Re}\, E^{+}\right) = \frac{1}{2}\left(1-\exp\left(-\phi_0^2\right)\right) \tag{3.11}$$

$$b_2 = -\frac{1}{2}\frac{\partial^2}{\partial t^2}\left\langle E(0)E*(t)\right\rangle_{t=0} = -\frac{\phi_0^2}{2}\frac{\partial^2}{\partial t^2}\left(\exp\left[-\phi_0^2\left(1-\rho(t)\right)\right]\right)_{t=0} \tag{3.12}$$

(3.10) and (3.11) are derived by Jakeman and McWhirter [4]. Equation (3.12) follows from the Huygens Fresnel integral

$$E(r_0,z) = \frac{i}{z\lambda}\int_{-\infty}^{\infty}\exp(i\phi(r))\exp\left(\frac{i\pi}{z\lambda}(r-r_0)^2\right)d^2r\,, \tag{3.13}$$

where the number of integrals performed is explicit from the integration variables. The correlation function of the field is

$$\begin{aligned}\left\langle EE'*\right\rangle &= \frac{1}{(z\lambda)^2}\int_{-\infty}^{\infty}\left\langle\exp(i[\phi(r)-\phi(r')])\right\rangle\exp\left(\frac{i\pi}{z\lambda}\left[(r-r_0)^2-(r'-r_0')^2\right]\right)d^2rd^2r' \\ &= \frac{1}{(z\lambda)^2}\int_{-\infty}^{\infty}\exp\left(-\phi_0^2\left(1-\rho(r-r')\right)\right)\exp\left(\frac{i\pi}{z\lambda}\left[(r-r_0)^2-(r'-r_0')^2\right]\right)d^2rd^2r' \\ &= \frac{1}{(2z\lambda)^2}\int_{-\infty}^{\infty}\exp\left(-\phi_0^2\left(1-\rho(v)\right)\right)\exp\left(\frac{i\pi}{z\lambda}[v-(r_0-r_0')][u-(r_0+r_0')]\right)d^2ud^2v\end{aligned}$$

$$\Rightarrow \left\langle EE'*\right\rangle = \exp\left(-\phi_0^2\left(1-\rho(r_0-r')\right)\right) \tag{3.14}$$

where $u = r + r'$ and $v = r + r'$ are sum and difference co-ordinates. The result $\left\langle\exp(i[\phi(r)-\phi(r')])\right\rangle = \exp\left(-\phi_0^2\left(1-\rho(r-r')\right)\right)$ is obtained by assuming the phase difference is a Gaussian variable, together with the well-known result of Gaussian noise theory, $\left\langle\exp(iA)\right\rangle = \exp\left(-\frac{1}{2}\left\langle A^2\right\rangle\right)$. To proceed further one must assume a form

for the autocorrelation function that characterises the phase screen. Assuming a Gaussian correlation function (equation (2.9)) for the phase screen gives $b_2 = \frac{\phi_0^2}{\xi^2}$.

A numerical evaluation of the first 50 terms in the sum contained in equation (2.9) provides an adequate estimation for $P(J)$ as the sum converges rapidly. The distribution can be plotted in terms of dimensionless variables by using $\sqrt{\langle J^2 \rangle} P\left(J \Big/ \sqrt{\langle J^2 \rangle} \right)$, in this way one can look at several regimes on one plot. Figure 3.1 gives two plots of equation (3.9), the bold line refers to $\phi_0 = 0.5$ (weak turbulence) while the thin line refers to $\phi_0 = 100$ (strong turbulence). Both plots use $\xi = 1000$.

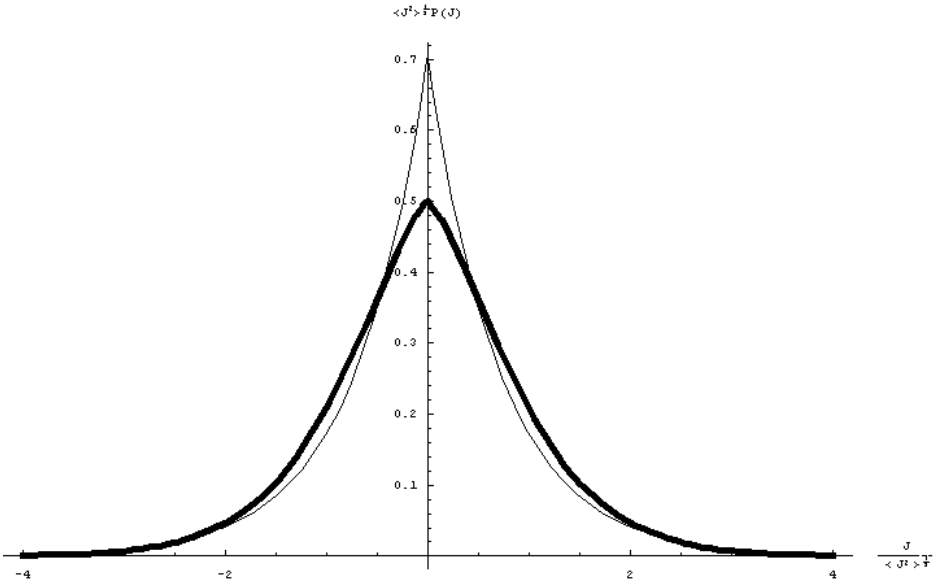

Fig. 3.1: Two pdf plots for P(*J*).

Figures 3.2 and 3.3 display the same graphs as in figure 1 on log / linear scales in order to make the structure of the tails visible. Numerical simulation is compared to theory.

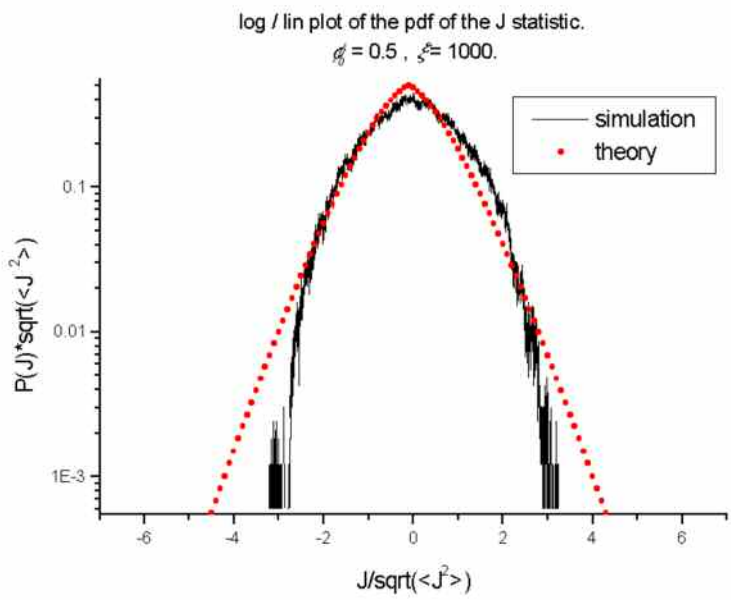

Fig. 3.2: pdf of the *J* statistic (simulation and theory) for ϕ_0 = 0.5 and ξ = 1000.

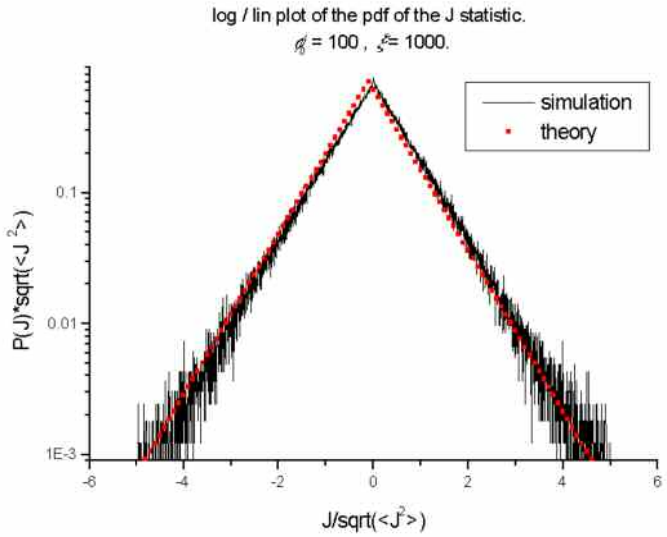

Fig. 3.3: pdf of the *J* statistic (simulation and theory) for ϕ_0 = 100 and ξ = 1000.

There is a good match between simulation and theory in figure 3.3. The behaviour in the tails in figure 3.3 is consistent with an exponential form; $P(J) \sim \exp(-|J|)$ (this is expected from Gaussian noise theory, see equation 1.13). Despite matching for $J \leq 2$, there is a difference between theory and simulation in the tails of figure 3.2. It is surmised that this is due to statistical measures failing to converge when performing simulations of weak turbulence in the Fraunhofer zone. Such problems were seen in section 2.5.2 and will be looked at in more detail in later sections.

3.1.2. Calculation of the characteristic function for the *J* statistic in the Rician field.

The characteristic function is an important tool in statistics. It is defined as the Fourier transform of the probability density function, from it the moments of the distribution can be easily obtained. For *J* in a Rician field one cannot directly perform the Fourier transform of the pdf given in equation (3.9), one can obtain the characteristic function directly from the joint pdf for *A* and $\hat{\theta}$ (3.1). The characteristic function is

$$C_J(u) = \langle \exp(iuJ) \rangle = \left\langle \exp\left(iuA^2\hat{\theta}\right) \right\rangle = \int_0^\infty dA \int_{-\infty}^{\infty} \exp\left(iuA^2\hat{\theta}\right) P\left(A,\hat{\theta}\right) d\hat{\theta} \tag{3.15}$$

$$\begin{aligned}
\Rightarrow C_J(u) &= \exp\left(-\frac{Q^2}{2b_0}\right) \int_{-\infty}^{\infty} A^2 I_0\left(\frac{AQ}{b_0}\right) \exp\left\{-\frac{A^2}{2b_0}\right\} dA \int_{-\infty}^{\infty} \cos\left(uA^2\hat{\theta}\right) \exp\left\{-\frac{A^2}{2}\frac{\hat{\theta}^2}{b_2}\right\} d\hat{\theta} \\
&= \exp\left(-\frac{Q^2}{2b_0}\right) \sqrt{2b_2\pi} \int_{-\infty}^{\infty} A I_0\left(\frac{AQ}{b_0}\right) \exp\left\{-A^2\left(\frac{1}{2b_0} + \frac{u^2 b_2}{2}\right)\right\} dA \\
&= \frac{1}{1+u^2 b_2 b_0} \exp\left(-\frac{Q^2}{2b_0}\right) \exp\left(\frac{Q^2}{2b_0}\left[\frac{1}{1+u^2 b_2 b_0}\right]\right)
\end{aligned}$$

resulting in

$$C_J(u) = \frac{1}{\left(1+u^2 b_2 b_0\right)} \exp\left(\frac{-Q^2 u^2 b_2}{2\left(1+u^2 b_2 b_0\right)}\right) \tag{3.16}$$

such that (3.16) and (3.9) constitute a Fourier pair. The characteristic function is used to calculate the moments of the *J* statistic in the following way:

$$C_J(u) = \langle \exp(iuJ) \rangle = \left\langle 1 + iuJ - \frac{u^2}{2} J^2 + \ldots \right\rangle = 1 + iu\langle J \rangle - \frac{u^2}{2}\left\langle J^2 \right\rangle + \ldots \tag{3.17}$$

Note from (3.16) that the characteristic function is a function of u^2, thus all odd moments are zero, this is also seen from the fact that the distribution of J is symmetric. The 2nd and 4th order moments of the J statistic are

$$\left\langle J^2 \right\rangle = -\frac{\partial^2}{\partial u^2} C_J(u)_{u=0} = 2b_0 b_2 \left(1 + \frac{Q^2}{2b_0}\right) \tag{3.18}$$

and

$$\left\langle J^4 \right\rangle = \frac{\partial^4}{\partial u^4} C_J(u)_{u=0} = 24 b_2^2 b_0^2 \left(1 + \frac{Q^2}{b_0} + \frac{Q^4}{8b_0^2}\right). \tag{3.19}$$

It is possible to express the characteristic function for J in terms of the Laguerre polynomials, thus allowing for a general expression for the n^{th} moment to be obtained The Laguerre polynomials are defined in terms of the generating function [32]

$$\frac{1}{1-z}\exp\left(\frac{xz}{z-1}\right) = \sum_{n=0}^{\infty} L_n(x) z^n \ . \tag{3.20}$$

Identifying $z = -u^2 b_0 b_2$ and $x = -\dfrac{Q^2}{2b_0}$ obtains equation (3.16),

$$C_J(u) = \sum_{n=0}^{\infty} L_n\left(-\frac{Q^2}{2b_0}\right)\left(-u^2 b_0 b_2\right)^n \ , \tag{3.21}$$

the characteristic function. This expression can be exploited to find the moments of J in similar terms. The odd moments of J are known to be zero since equation (3.9) is an even function, hence consider the $2n^{th}$ moment only:

$$\left\langle J^{2n} \right\rangle = 2n!\left(b_0 b_2\right)^n L_n\left(-\frac{Q^2}{2b_0}\right). \tag{3.22}$$

The normalised forth moment, $\left\langle J^4 \right\rangle \Big/ \left\langle J^2 \right\rangle^2$, can be used, in addition to the normalisation used by Jakeman et al in [16], e.g. $\left\langle J^2 \right\rangle \Big/ \left\langle J^2 \right\rangle_{z=0}$, as a measure of the scintillation in the field. This moment may result in improved statistics if illumination is by anything other than a plane wave. The form of the normalised forth moment of the *J* statistic is

$$\frac{\left\langle J^4 \right\rangle}{\left\langle J^2 \right\rangle^2} = 6\frac{\left\{1+\frac{Q^2}{b_0}+\frac{Q^4}{8b_0^2}\right\}}{\left\{1+\frac{Q^2}{b_0}+\frac{Q^4}{4b_0^2}\right\}}, \tag{3.23}$$

which, using phase screen parameters, is

$$\frac{\left\langle J^4 \right\rangle}{\left\langle J^2 \right\rangle^2} = \frac{6\left[1+\frac{2e^{-\phi_0^2}}{1-e^{-\phi_0^2}}+\frac{4e^{-2\phi_0^2}}{8\left(1-e^{-\phi_0^2}\right)^2}\right]}{\left(1+\frac{e^{-\phi_0^2}}{1-e^{-\phi_0^2}}\right)^2}. \tag{3.24}$$

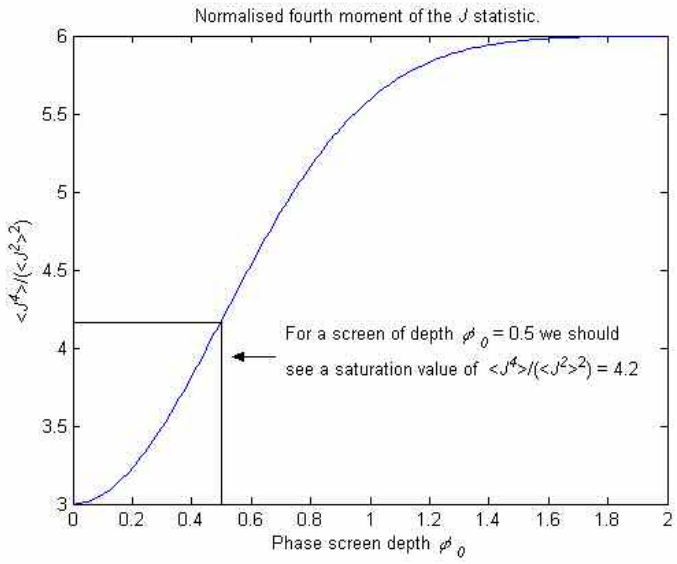

Fig. 3.4. Normalised fourth moment of the *J* statistic.

Equation (3.24) is plotted in figure 3.4 (above) as a function of the mean square phase shift ϕ_0. The plot gives, as function of screen strength, the value to which the normalised forth moment will saturate in the Fraunhofer zone. The saturation value is close to 3 for a weak screen and tends to 6 for a strong screen. As the strength of the phase screens increase, the statistics of the propagation problem tend towards Gaussian saturation. Figure 3.4 indicates the expected saturation value for a phase screen of strength $\phi_0 = 0.5$.

3.1.3. Comparison of theory with phase screen simulation.

Simulations in this section use a simple two-dimensional propagation algorithm (intorduced in chapter 2) to investigate the properties of the *J* statistic. In order to do this, the normalised moments $\left\langle J^4 \right\rangle \Big/ \left\langle J^2 \right\rangle^2$ and $\left\langle J^2 \right\rangle \Big/ \left\langle J^2 \right\rangle_{z=0}$ are considered. The simulations use 1000 realisations at each propagation distance (to improve statistical accuracy), each phase screen is sampled by 2^{14} points, ξ = 1000. Firstly, weak turbulence is considered.

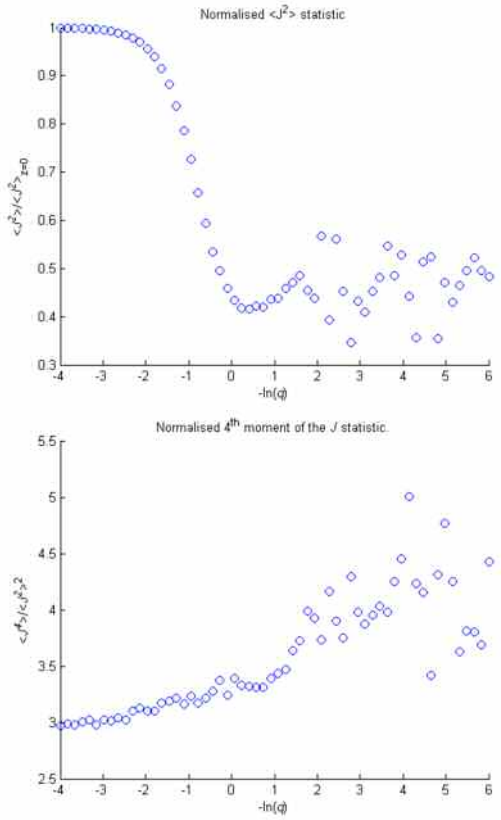

Figs 3.5 (second moment) and 3.6 (forth moment); moments of the *J* statistic for ϕ_0 = 0.5.

Figures 3.5 and 3.6 show the results of a set of simulations carried out using a Gaussian correlated screen with ϕ_0 = 0.5, the two normalised moments of *J* have been calculated for a range of propagation distances. The dimensionless length parameter, $q = \frac{k\xi^2}{2z\phi_0\sqrt{6}}$ (defined in section 2.5), is used. One can see the saturation value of the two moments in the Fraunhofer zone ($-\ln(q) \geq 4$), in figure 3.5 the normalised second moment tends to ½ while in figure 3.6 the normalised fourth moment tends to a value between 4 and 4.5. This result corroborates the prediction made by equation (3.24) regarding the saturation value of $\langle J^4 \rangle / \langle J^2 \rangle^2$.

The scatter present in both figures is due to weak screen simulations tending to have a greater spread on their statistics than deep screen equivalents. Note also that in using higher order statistics one is likely to see much more scatter in the data. A second set of simulations with ϕ_0 = 10 are shown in figures 3.7 and 3.8. These simulations give a very different picture, the saturation value is 6 for the fourth moment and ½ for the second moment.

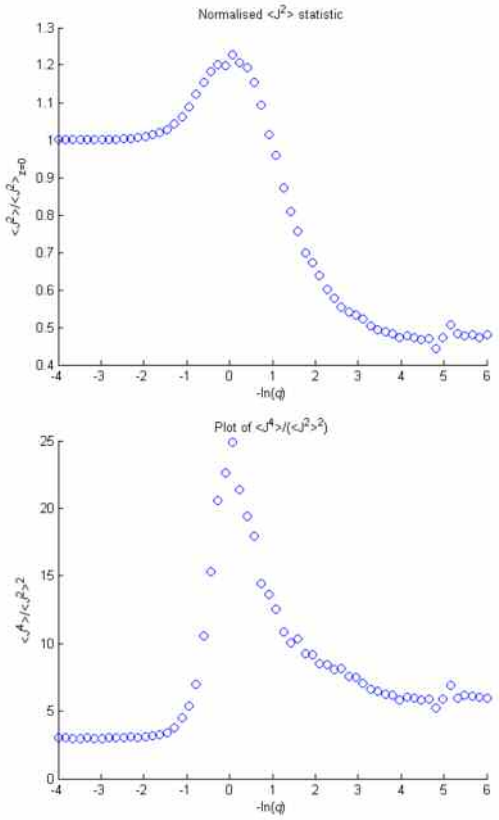

Figs 3.7 (second moment) and 3.8 (forth moment); normalised moments of *J* for $\phi_0 = 10$.

The existence of peaks in the curves, in contrast to a steady increase in figures 3.5 and 3.6, indicate the presence of a focussing regime as would be expected for a higher ϕ_0. Note also how, in comparison to figures 3.5 and 3.6, there is much less scatter in the statistics. This is an indication of the improved convergence of statistics in simulations that use stronger turbulence as opposed to weak turbulence.

3.1.4. Conclusions.

The properties of the intensity-weighted phase derivative in a Rician field have been investigated. The probability density and characteristic functions for *J* under such conditions have been derived and compared to appropriate computer simulations. In the Fraunhofer zone simulation results accurately match the predictions made by analytical calculations. Problems relating to the convergence of statistics under weak turbulence conditions have also been noted.

3.2. The correlation function of the phase derivative in a Rician field.

Use of the phase derivative as a measurement tool in coherent radiation systems has been considered by several authors in different fields of expertise [4, 16, 21, 13, 30, 65, 66]. One of the most important measures in an stochastic system is the power spectrum. The power spectrum of a stochastic process is defined [36] as the Fourier transform of the correlation function of that process; therefore it is instructive to study the correlation function of the phase derivative $\dot{\phi}$ under various turbulence conditions. In this section the properties of the correlation function of $\dot{\phi}$ are considered in the case of a Rician field.

3.2.1. Analysis.

Rice [13] derived an expression for the correlation function $\Omega(\tau)$ of the phase derivative in a Rician field

$$\Omega(\tau) = \frac{g'^2 - gg''}{2g^2} y_1 - \frac{g'^2}{2g^2} y_2, \tag{3.25}$$

where $g(\tau)$ is the correlation function of the real (or imaginary) part of the field, primes indicate a derivation with respect to time and y_1 and y_2 (see equations (3.29) and (3.30) respectively) are defined in terms of the properties of the field and are also functions of τ. These results are now adapted to include a formulation based on phase screen parameters. $g(\tau)$ is defined slightly differently than the correlation function given in equation (3.12) because $g(\tau)$ is the correlation function of the real part of the field $X(\tau)$, rather than the total field $E(\tau)$. Therefore

$$\begin{aligned} g(\tau) &= \langle X(0)X(\tau)\rangle = \frac{1}{2}\left\langle \left(E - \langle E\rangle\right)\left(E'^* - \langle E'^*\rangle\right)\right\rangle = \frac{1}{2}\left[\langle EE'^*\rangle - \langle E\rangle\langle E^*\rangle\right] \\ &= \frac{1}{2}\left\{\exp\left(-\phi_0^2[1-\rho(\tau)]\right) - \exp\left(-\phi_0^2\right)\right\} \end{aligned}. \tag{3.26}$$

Assuming a Gaussian form for the autocorrelation function (equation 2.9); the expression for $\Omega(\tau)$ becomes

$$\Omega(\tau)=\frac{2\phi_0^2}{\xi^2}\left\{\left(\frac{1}{2}-\frac{\tau^2}{\xi^2}\right)\exp\left(-\frac{\tau^2}{\xi^2}\right)y_1-\frac{\phi_0^2}{\xi^2}\tau^2\exp\left(-\frac{2\tau^2}{\xi^2}\right)y_2\right\} \tag{3.27}$$

$$\Rightarrow\frac{\xi^2}{2\phi_0^2}\Omega\left(\frac{\tau}{\xi}\right)=\Omega'(\tau')=\left(\frac{1}{2}-\tau'^2\right)\exp\left(-\tau'^2\right)y_1-\phi_0^2\tau'^2\exp\left(-2\tau'^2\right)y_2 \tag{3.28}$$

when written in terms of a normalised correlation time $\tau'=\tau/\xi$.

Rice defines y_1 and y_2 in terms of two variables p and k

$$y_1=\exp\left(-\frac{p}{k}\right)\left\{Ei\left[\frac{p}{k}\right]-2Ei\left[\frac{p(1-k)}{k}\right]+Ei\left[\frac{p(1-k)}{k(1+k)}\right]\right\} \tag{3.29}$$

$$y_2=\frac{p}{k}y_1-1+\frac{2}{1-k}\exp(-p)-\frac{1+k}{1-k}\exp\left(\frac{-2p}{1+k}\right) \tag{3.30}$$

where

$$p=\frac{Q^2}{2b_0}=\frac{\exp\left(-\phi_0^2\right)}{1-\exp\left(-\phi_0^2\right)} \tag{3.31}$$

$$k=\frac{g(\tau)}{b_0}=\frac{\exp\left(-\phi_0^2\right)\left(\exp\left[\phi_0^2\rho(\tau)\right]-1\right)}{1-\exp\left(-\phi_0^2\right)}=p\left(\exp\left[\phi_0^2\rho(\tau)\right]-1\right) \tag{3.32}$$

when defined in terms of the phase screen parameters. The exponential integral $Ei(x)=\int_{-\infty}^{x}e^t/t\,dt$. The integrand has a singularity at $t = 0$, so Cauchy's principal value theorem [22] is required to evaluate the integral for $x > 0$. Doing this allows for the numerical evaluation of $\Omega'(\tau')$. Figures 3.9 and 3.10 give $\Omega'(\tau')$ for two weak phase screen cases.

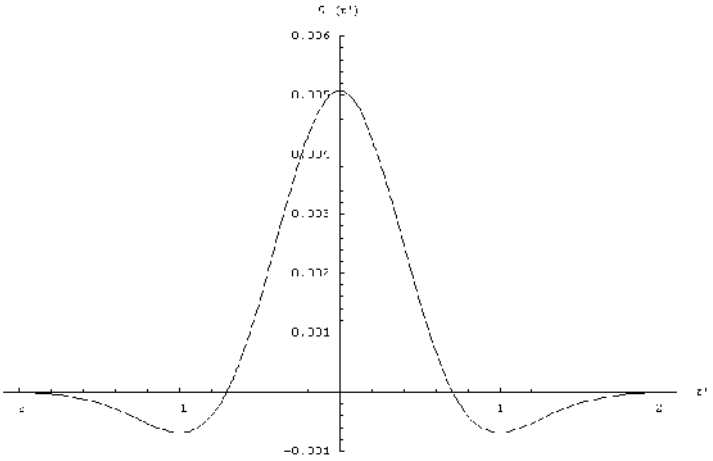

Fig. 3.9: Correlation function $\Omega'(\tau')$ for ϕ_0 = 0.1.

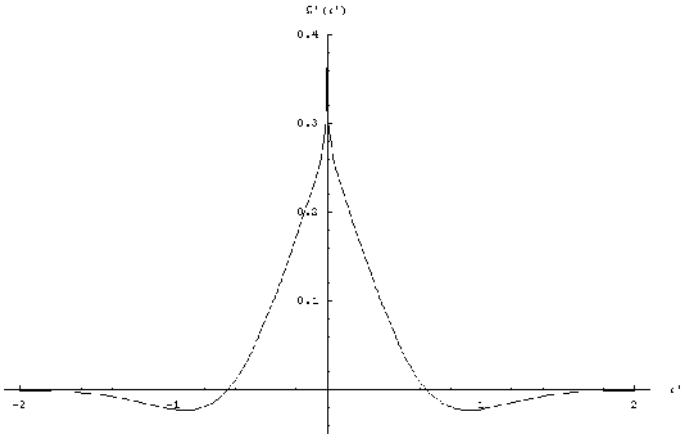

Fig. 3.10: Correlation function $\Omega'(\tau')$ for ϕ_0 = 0.5.

The correlation function is plotted with respect to τ'. As the strength of the turbulence increases, the centre of the correlation function tends to a cusp, indicating possible fractal-like behaviour (section 3.2.3) in the phase derivative. Consider now $\Omega'(\tau')$ for stronger levels of turbulence, figure 3.11 shows the correlation function for $\phi_0 = 1.5$.

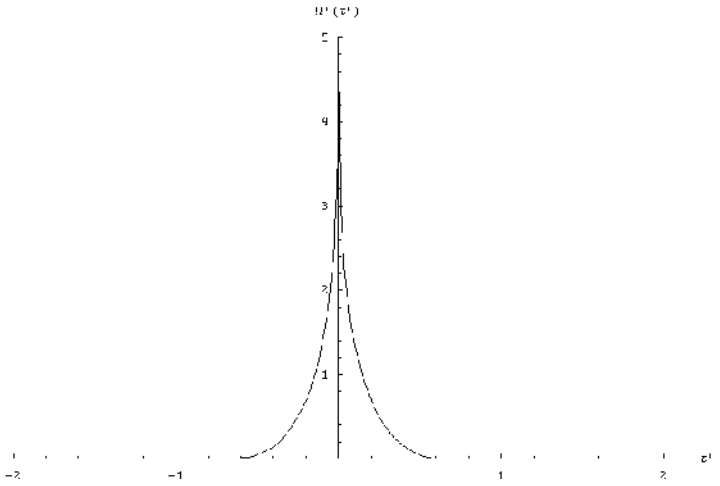

Fig. 3.11: Correlation function $\Omega'(\tau')$ for $\phi_0 = 1.5$.

As ϕ_0 increases, a cusp appears to be visible at $\tau' = 0$. There is weak correlation for very weak screens while the correlation function, at $\tau' = 0$, continues to increase into a cusp-like feature as the strength of the phase screens increases. One eventually reaches a value of ϕ_0 where the numerical evaluation of *Ei(x)* becomes problematic. In order to investigate this region it is necessary to find a large ϕ_0 expansion for $\Omega'(\tau')$.

3.2.2. Investigation of $\Omega'(\tau')$ for large ϕ_0.

Consider first the behaviour of *k* and *p* (as given by equations (3.29) and (3.30)) for large ϕ_0. Both *p* and *k* tend to 0 for large values of ϕ_0, note, however, that for $\tau' = 0$, $k = 1$ for all values of ϕ_0. $\Omega'(\tau')$ can be simplified by using a series expansion for the exponential integral

$$Ei(x) = \int_{-\infty}^{x} \frac{\exp(t)}{t} dt = C + \frac{1}{2}\ln(x^2) + \sum_{n=1}^{\infty} \frac{x^n}{n.n!} \qquad (3.33)$$

where Euler's constant $C \approx 0.577$. Now expand equation (3.29) using equation (3.33), this gives

$$y_1 = \exp\left(-\frac{p}{k}\right)\left\{\frac{1}{2}\ln\left(\frac{p}{k}\right)^2 - \ln\left(\frac{p(1-k)}{k}\right)^2 + \frac{1}{2}\ln\left(\frac{p(1-k)}{k(1+k)}\right)^2 + \frac{p}{k} + \frac{p^2}{4k^2} - \frac{2p(1-k)}{k} - \frac{p^2(1-k)^2}{k^2} + \frac{p(1-k)}{k(1+k)} + \frac{p^2(1-k)^2}{4k^2(1+k)^2}\right\} \tag{3.34}$$

$$y_1 = \exp\left(-\frac{p}{k}\right)\left\{-\ln(1-k) - \ln(1+k) + \frac{p}{k} + \frac{p^2}{4k^2} - \frac{2p(1-p)}{k} - \frac{p^2(1-p)^2}{k^2} + \frac{p(1-k)}{p(1+k)} + \frac{p^2(1-k)^2}{4p^2(1+k)^2}\right\} \tag{3.35}$$

recalling that $p = 0$ for all $\phi_0 >> 1$, this expression reduces to Rice's result [13]

$$y_1 = -\exp\left(-\frac{p}{k}\right)\ln[(1-k)(1+k)] \approx -\ln\left[1-k^2\right]. \tag{3.36}$$

One can show that $y_2 \to 0$ for all $\phi_0 >> 1$ (Appendix C). Therefore a modified expression for $\Omega'(\tau')$ is

$$\Omega'(\tau') = -\left(\frac{1}{2} - \tau'^2\right)\exp\left(-\tau'^2\right)\ln\left(1-k^2\right) \tag{3.37}$$

which is valid for all τ' such that $\phi_0 >> 1$ and that the autocorrelation function characterising the screen is smooth.

This expression can be plotted for all values of $\phi_0 > 1$ without using Cauchy's principal value theorem. Figure 3.12 (below) gives plots for $\phi_0 = 2$ and $\phi_0 = 5$. As ϕ_0 increases a peak is maintained at the origin, but the spread of the function decreases with increasing ϕ_0. The plots for each turbulence strength have similar shapes, the plot for $\phi_0 = 2$ tails off to zero at $\tau' \approx 1/2$, while the plot for $\phi_0 = 5$ does so at $\tau' \approx 1/4$

.

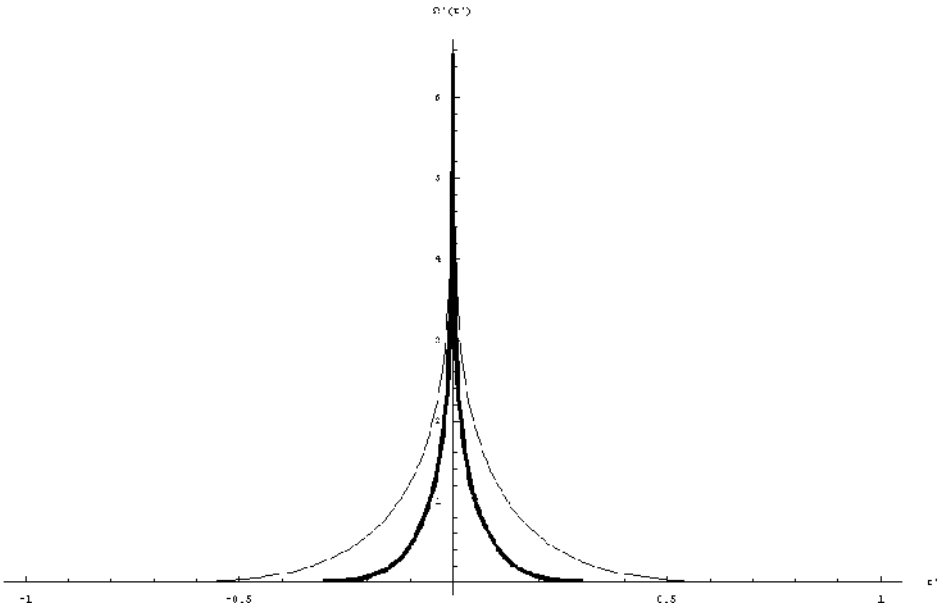

Fig. 3.12: $\Omega'(\tau')$ thicker line is for ϕ_0 = 5, thinner line is for ϕ_0 = 2.

Figure 3.13 gives a plot for ϕ_0 = 100; once again the correlation function appears to come to a single cusp at τ' = 0. Although $\Omega'(\tau')$ approaches a constant value for increasing ϕ_0, the value of the correlation function $\Omega(\tau') = \frac{2\phi_0^2}{\xi^2}\Omega'(\tau')$ is increasing with higher screen depths.

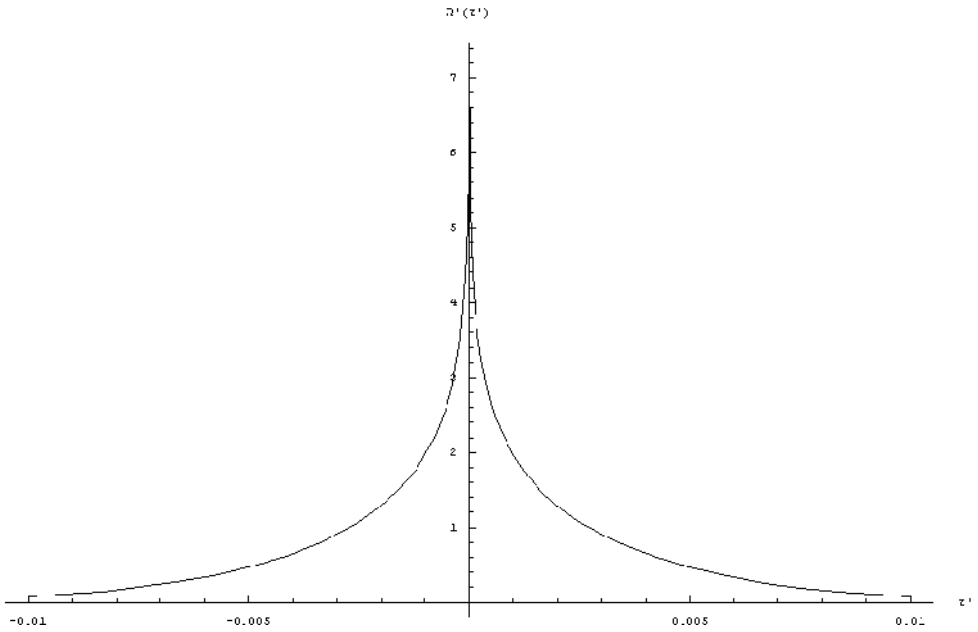

Fig. 3.13: Correlation function $\Omega'(\tau')$ for ϕ_0 = 100.

3.2.3. Limit for $\Omega'(\tau')$ as $\tau' \to 0$ for large ϕ_0.

A simple expansion for $\Omega'(\tau')$ can be derived for $\tau \approx 0$ and large ϕ_0. Assuming small τ' one can write the parameter *k* (equation 3.32) as

$$k \approx \frac{1-\tau'^2\phi_0^2-\exp\left(-\phi_0^2\right)}{1-\exp\left(-\phi_0^2\right)} \approx 1-\tau'^2\phi_0^2 \tag{3.38}$$

which is valid if ϕ_0 is large. Using this expression in $\Omega'(\tau')$ (equation (3.37)) gives

$$\Omega'(\tau') \approx \left(-\frac{1}{2}-\tau'^4+\frac{3}{2}\tau'^2\right)\ln\left(2\phi_0^2\tau'^2-\phi_0^4\tau'^4\right), \tag{3.39}$$

which on taking the limit $\tau' \to 0$ gives

$$\Omega'(\tau') \approx -\frac{1}{2}\ln\left(2\phi_0^2\tau^2\right) = -\ln\left(\sqrt{2}|\phi_0\tau'|\right) \tag{3.40}$$

which shows that the correlation function has a logarithmic singularity at the origin.

3.2.4. Numerical simulation of $\Omega'(\tau')$.

Numerical simulation is used to test the above results. These simulations were performed using phase screens with a Gaussian correlation function, with correlation length ξ = 1000. The correlation function for the phase derivative is calculated by taking the fast Fourier transform of the phase derivative power spectrum

$$\Omega'(\tau') = \int_{-\infty}^{\infty} \exp(-i\omega x)\left\{\left|\int_{-\infty}^{\infty} \exp(i\omega x)H(x)\not{\phi}(x)dx\right|^2\right\}d\omega\,. \tag{3.41}$$

Where $\not{\phi}(x)$ is the phase derivative data, *x* a spatial co-ordinate on the phase front, ω a phase space co-ordinate and $H(x)$ the Hanning window (see figure 3.14 below).

The phase derivative is found by taking the phase difference across the propagated wave front. A windowing technique is used in order to smooth the power spectrum before calculating $\Omega'(\tau')$. Windowing is an important technique in the calculation of power spectra, the data in a sample is multiplied by the windowing function, thus forcing the data at the edges of the sample to zero. It is a technique that will be used in chapters 4 and 5.

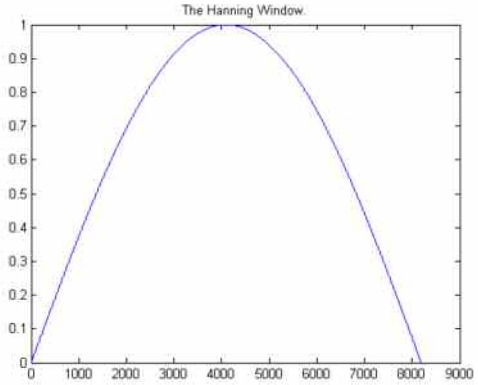

Figure 3.14: The Hanning window.

$H(x) = \cos(\pi(x - X/2)/X)$, where X is the number of samples and $x \in (0, X)$, is the Hanning window. The window removes discontinuities in the data at the edges of the sample. This process results in a much smoother spectrum which shows detailed structure more clearly. The use of windowing will incur a loss of power in the spectrum as the absolute values of the data are diminished, the clarity of features in the spectrum are improved though as the relative changes in the data remain unchanged.

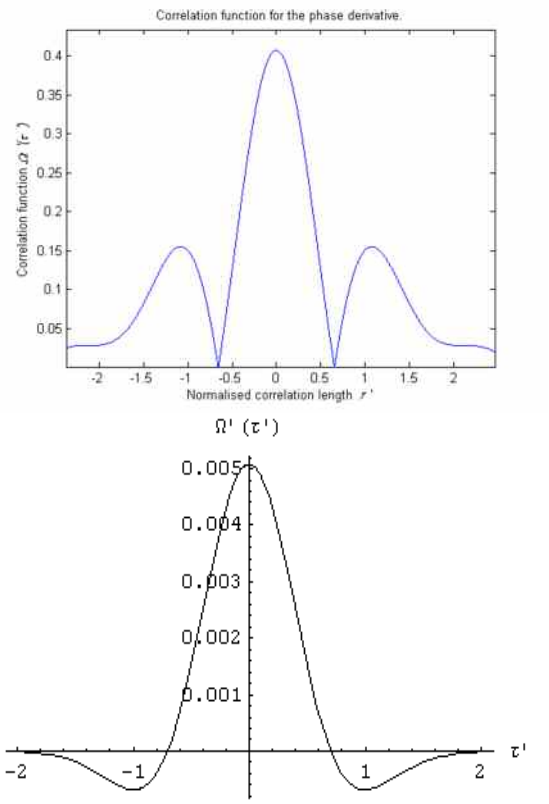

Figs 3.15 (simulation) and 3.16 (theory): Correlation functions for ϕ_0 = 0.1.

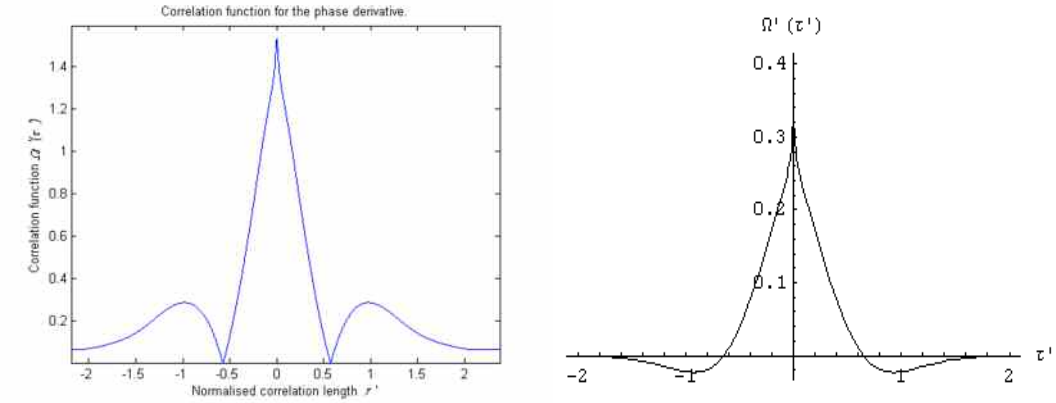

Figs 3.17 (simulation) and 3.18 (theory): Correlation functions for ϕ_0 = 0.5.

Figures 3.15 through 3.18 indicate a discrepancy of several orders of magnitude between simulation and theory, although there are some qualitative similarities. Possible explanations for these inconsistencies include the effect of the Hanning window, normalisation of the fast Fourier transform algorithm or the usual problems of statistical convergence encountered when performing simulations under conditions of weak turbulence.

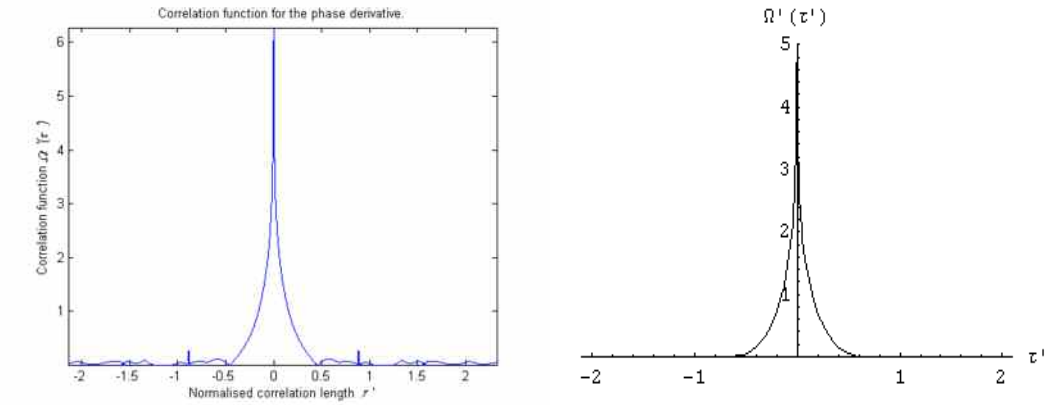

Figs 3.19 (simulation) and 3.20 (theory): Correlation functions for ϕ_0 = 1.5.

Figures 3.19 and 3.20, for a stronger level of turbulence, give a better match between simulation and theory. Figure 3.21 (below) shows the simulation results for still stronger levels of turbulence, ϕ_0 = 2 and ϕ_0 = 5. The simulations compare favourably with the theory in figure 3.12.

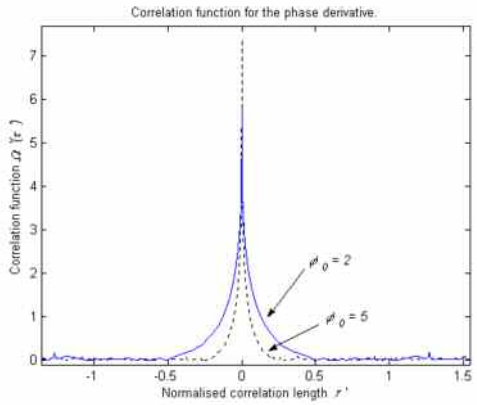

Fig. 3.21: Correlation functions for ϕ_0 = 2 and 5 (simulation).

Note especially the two tails and the value at which the two plots become indistinguishable. The function has reached a value of 0 at $\tau' \approx 1/2$ for ϕ_0 = 2 and $\tau' \approx 1/4$ for ϕ_0 = 5.

3.2.5. Concluding remarks.

The correlation function for the phase derivative has been derived for a Gaussian phase screen under both weak and strong turbulence conditions. Computer simulation has provided evidence for the accuracy of the work in the strong turbulence regime.

Difficulties have been encountered in obtaining numerical corroboration of the theory in the case of weak turbulence, complications concerning the convergence of statistics in such regimes have already been reported in section 3.1. The strong turbulence result (equations (3.37)) has proved the most successful, it accurately predicts the behaviour of the tails of the correlation function in both quantitative and qualitative terms.

The presence (equation (3.40)) of a logarithmic singularity in the auto-correlation function $\Omega'(\tau')$ implies a similar singularity in the structure function for the phase derivative, something which is a direct consequence of a 'marginal' fractal [83]. Such fractals occur when the structure function of a random process g is given by $D_g(\tau) \sim a\tau^{\nu}$ such that $0 < \nu < 2$ and $\nu = 2$ corresponds to deterministic (ballistic) motion. In the case that $\nu = 2 - \delta$ where $\delta \to 0$, the structure function has the form $D_g(\tau) \sim 1 - \delta \ln(\tau)$ and the auto-correlation function will therefore have a logarithmic singularity. This is interesting because the result is at the boundary between two distinctly different phases in the behaviour of g. As well as this fractal behaviour in the structure function, the probability distribution for the increments is at the margin of the class of scale invariant distributions. The Rician field recovers Gaussian statistics in the case of large ϕ_0 such that $P(\phi)$ follows a student-t (equation 1.10), a distribution with a cubic power law tail. This marginal distribution indicates fractal behaviour in the increments of the phase derivative.

Thus it has been shown that the phase derivative for a Rician field exhibits marginal behaviour (i.e. statistics that arise on the boundary between two phases of behaviour yet in neither) in two senses, that of the increments and the structure function. This is an interesting result as marginal behaviour has previously been found exclusively in either the increments or the structure function of a process g, not both.

3.3. Calculation of the second moment of J for a plane wave propagating through a single weak corrugated phase screen.

Hitherto in this chapter, work has been restricted to the phase derivative as modelled by a Rician field in the saturation regime. Consider now the J statistic at any propagation distance. Jakeman et al [16] found an expression for $\langle J^2\rangle / \langle J^2\rangle_{z=0}$ in the case of strong turbulence. The significance of $\langle J^2\rangle / \langle J^2\rangle_{z=0}$ as a statistic in measuring scintillation levels has been discussed in section 2.5.3. This section of the thesis provides a derivation of $\langle J^2\rangle / \langle J^2\rangle_{z=0}$ in the case of weak turbulence at any propagation distance z. It has been shown (section 2.5.3) that $\langle J^2\rangle / \langle J^2\rangle_{z=0} \to 1/2$ in the Fraunhofer zone (saturation regime), this derivation relied on the assumption that the field is described by a Gaussian circular process. The derivation that follows assumes weak turbulence, and therefore extends the work in section 2.5.3 to include the Rician field.

3.3.1. Normalised second moment of J for all z.

Consider a plane wave interacting with and propagating beyond a one-dimensional phase screen located at $z = 0$. The one-dimensional propagated field, at z , is given by the Huygens Fresnel integral

$$E(x,z) = i\sqrt{\frac{k}{2z\pi}}\int_{-\infty}^{\infty}\exp\left(\frac{ik}{2z}(x-s)^2 + i\phi(s)\right)ds, \qquad (3.42)$$

where s is an integration variable over the spatial domain, $\phi(s)$ the phase screen and k the wave number. Performing a co-ordinate transformation, $s \to s + ut$ where u is the speed of the phase screen across the wave front, and introducing a time co-ordinate t allows J to be is expressed as (see section 1.2)

$$J = \mathrm{Im}\left(E * \frac{\partial E}{\partial t}\right).$$

Substituting equation (3.42) yields

$$J = \frac{uk^2}{2\pi z^2}\int_{-\infty}^{\infty} ds_1 ds_2 (x - s_2 + ut)\times \\ \times\cos\left\{\frac{k}{2z}\left(-(x-s_1+ut)^2 + (x-s_2+ut)^2\right) - \phi(s_1+ut) + \phi(s_2+ut)\right\}.$$

Setting x = 0, valid for a plane wave, and performing a co-ordinate transform, $s \to s - ut$, gives

$$J = \frac{uk^2}{2\pi z^2}\int_{-\infty}^{\infty} ds_1 ds_2 s_2 \cos\left\{\frac{k}{2z}\left(-s_1^2 + s_2^2\right) - \phi(s_1) + \phi(s_2)\right\}.$$

From this one can write the second moment of J as

$$\left\langle J^2\right\rangle = \left(\frac{uk^2}{2\pi z^2}\right)^2 \int_{-\infty}^{\infty} s_2 s_4 \left\langle \cos\left\{\frac{k}{2z}\left(-s_1{}^2 + s_2{}^2\right) - \phi(s_1) + \phi(s_2)\right\}\times\ldots \right. \\ \left. \ldots\times\cos\left\{\frac{k}{2z}\left(-s_3{}^2 + s_4{}^2\right) - \phi(s_3) + \phi(s_4)\right\}\right\rangle \prod_{i=1}^{4} ds_i \qquad (3.43)$$

where now there are 4 integration variables labelled s_i. This expression can be simplified

$$\left\langle J^2\right\rangle \sim \int_{-\infty}^{\infty}\left\{ s_2 s_4 \left\langle \cos\left\{\frac{k}{2z}\left(-s_1{}^2 + s_2{}^2 - s_3{}^2 + s_4{}^2\right) - \phi(s_1) + \phi(s_2) - \phi(s_3) + \phi(s_4)\right\}\right\rangle \mathrm{K} \right. \\ \left. \mathrm{K} + s_2 s_4 \left\langle \cos\left\{\frac{k}{2z}\left(-s_1{}^2 + s_2{}^2 + s_3{}^2 - s_4{}^2\right) - \phi(s_1) + \phi(s_2) + \phi(s_3) - \phi(s_4)\right\}\right\rangle\right\} \prod_{i=1}^{4} ds_i$$

$$\left\langle J^2\right\rangle \sim \mathrm{Re}\int_{-\infty}^{\infty}\left\{ s_2 s_4 \exp\left\{\frac{ik}{2z}\left(s_2{}^2 - s_1{}^2 - s_3{}^2 + s_4{}^2\right)\right\}\left\langle \exp\left[i\phi(s_2) - i\phi(s_1) - i\phi(s_3) + i\phi(s_4)\right]\right\rangle + \right. \\ \left. \mathrm{K} + s_2 s_4 \exp\left\{\frac{ik}{2z}\left(s_2{}^2 - s_1{}^2 + s_3{}^2 - s_4{}^2\right)\right\}\left\langle \exp\left[-i\phi(s_1) + i\phi(s_2) + i\phi(s_3) - i\phi(s_4)\right]\right\rangle\right\} \prod_{i=1}^{4} ds_i$$

where the multiplier $\left(uk^2/2\pi z^2\right)^2$ has been dropped and the ensemble averages are restricted to phase screen terms. Employing the well known result of Gaussian noise theory, $\langle \exp(iA) \rangle = \exp\left(-\frac{1}{2}\langle A^2 \rangle\right)$, averaging over the phase screen elements and integrating out two of the of the integration variables results in [21]

$$\begin{aligned}\langle J^2 \rangle = -\frac{2\pi z}{k}\left(\frac{k^2 u}{2\pi z^2}\right)^2 \int_{-\infty}^{\infty} dxdy\left\{\frac{4z^2\phi_0^2}{k^2}\left(\frac{\partial^2\rho(x)}{\partial x^2}+\frac{\partial^2\rho(y)}{\partial y^2}\right)+x^2+y^2\right\}\times... \\ ...\times\cos\left[\frac{k}{z}xy\right]\exp\left[-\phi_0^2\{2-2\rho(x)-2\rho(y)+\rho(x+y)+\rho(x-y)\}\right]\end{aligned} \tag{3.44}$$

where $\rho(x)$ is the correlation function of the screen. The integration is completed in [21] for a deep phase screen (ϕ_0 >> 1) by assuming a Gaussian form for the correlation function and the use of 'function modelling'. Assuming weak turbulence (ϕ_0 << 1) allows for an expansion of exponential in equation (3.44),

$$\begin{aligned}\langle J^2 \rangle = -\frac{2\pi z}{k}\left(\frac{k^2 u}{2\pi z^2}\right)^2 \int_{-\infty}^{\infty} dxdy\left\{\frac{4z^2\phi_0^2}{k^2}\left(\frac{\partial^2\rho(x)}{\partial x^2}+\frac{\partial^2\rho(y)}{\partial y^2}\right)+x^2+y^2\right\}\times \\ \times\cos\left[\frac{k}{z}xy\right]\left[1-\phi_0^2\{2-2\rho(x)-2\rho(y)+\rho(x+y)+\rho(x-y)\}\right]\end{aligned} \tag{3.45}$$

Assuming a Gaussian correlation function for $\rho(x)$ (equation (2.9)) and noting a symmetry between *x* and *y* yields

$$\begin{aligned}\langle J^2 \rangle = -\frac{2\pi z}{k}\left(\frac{k^2 u}{2\pi z^2}\right)^2 \left\{\frac{8z^2\phi_0^2}{k^2}\int_{-\infty}^{\infty} dxdy\left(\frac{\partial^2\rho(x)}{\partial x^2}\right)\cos\left[\frac{k}{z}xy\right]h(x,y)+\mathrm{K}\right. \\ \left.\mathrm{K}+2\int_{-\infty}^{\infty} dxdyx^2\cos\left[\frac{k}{z}xy\right]h(x,y)\right\}\end{aligned} \tag{3.46}$$

where $h(x,y)=1-\phi_0^2\{2-2\rho(x)-2\rho(y)+\rho(x+y)+\rho(x-y)\}$. Performing each of the integrations gives the desired result, see appendix B for the full expression.

Performing a Taylor expansion of equation (B1) about $z = 0$ allows for a normalisation of the moment;

$$\left\langle J^2 \right\rangle_{z=0} \approx \frac{2\phi_0^2}{\xi^2}. \tag{3.47}$$

Equation (B1) is plotted in figure 3.22 using the normalisation in equation (3.47) several phase screen strengths are shown. The statistic is unity in the Fresnel zone while saturating to ½ in the Fraunhofer zone. This, of course, is the same limiting behaviour as for strong turbulence – see figure 2.11. There is no focussing regime corresponding to a maximum in $\left\langle J^2 \right\rangle / \left\langle J^2 \right\rangle_{z=0}$. This is similar to what has been seen in intensity scintillation statistics for weak turbulence (see section 2.5.2).

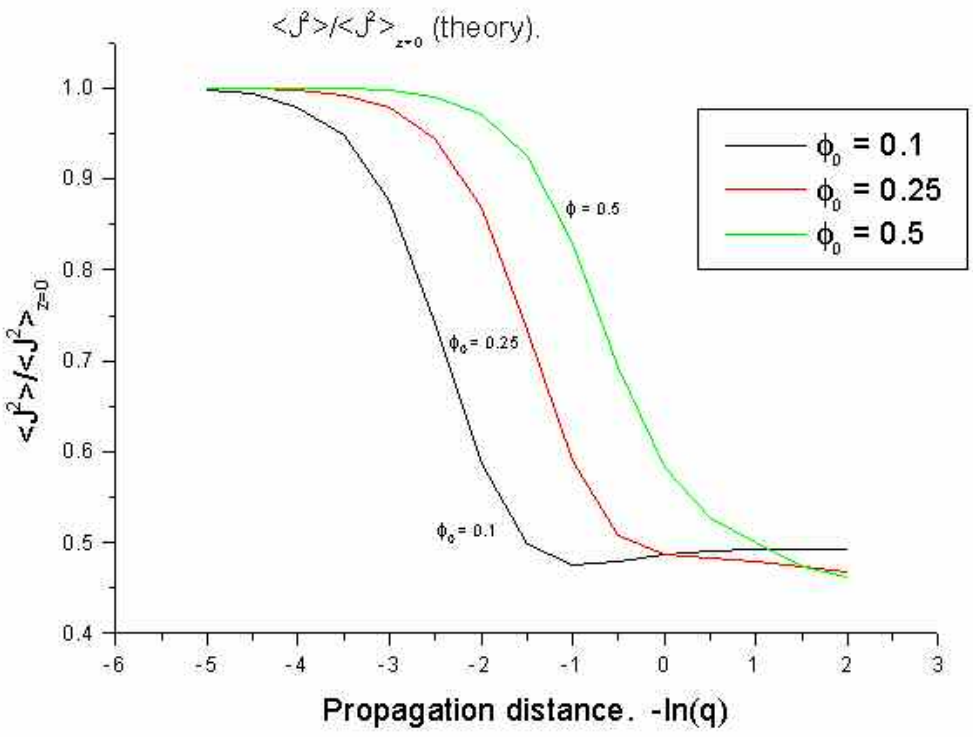

Fig. 3.22. The normalised second moment of the *J* statistic for a plane wave propagating through a weak phase-changing screen.

3.3.2. Computer simulation.

Numerical simulations were performed using a plane wave sampled by 2^{14} points. Constants used in the simulations were ξ = 1000, k = 500 and u = 1. Plots were produced showing $\left\langle J^2 \right\rangle / \left\langle J^2 \right\rangle_{z=0}$ for a range of propagation distances and a range of screens strengths. 300 realisations were used at each propagation distance in order to improve statistical accuracy. Figures 3.23 and 3.24 (below) indicate the comparison between theory and simulation for two weak screen propagations, ϕ_0 = 0.5 and ϕ_0 = 0.25. The theory slightly over-estimates the statistic in figure 3.23 at intermediate propagation distances while figure 3.24 indicates good correlation between theory and simulation.

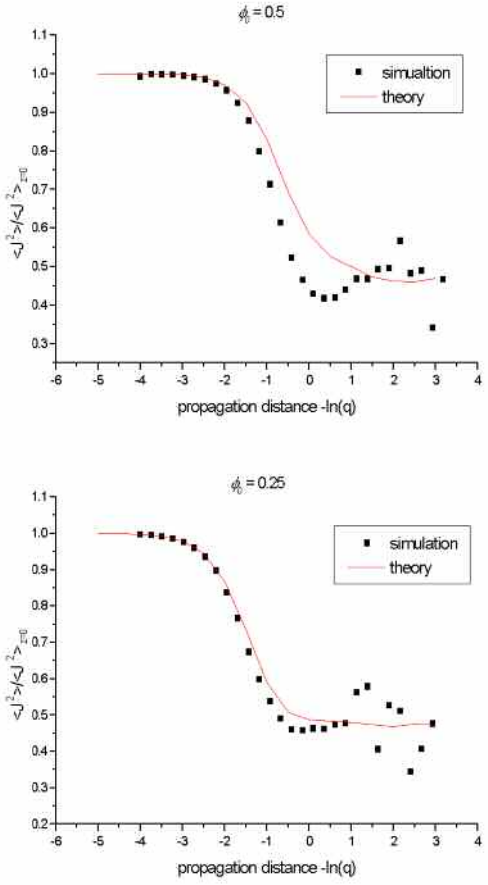

Figures 3.23 (ϕ_0 = 0.5) and 3.24 (ϕ_0 = 0.25), theory and simulation.

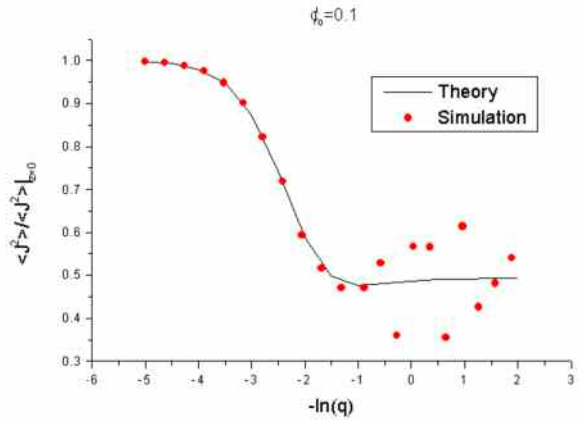

Fig. 3.25, simulation and theory (ϕ_0 = 0.1).

Figure 3.25 indicates the ϕ_0 = 0.1 case, there is good correlation between theory and simulation until the propagation approaches $-\ln(q) \approx 0$. The lack of convergence to saturated statistics under weak turbulence conditions is a phenomenon that has been discussed already in this chapter.

3.3.3. Conclusions.

An expression for the normalised second moment of the *J* statistic has been derived for all propagation distances *z*. Assumptions included the use of a Gaussian phase screen, weak turbulence and the Huygens Fresnel integral of wave diffraction. The far field behaviour of the moment in a Rician field equates to the behaviour of the statistic in a Gaussian circular process, i.e. $\left\langle J^2 \right\rangle / \left\langle J^2 \right\rangle_{z=0}$ saturates to ½. Computer simulation corroborates the analysis and once again shows evidence that statistics, under weak turbulence conditions, do not easily converge.

3.4. Conclusions.

This chapter has concentrated on phase derivative statistics in a Rician field. The Gaussian circular process is a subset of the Rician process, and plane wave propagating into the Fraunhofer zone can be modelled by such a process. Several properties of *J* have been derived for the Rician field, including the characteristic

function, probability density function and n^{th} moment in the far field. The derivation of the normalised second moment of J for all z has shown that the behaviour of that moment in the far field is identical to that of the Gaussian saturation regime.

The phase derivative was also considered and a derivation of the correlation function for $\not\partial$ performed. Simulated wave propagation showed good qualitative and quantitative agreement at strong levels of turbulence. Weakly turbulent simulations produced results which are more difficult to interpret due to high levels of spread in the statistics. It appears that even taking a large number of realisations fails to account for these problems. Given the discovery of doubly marginal behaviour in the phase derivative in a Rician field it may be possible to explain such problems in terms of the variances of such marginal distributions. The variance of such distributions does not exist due to the behaviour of the tails, thus the attempts presented in this chapter to measure the variance of the J statistic, a function of the phase derivative, may be inherently flawed. It may be impossible, using current algorithms and under conditions of weak turbulence, to perform numerical simulations of the 4^{th} or higher moments that converge to accurate statistics (see figures 3.6 and 3.8).

4. Phase Power Spectra, two-dimensional models.

The most crucial difference between a remote detection system using coherent radiation and one using direct detection is the availability of usable phase data. The retention of a 'beat' frequency at the transmission equipment allows an operator to detect frequency modulations in the received signal. Such modulations come in the form of vibrations and absorptions / emissions in the intervening medium and reflecting surfaces. One can look at the frequency data in the phase by looking at the spectral components of that phase via the power spectrum. The phase power spectrum $S_\theta(\omega)$ is defined (in terms of a frequency parameter ω) as the square of the absolute value of the Fourier transform of the phase $\theta(x)$,

$$S_\theta(\omega) = \left|\hat{\theta}(\omega)\right|^2 = \left|\int_{-\infty}^{\infty} \theta(x)\exp(-i\omega x)dx\right|^2 . \qquad (4.1)$$

The study of the phase power spectrum (PPS) is crucial in the field of LIDAR technology [68] because the spectrum enables one to obtain data about the frequency information present in a retro-reflected beam. While applications of LIDAR technology such as range finding, chemical composition and Doppler LIDARs [53, 54] make use of scattering and red shifting, any application to vibrometry requires an understanding of the frequency spectrum.

Given these practical usages, an understanding of $S_\theta(\omega)$ in various turbulence regimes and under several turbulence models is desirable. The spectral form of $S_\theta(\omega)$ relies heavily on the statistical properties of the atmosphere. In the case of a Kolmogorov turbulence a -8/3 power law behaviour is expected in the spectrum, this is in addition to any artefacts due to vibrations in the reflecting surface.

Analytical work and numerical simulations are presented in this chapter which investigate an idealised case; a 2 dimensional propagation problem using simple 1 dimensional corrugated phase screens. The objective is to test computer simulation against simple theory and thus form a benchmark for more complex problems

undertaken in the next chapter. A simple Rytov (i.e. small perturbations in the phase introduced at the start of the propagation) propagation problem is considered; then, by the use of multiple 1 dimensional phase screens, an extended medium problem is investigated. The chapter ends with numerical simulations of $S_\theta(\omega)$ in strongly turbulent media in single screen and extended medium (i.e. multiple screens) cases, in these cases there are no theoretical results available.

4.1. PPS for propagation through a single, weak, corrugated phase screen.

One can derive a simple expression, in terms of both analysis and numerical computation, for the phase power spectrum $S_\theta(\omega)$ in terms of the equivalent spectrum for the phase screen $S_\phi(\omega)$; this is then compared with numerical simulation.

4.1.1 Analysis.

$S_\theta(\omega)$ is calculated for propagation through a single, weak phase screen in terms of the phase spectrum of the initial field. For a plane wave passing through a phase screen $\phi(r,t)$, the Huygens Fresnel integral gives the field *E(r, t)* at a distance *z* from the screen [31],

$$E(r,t)=\frac{ik}{2\pi z}\int_{-\infty}^{\infty}\exp\left(\frac{-ik|r-r'|^2}{2z}\right)\exp(i\phi(r',t))d^2r' \qquad (4.2)$$

where *k* is the wave number, *r* a spatial co-ordinate in 2 dimensions at the observation screen, *t* the temporal co-ordinate and r' the integral variable over the initial wave profile at the phase screen. Given a weak phase screen (i.e. $\phi < 1$), the approximation, $\exp(i\phi)\approx 1+i\phi$, holds. Equation (4.2) is reduced to

$$E(r,t)=1-\frac{k}{2\pi z}\int_{-\infty}^{\infty}\exp\left(\frac{-ik|r-r'|^2}{2z}\right)\phi(r',t)d^2r'. \qquad (4.3)$$

The phase perturbation θ of the scattered wave front will also be small, writing $\theta = \arg(E(r,z)) \approx \mathrm{Im}(E(r,z))$ gives

$$\theta(r,t) = -\mathrm{Im}\left[\frac{k}{2\pi z}\int_{-\infty}^{\infty}\exp\left(\frac{-ik|r-r'|^2}{2z}\right)\phi(r',t)d^2r'\right]$$

such that

$$\theta(r,t) = \frac{+k}{2\pi z}\int_{-\infty}^{\infty}\sin\left(\frac{k|r-r'|^2}{2z}\right)\phi(r',t)d^2r'. \tag{4.4}$$

The distance parameter *r* is written in terms of *x* and *y* co-ordinates such that *x* and *y* are defined on orthogonal axes. Consider now a 1 dimensional phase screen such that the field is translationally invariant, i.e. set *y* = 0 to give

$$|r-r'|^2 = x^2 + y^2 + x'^2 + y'^2 - 2xx' - 2yy' = y'^2 + (x-x')^2, \tag{4.5}$$

which can be used as an expansion in (4.4). This results in

$$\begin{aligned}\theta(x,t) = \frac{+k}{2\pi z}\int_{-\infty}^{\infty}\Bigg\{&\sin\left(\frac{k\left(x^2+x'^2-2xx'\right)}{2z}\right)\cos\left(\frac{ky'^2}{2z}\right)\mathrm{K}\\ &\mathrm{K}+\cos\left(\frac{k\left(x^2+x'^2-2xx'\right)}{2z}\right)\sin\left(\frac{ky'^2}{2z}\right)\Bigg\}\phi(x',t)dy'dx'\end{aligned} \tag{4.6}$$

from which one can integrate out the terms containing y', leaving

$$\theta(x,t) = \frac{1}{2}\sqrt{\frac{k}{z\pi}}\int_{-\infty}^{\infty}\left[\sin\left(\frac{k(x-x')^2}{2z}\right)+\cos\left(\frac{k(x-x')^2}{2z}\right)\right]\phi(x',t)dx'. \tag{4.7}$$

Given the screen moves at a speed *v* across the wave front, the phase screen $\phi(x',t)$ can be replaced by $\phi(x'+vt)$. This uses the Taylor 'frozen-in' turbulence hypothesis (see also section 3.3.1), meaning that the turbulence is assumed not to change during the wave propagation save for the motion due to wind. Performing the transformation $x'+vt \to x''$ yields

$$\theta(x,t)=\frac{1}{2}\sqrt{\frac{k}{z\pi}}\int_{-\infty}^{\infty}\left[\sin\left(\frac{k(x-x''+vt)^2}{2z}\right)+\cos\left(\frac{k(x-x''+vt)^2}{2z}\right)\right]\phi(x'')dx''. \qquad (4.8)$$

Now multiply the integrand in equation (4.8) by $e^{-i\omega_t t}$, integrate over *t* and take the square of the absolute value to give $S_\theta(\omega)$. The wave front develops over a single point at *x* = 0. There are two frequency space parameters ω_t and ω_x, such that $\omega_x=\omega_t/v$, arising from the temporal and a spatial variables. The phase power spectrum in 1 dimension is therefore

$$\begin{aligned}
S_\theta(\omega_t)&=\left|\int_{-\infty}^{\infty}\theta(x,t)\exp(-i\omega_t t)dt\right|^2\\
&=\frac{1}{4}\frac{k}{z\pi}\left|\int_{-\infty}^{\infty}\left[\sin\left(\frac{k(vt-x'')^2}{2z}\right)+\cos\left(\frac{k(vt-x'')^2}{2z}\right)\right]\times \mathrm{K}\right.\\
&\qquad\left.\mathrm{K}\,\phi(x'')\exp(-i\omega_x x''+i\omega_x x'')\exp(-i\omega_t t)dtdx''\right|^2\\
&=\frac{1}{4}\frac{k}{z\pi}\left|\int_{-\infty}^{\infty}\left[\sin\left(\frac{kv^2\left(t-x''/v\right)^2}{2z}\right)+\cos\left(\frac{kv^2\left(t-x''/v\right)^2}{2z}\right)\right]\times \mathrm{K}\right.\\
&\qquad\left.\mathrm{K}\,\phi(x'')\exp(-i\omega_x x'')\exp\left(-i\omega_t\left(t-x''/v\right)\right)dtdx''\right|^2\\
&=\frac{1}{4v^2}\left|2\int_{-\infty}^{\infty}\phi(x'')\exp(-i\omega_x x'')\left[\cos\left(\frac{z\omega_t^{\,2}}{2kv^2}\right)-\sin\left(\frac{z\omega_t^{\,2}}{2kv^2}\right)\right]dx''+\mathrm{K}\right.\\
&\qquad\left.\mathrm{K}+2\int_{-\infty}^{\infty}\phi(x'')\exp(-i\omega_x x'')\left[\cos\left(\frac{z\omega_t^{\,2}}{2kv^2}\right)+\sin\left(\frac{z\omega_t^{\,2}}{2kv^2}\right)\right]dx''\right|^2\\
&=\frac{1}{v^2}\cos^2\left(\frac{z\omega_t^{\,2}}{2kv^2}\right)\left|\int_{-\infty}^{\infty}\phi(x'')\exp(-i\omega_x x'')dx''\right|^2\\
&=\frac{1}{v^2}\cos^2\left(\frac{z\omega_t^{\,2}}{2kv^2}\right)\left|\hat{\phi}(\omega_x)\right|^2
\end{aligned}$$

resulting in

$$S_\theta(\omega_t) = \frac{S_\phi(\omega_x)}{2v^2}\left(1+\cos\left(\frac{z\omega_t^{\,2}}{kv^2}\right)\right) = \frac{S_\phi(\omega_t)}{2}\left(1+\cos\left(\frac{z\omega_t^{\,2}}{kv^2}\right)\right) \tag{4.9}$$

where $S_\phi(\omega)$ is the phase power spectrum of the phase screen. The spatial power spectrum of the phase screen itself has been related to the temporal spectrum of the propagated field. The result indicates that the spectrum for the propagated wave, $S_\phi(\omega)$, is merely the spectrum for the screen, $S_\phi(\omega)$, with a multiplicative oscillatory behaviour dependant on the propagation distance and wave number of the beam. For low frequencies, i.e. small ω_t, $S_\theta(\omega_t)$ tends to $S_\phi(\omega_t)$, while the oscillatory behaviour therefore increases for $k\omega_t^2 >> z$.

4.1.2. Computer Simulation.

The following numerical simulations look at the model investigated in section 4.1.1, using 1 dimensional phase screens under weak turbulences conditions. The theory of 4.1.1. is strongly dependent on the specific statistics of the phase screens as the resulting expression $S_\theta(\omega_t)$ is in terms of $S_\phi(\omega)$, the theory should be valid for any spectral model of atmospheric turbulence. The Von Karman correlation model of the form (see figure 1 below)

$$\Phi(\kappa_x) = 0.348k^2C_n^2L\frac{\exp\left(\frac{-\kappa_x^2}{\kappa_I^2}\right)}{\left(\kappa_x^2+\kappa_o^2\right)^{4/3}} \tag{4.10}$$

is used in these simulations. This model has low and high frequency filters built into it based on the inner $(\kappa_I = 2\pi/l_0)$ and outer $(\kappa_O = 2\pi/L_0)$ scales (see section 2.2.2 for a detailed overview of the Kolmogorov theory of turbulence). A -8/3 power law behaviour is expected in the inertial subrange $(\kappa_O < \kappa < \kappa_I)$ of the spectrum. The

sizes of the scales used in these simulations are l_0 = 50cm and L_0 = 0.2cm. An averaging over 100 realisations is used in order to improve statistics.

In each simulation, the total length of the phase screen used is 1m, sampled by 2^{13} points. The wind speed v = 2ms^{-1}, meaning that the total temporal length of the simulation, T, is half a second. Therefore the smallest frequency measurable by the simulation is $1/T = 2$Hz, while the largest measurable frequency is $2^{13}/2T$ = 8192Hz. For each simulation (i.e. for each set of parameters modelled) $S_\theta(\omega_t)$, $S_\phi(\omega)$ and equation (2.9) are plotted. The frequency parameters, ω, given in the spectral plots (figures 4.1 to 4.9) are all in Hz.

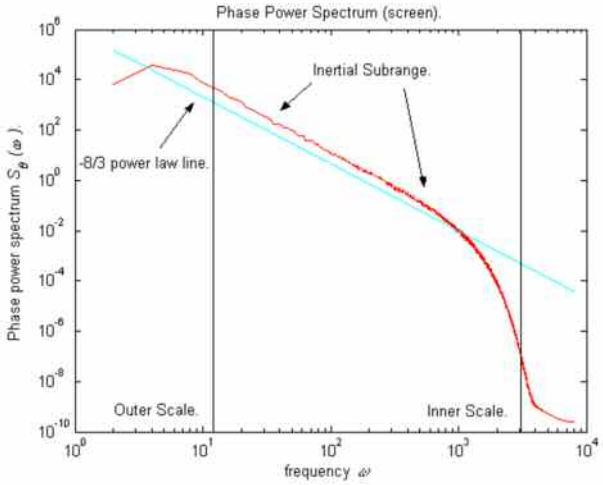

Figure 4.1, showing the inertial subrange, the inner and the outer scales in the spectrum. The inertial subrange was approximately two decades in length. Arbitrary units on the vertical axis.

In addition to these considerations, a 100Hz sinusoidal signal has been included in the wave before propagation in order that one might see how this signal appears in the spectral output. The strength of this signal is of the same order as the noise introduced by the phase screens. The ability to recover such signals (albeit with much more complicated frequency components) is the ultimate aim of the LIDAR technology that uses temporal frequency spectra like this.

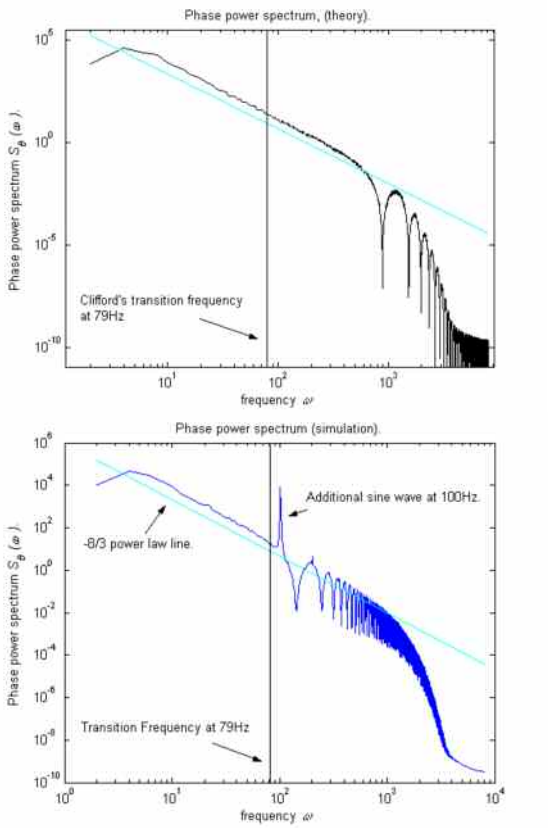

Figs 4.2 and 4.3; refractive index structure constant $C_n^2 = 10^{-16}\text{m}^{-2/3}$, wavelength λ = 1μm, propagation distance L = 100m, mean square phase shift $\langle\phi_0^2\rangle \approx 0.001$.

The most important feature in figures 4.2 and 4.3 is the existence of two regions, one at low frequencies where the spectrum of the propagated wave is equivalent to the screen spectrum (figure 4.1), and a second at high frequencies where an oscillatory behaviour can be seen in the spectrum. Note also that the spectrum follows a -8/3 power law in the inertial subrange as expected. The 'transition frequency' between these two regimes arises from a calculation performed by Clifford in [30], see section 4.2.1, in which two distinct regions, separated by a frequency ω such that $\Omega = \frac{\omega}{v}\sqrt{2\pi\lambda L} \approx 1$, are defined where $S_\theta(\omega)$ behaves quantitatively differently. This transition frequency provides a very accurate prediction of the distinction between the two regimes in the numerical output. The theory (equation (2.9)) is much less accurate, indicating that the oscillatory behaviour should begin at almost 1000Hz rather than 70Hz.

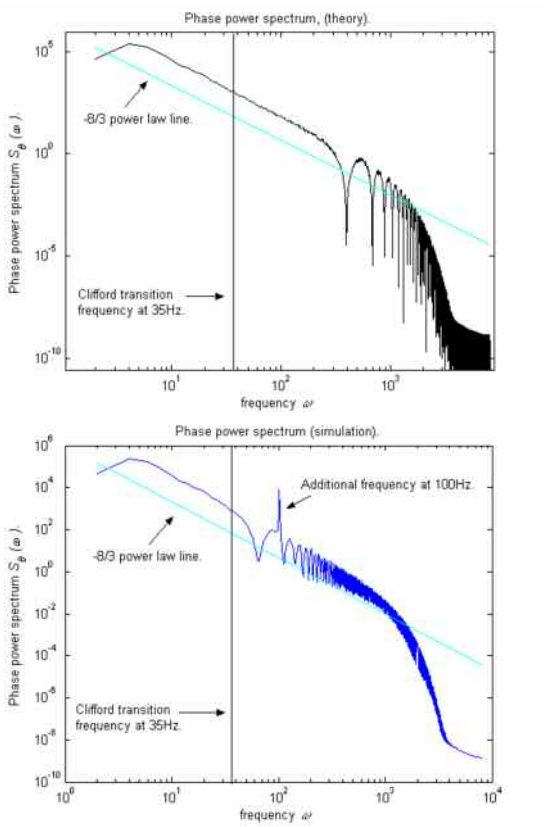

Figures 4.4 and 4.5; $C_n^2 = 10^{-16}\text{m}^{-2/3}$, $\lambda = 1\mu\text{m}$, $L = 500\text{m}$, $\langle\phi_0^2\rangle \approx 0.01$.

In figure 4.5 Clifford's transition frequency is successful in predicting the behaviour of the spectrum, again the theory developed in 4.1.1 (figure 4.4) is much less accurate.

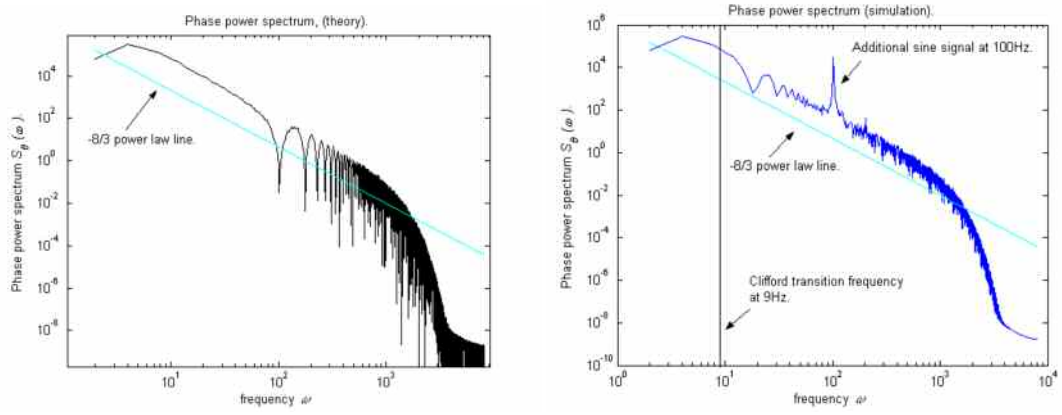

Figs 4.6 and 4.7; $C_n^2 = 10^{-17}\text{m}^{-2/3}$, $\lambda = 1\mu\text{m}$, $L = 7500\text{m}$, $\langle\phi_0^2\rangle \approx 0.01$.

In figures 4.6 and 4.7 the transition frequency is at 9Hz. The oscillatory behaviour is only just visible in figure 4.7; in comparison to figures 4.3 and 4.5 the behaviour is not as pronounced. Once again the theoretical prediction (figure 6) incorrectly predicts the transition frequency. Figures 4.8 and 4.9 look at a propagation geometry

using a much shorter wavelength and weaker turbulence. Once again the Clifford transition frequency provides an accurate prediction for the change in the behaviour of the spectrum while the Rytov calculation has over estimated the transition frequency by an order of magnitude.

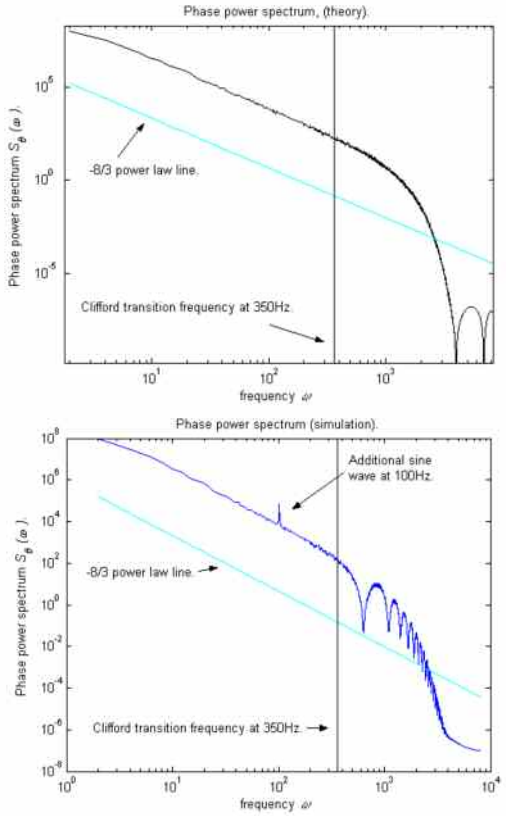

Figures 4.8 and 4.9; $C_n^2 = 10^{-18}\text{m}^{-2/3}$, $\lambda = 0.01\mu\text{m}$, $L = 500\text{m}$, $\langle\phi_0^2\rangle \approx 0.7$.

4.1.3. Conclusions.

In this section, computer simulation techniques have been used to model $S_\theta(\omega)$ for a corrugated, 1 dimensional, weak phase screen in the case of a plane wave. Simple Rytov theory qualitatively predicts the existence of oscillatory behaviour in the phase spectrum in the high frequency regime. This same theory fails in its prediction of the exact frequency at which the oscillatory behaviour begins to dominate, but a more rigorous derivation by Clifford (section 4.2.1) allows for the calculation of a 'transition frequency' which accurately predicts the same. Simple Rytov theory,

although correctly predicting the existence of an oscillatory regime for high frequencies, contains too many simplifications and assumptions to allow for an accurate prediction of the behaviour of the spectrum. $S_\theta(\omega)$ has a -8/3 power law form in the inertial subrange due to the Von Karman spectrum, as expected.

In these simulations the propagated field always remained in an 'unsaturated'[6] regime. Thus, although not specifically stated above, the statistics of the intensity were always approximated by the log-normal distribution (equation (2.28)). For stronger turbulence levels the propagated field will give negative exponential statistics for the intensity at similar propagation distances.

4.2. PPS for propagation through an extended medium; multiple, weak, corrugated phase screens.

Since the proposal of the phase screen technique [2] as a method for modelling scattering caused by a turbulent layer, much research has focussed on investigating its validity in approximating an extended region of a turbulent medium. Bramley [62] showed that the phase screen approximation works well for single scattering in the ionosphere. This work was extended when it was shown that the phase screen method is valid as an approximation for describing a medium that fluctuates along the entire path of the beam [63]. One can show (section 2.2.3), using a geometric optics formulation, that the phase shift on a propagated wave is proportional to the path integral over the refractive index fluctuations such that $\theta(x,y,L) = k\int_0^L n(x,y,z)dz$. Showing that one can impose the entire phase fluctuation θ at the start of the propagation path was an important validation for the phase screen technique .

Booker et al [61] tested this assertion using a numerical solution to the fourth moment equation for a propagated wave front. They used a forward difference method to solve the resulting non-linear PDE, claiming that small discrepancies in results between phase screen and extended medium formulations were insignificant, and that

[6] 'Unsaturated' is understood to mean that significant diffraction effects have not yet had time to develop.

the methods were essentially giving the same results. Nevertheless some differences are present, and it has been unclear until now how significant these will be for phase spectra calculations.

In their 1988 study of intensity statistics in an extended medium, Martin and Flatté modelled the extended medium using a sequence of 2D phase screens [15]. They chose to allow the beam to propagate between the screens, acquiring additional phase shifts at each one rather imposing the entire phase shift at the start of the propagation path. They imposed a set of conditions that maintained weak propagation between each screen, insisting that there were sufficient screens such that less than 10% of the total scintillation occurred between each screen. This idea was used again in a subsequent paper by the same authors [8], and extended by others [25] to use as a condition on the weak-fluctuation irradiance variance $\beta_0^2 = 1.23 C_n^2 k^{\frac{7}{6}} L^{\frac{11}{6}}$ (4.11). Belmonte [7] used 20 phase screens in modelling an extended medium. This, in similar fashion to the Flatté / Martin condition, appears to be a rather arbitrary decision, based more on an intuitive grasp of how an extended medium should behave rather than any rigorous derivation.

Modelling an extended medium by multiple phase screens has bridged the gap between the computational benefits of the phase screen method and the improved accuracy of the extended medium. One can generate n_s screens just as easily as a single screen; the propagation of the wave between each screen instead of across the entire path length in vacuum is a very easy modification to introduce into a code. The strength of the fluctuations imposed by each of these screens can be determined in two ways. Either each phase screen is given a phase shift[7] of $\phi_0 / \sqrt{n_s}$ in order to represent a total shift of ϕ_0, or one can use a Kolmogorov filter, for example (4.10), to filter the data in each screen with the total propagation length L replaced by the propagation length between each screen L/n_s .

[7] Note that the 'phase shift' imposed on a screen is understood to the mean $<\phi_0^2>$, defined by the second moment of the phase shift imposed upon the beam. It is convenient for the purposes of this thesis that $\phi_0 = \sqrt{\langle \phi_0^2 \rangle}$ is referred to as the 'strength' or 'depth' of the phase screen in question. This is used in the definition of the Gaussian correlation function (equation (2.9)) and can be inferred from the constants in the Von Karman spectrum (equation (2.25)).

4.2.1. An overview of Clifford's extended medium theory.

In his work of 1971 on the nature of phase power spectra for spherical waves propagating through extended media, Clifford [30] builds on the work of Tatarski [36] and Lawrence and Strohbehn [34]. Since his work, there has been only limited interest [73, 74 plus references in chapter 5] in phase and phase derivative power spectra in the open literature, although the intensity spectrum is the measure of choice for Martin, Flatte and Gerber [15, 25]. Clifford uses the Kolmogorov pure power law spectrum (equation (2.13)) and assumes weak turbulence. These conditions are compatible with simulations which employ the Von Karman modified spectrum. This theory is used to benchmark extended medium simulations.

Clifford calculates the power spectrum for the phase and the log amplitude of spherical and plane waves propagating through a weak scattering medium (i.e. such that $\left\langle \phi_0^2 \right\rangle < 1$). This is obtained via the correlation function $R_g(\tau)$, which is the Fourier transform of the power spectrum $S_g(\omega)$ for some function or stochastic process *g*. i.e.

$$S_g(\omega) = 4\int_0^\infty d\tau \cos(2\pi\omega\tau) R_g(\tau). \tag{4.12}$$

Lee and Harp [33] calculated the form of the correlation function for the phase θ for a weakly scattering geometry to be

$$R_\theta(\tau) = 2\pi^2 k^2 \int_0^L dz \int_0^\infty \kappa \Phi_n(\kappa) J_0(\tau v \kappa) \left\{ 1 + \cos\left(\frac{\kappa^2 z(L-z)}{kL} \right) \right\} d\kappa, \tag{4.13}$$

where $J_0(x)$ is a zero order Bessel function, κ the frequency space co-ordinate, *v* a characteristic velocity, $\Phi_n(\kappa)$ the spectrum of refractive index fluctuations, *L* the total propagation distance and *k* the wave number.

Writing down the phase power spectrum and integrating out the τ variable gives (in the case of a spherical wave)

$$S_\theta(\omega) = 8\pi^2 k^2 \int_0^L dz \int_0^\infty \kappa \Phi_n(\kappa) \left[(\kappa v)^2 - (2\pi\omega)^2 \right]^{-\frac{1}{2}} \left\{ 1 + \cos\left(\frac{\kappa^2 z(L-z)}{kL} \right) \right\} d\kappa, \qquad (4.14)$$

which can be evaluated by assuming a pure power law Kolmogorov spectrum for the refractive index fluctuations (equation (2.13)). This results in the following expression for the phase power spectrum in terms of a normalised frequency variable Ω defined by $\Omega = \frac{\omega}{v}\sqrt{2\pi\lambda L}$:

$$S_\theta(\omega) = 2.19 k^{\frac{2}{3}} L^{\frac{7}{3}} v^{-1} C_n^2 \Omega^{-\frac{8}{3}} \operatorname{Re}\left\{ 1 + {}_2F_2\left(1, -\frac{5}{6}; \frac{3}{2}, -\frac{1}{3}; i\frac{\Omega^2}{4} \right) + \mathrm{K} \right.$$
$$\left. \mathrm{K} + \frac{4}{11}\Gamma\left(-\frac{4}{3} \right)\left(-i\frac{\Omega^2}{4} \right)^{\frac{4}{3}} {}_1F_1\left(\frac{1}{2}, \frac{17}{6}, i\frac{\Omega^2}{4} \right) \right\} \qquad (4.15)$$

where ${}_1F_1$ and ${}_2F_2$ are hypergeometric functions [32]; from this, high and low frequency behaviour can be determined. Clifford obtained asymptotic forms for the above expression for both plane and spherical wave in both a low frequency (which one can also show using a geometric optics formulation, see appendix A) and a high frequency region as follows;

$$\Omega << 1 \Rightarrow S_\theta(\omega) \approx 4.38 k^{\frac{2}{3}} L^{\frac{7}{3}} v^{-1} C_n^2 \Omega^{-\frac{8}{3}},$$

$$\Omega >> 1 \Rightarrow S_\theta(\omega) \approx 2.19 k^{\frac{2}{3}} L^{\frac{7}{3}} v^{-1} C_n^2 \Omega^{-\frac{8}{3}}.$$

These approximations indicate that the only difference in the spectrum between low and high frequency behaviours is a factor of ½, with a transition frequency, ω_c, occurring at $\Omega \sim 1$. Thus Clifford's calculation indicates the existence of quantitatively different behaviour in $S_\theta(\omega)$ for given regimes in the frequency domain. This prediction corresponds to the transition frequencies used in figures 4.2

to 4.9 in section 4.1.2. In the extended medium simulations this qualitative difference is expected to manifest in the form predicted by Clifford's calculation, in the simpler single screen simulations the transition manifests itself in the appearance of oscillatory behaviour.

Thus although the simple Rytov calculation failed to predict the frequency at which this transition takes place, the same calculation is correct in its prediction of the qualitative behaviour change of the temporal frequency spectrum[8] under those conditions. Clifford's more rigorous calculation is required to give greater accuracy in predicting the behaviour of the spectrum with regard to the transition between regimes.

4.2.2. Simulation of an extended medium with weak turbulence.

The simulation of an extended region of weak turbulence using multiple phase screens is directly analogous to Clifford's theory. To perform similar simulations to those in 4.1 with multiple screens, the single screen of depth ϕ_0 is replaced by n_s screens each with depth $\phi_0 / \sqrt{n_s}$; the m^{th} screen is located at a distance $L(m-1)/n_s$ from the first phase screen such that the total propagation distance is equal to L. The beam interacts with the first screen, is Fourier decomposed into its spectral components for propagation to the second screen, then converted back into real space components for interaction with that screen (as per the simulation technique described in section 2.3). The beam progresses through each of the n_s screens before the scattered field is reconstructed at the observation plane $z = L$.

Each phase screen is of the same strength and has identical correlation properties. The Von Karman spectrum,

$$\Phi(\kappa_x) = 0.348 k^2 C_n^2 \frac{L}{n_s} \frac{\exp\left(\frac{-\kappa_x^2}{\kappa_l^2}\right)}{\left(\kappa_x^2 + \kappa_o^2\right)^{4/3}} \tag{4.16}$$

[8] The terms 'Phase power spectrum' and 'Temporal frequency spectrum' are virtually interchangeable in the study of temporal phase statistics.

is used as the spectrum of phase fluctuations. This spectrum has a major advantage over the pure power law in that it is much easier to sample numerically [20] due to the frequency cut-offs which remove a divergence at $\kappa = 0$. Alternative sampling techniques that will allow the modelling of a pure power law are discussed in the next chapter. The individual screens must remain statistically independent; to this end the screens are never physically closer than one correlation length. In this case the screens must be no closer together than the outer scale; $L_0 = 2\pi/\kappa_0$.

The Flatté / Gerber limit for the number of screens in an extended medium simulation can be used to ensure that enough screens are used. The number of screens used in an extended medium simulation, n_s, should satisfy $n_s > \left(10\beta_0^2\right)^{6/11}$, where $\beta_0{}^2$ (equation (4.11)) is the weak-fluctuation irradiance variance in the case of a zero inner scale [25]. Although these simulations include an inner scale, this limit provides a useful indicator for the number of screens to use.

4.2.3. Results of simulations.

Section 4.1.2 looked at a number of simulation regimes for a single weak phase screen. Extended medium simulations are now performed for a similar set of parameters. These simulations make use of 20 independent phase screens (well within the Flatté / Gerber [25] limit), each with Von Karman (4.16) filtered phase data as discussed above. The ratio between $S_\theta(\omega)$ (at the observation plane) and $S_\phi(\omega)$ (at the screen) is considered; this helps reveal detailed structure in the statistics. This ratio is expected to be unity in the low frequency regime, becoming ½ in a high frequency region separated by the now-familiar transition frequency at $\Omega \sim 1$. 100 realisations were used in each plot in order to smooth the statistics.

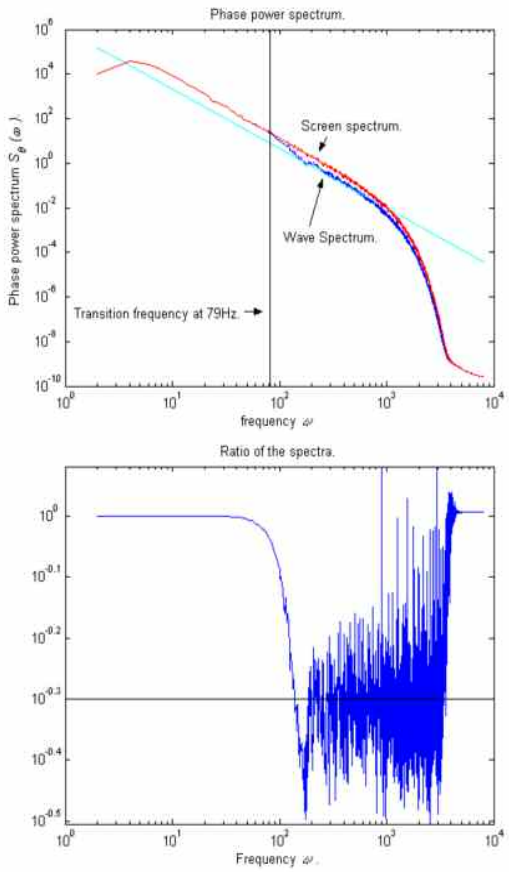

Figures 4.10 and 4.11: $C_n^2 = 10^{-16}\text{m}^{-2/3}$, $\lambda = 1\mu\text{m}$, $L = 100\text{m}$, $\langle\phi_0^2\rangle \approx 0.001$.

Figure 4.10 shows the two power spectra on the same plot, the spectra are indistinguishable at frequencies lower than ω_c while for $\omega > \omega_c$ there is a clear separation. Figure 4.11 gives the ratio between the spectra. The ratio oscillates noisily around ½ (the horizontal line in the plot) before returning to 1 after reaching the high frequency cut-off defined by the inner scale. Note that the frequency domain contained outside of inner scale is outside of the regime considered by Clifford's calculation and so cannot be expected to follow the law.

This second set of simulations (figures 4.12 and 4.13 below) use the same parameters as are used figures 4.4 and 4.5, the transition frequency ω_c signals a change to the behaviour predicted by Clifford's theory rather than the oscillatory behaviour seen for a single screen. There is a lot of 'noise' in these calculated ratios (figures 4.11, 4.13, 4.15 and 4.17), this can be accounted for by the fact that very small numbers are used in the ratios and that propagations problems using weak turbulence often fail to converge to a limit.

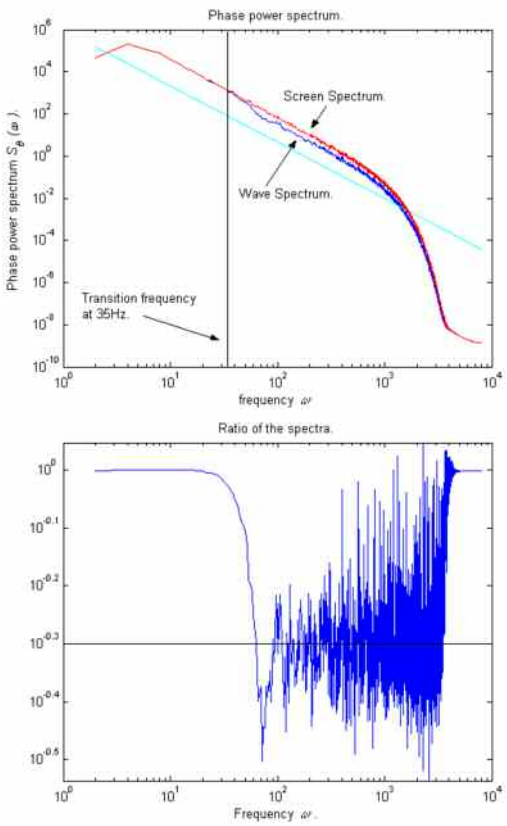

Figures 4.12 and 4.13: $C_n^2 = 10^{-16}\text{m}^{-2/3}$, $\lambda = 1\mu\text{m}$, $L = 500\text{m}$, $\langle\phi_0^2\rangle \approx 0.01$.

Figs 4.14 and 4.15 show two more results using different propagation parameters. Once again the transition frequency indicates a shift in the behaviour for the temporal phase spectrum, this simulation uses the same parameters as figs 4.6 and 4.7.

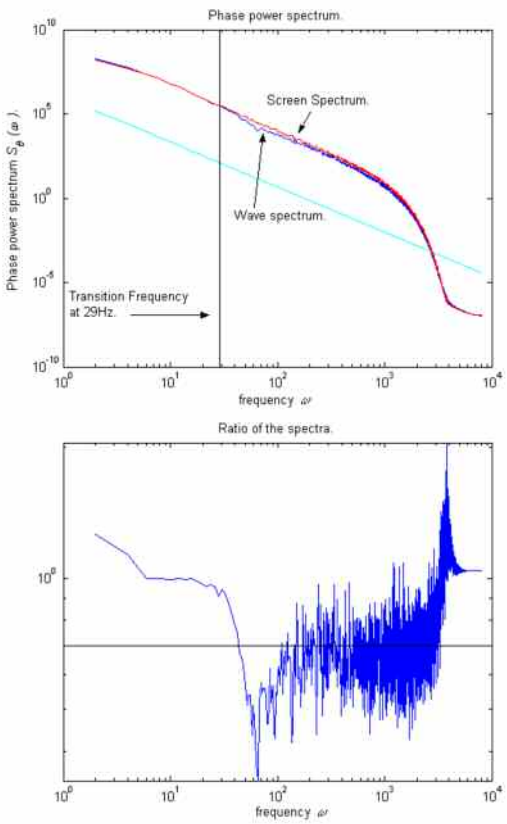

Figures 4.14 and 4.15: $C_n^2 = 10^{-17}\text{m}^{-2/3}$, $\lambda = 0.1\mu\text{m}$, $L = 7500\text{m}$, $\langle\phi_0^2\rangle \approx 0.01$.

Figures 4.16 and 4.17 (below), using the same parameters as in figures 4.8 and 4.9, show the transition frequency again predicting the quantitative change in the phase power spectrum. In the inertial subrange the ratio of $S_\theta(\omega)$ at the observation screen to $S_\phi(\omega)$ is approximately ½, for frequencies beyond the transition frequency ω_c. Above the high-frequency cut-off the theory breaks down. This is not a concern as Clifford's theory is valid in the case of a pure power law Kolmogorov spectrum, or in the inertial subrange.

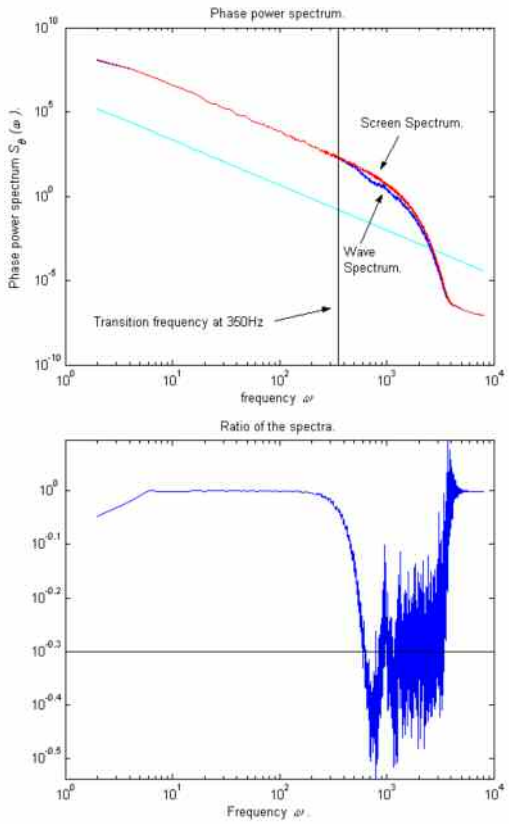

Figures 4.16 and 4.17: $C_n^2 = 10^{-18}\text{m}^{-2/3}$, $\lambda = 0.01\mu\text{m}$, $L = 500\text{m}$, $\langle\phi_0^2\rangle \approx 0.7$.

4.2.4. Conclusions.

This section has looked at the behaviour of the phase power spectrum in a two-dimensional propagation problem for weak turbulence ($\langle\phi_0^2\rangle < 1$). Important similarities and differences have been noted in both quantitative and qualitative terms between single screen and extended medium simulation. There exists a transition frequency, in agreement with Clifford's theory (at $\Omega \sim 1$), in the phase power spectrum plot below which the spectrum in the far field is indistinguishable from that at short propagation paths and above which a certain structure exists. This transition exists in both the single screen and extended medium cases. It is conjectured that the structure observed in the case of a single screen is somewhat 'washed out' in the case of multiple phase screens.

The use of a single screen introduces a seemingly artificial oscillatory structure into $S_\theta(\omega)$ that may not be present in experimental data. One can conclude (in contrast to the Booker et al study of 1985 [61]) that, in the study of temporal frequency spectra,

results arising from the use of the single screen and extended medium simulation methods differ significantly. Therefore any numerical modelling should be performed using an extended medium in order to ensure accurate qualitative behaviour in the resulting spectrum.

4.3. Propagation problems using stronger turbulence levels in 2D.

Theory pertaining to the statistics of coherent radiation in strong turbulence (i.e. $\left\langle \phi_0^2 \right\rangle >> 1$) is not as widely developed as for weak turbulence. Several different theoretical distributions for the intensity, notably short (log normal) and far (negative exponential) propagation distances, have been proposed The search for a model for the intensity that is valid across the focussing and saturation regimes is discussed in various papers. Phillips and Andrews [59] developed a model based on a field perturbed by 'specular' and 'diffuse' components that obey a distribution behaving like a negative exponential or a log-normal in different regimes. Churnside and Hill [58] used a similar approach while Jakeman and Pusey [60] developed a theory of 'K-distributions' based on the assumption that the field is perturbed by a fluctuating sum of *N* independent scatterers where *N* is distributed by a binomial. Hill and Clifford [46] also proposed a theory of intensity saturation in strong turbulence. Numerical simulations [25] and experiment [55] have proved crucial in the investigation of such statistics. Simulations performed by Flatté and Gerber showed that the intensity spectrum of strong turbulence was qualitatively, but not quantitatively, accurate [25]. Although several groups have had partial successes in investigating intensity fluctuations, there is much less work on phase statistics and the phase power spectrum in strong turbulence. Some progress was made in the realm of phase statistics by Jakeman et al [16] in their study of the intensity-weighted phase derivative, *J*. They calculated the form of the normalised second moment of *J* under strongly turbulent conditions (indeed their result was used to benchmark phase screen simulations in section 2.5.3) and used numerical simulation similar to those presented here.

This section reports on numerical simulations that look at the phase power spectrum in strongly turbulent regimes. All simulations are restricted to 2 dimensions, thus one-dimensional phase screens are used. Propagation problems considered use 'intermediate' and 'strong' turbulence levels at similar propagation ranges to those used in the previous sections. Differences between the extended medium and the single phase screen method are contrasted. Once again the dimensionless q (section 2.5.1) parameter is used to characterise the propagation distance and other parameters in the simulation. This is done to control the propagation regime of the simulation while at the same time restricting the simulations to strong turbulence. Therefore one can define a mean square phase shift $<\phi_0^2>$ and a propagation regime[9] $-\ln(q)$ before adjusting the other parameters to ensure that these conditions are maintained.

4.3.1 PPS for propagation through a single, strongly turbulent, corrugated phase screen.

Simulations were performed using comparable parameters to those used in section 4.1.2. Two levels of 'strong' turbulence were used, firstly $\phi_0 = 10$ and then $\phi_0 = 100$. Very little structure was observed in $S_\theta(\omega)$ when the beam propagated to distances close to the screen. Thus, unlike in 4.1.2, the focussing and far field (Fraunhofer zone) regimes are probed. The propagation distances are described in terms of the parameter q (defined in section 2.5) so as to more easily relate the propagation problem to either the near, focussing or saturation regimes. A Von Karman spectrum is also used. All parameters are normalised to the step sizes used in the computer program, while the turbulence level is normalised to the mean square phase shift ϕ_0.

[9] See chapter 2 for a discussion of the relationship between q and the propagation regimes.

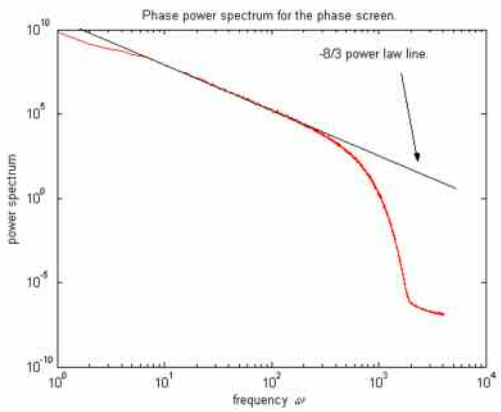

Figure 4.18, the phase power spectrum of a single, corrugated phase screen using ϕ_0 = 10. Note the -8/3 power law dependence in the inertial subrange and the high / low frequency cut-offs.

Figure 4.18 shows the phase power spectrum for a 'deep' phase screen. It is against this that one can compare the spectra of the propagated fields in a similar manner to previous sections. Although no theory exists it is still instructive to look at the structure of the spectrum, especially in the high frequency region. The phase power spectra are plotted alongside a histogram equivalent to the pdf of the intensities for each propagation. A log-normal curve (equation (2.28)) is plotted over the intensity pdf for comparison with theory, the curve is expected to be a good fit in the Fresnel and focussing zones with some divergence for far-field propagation.

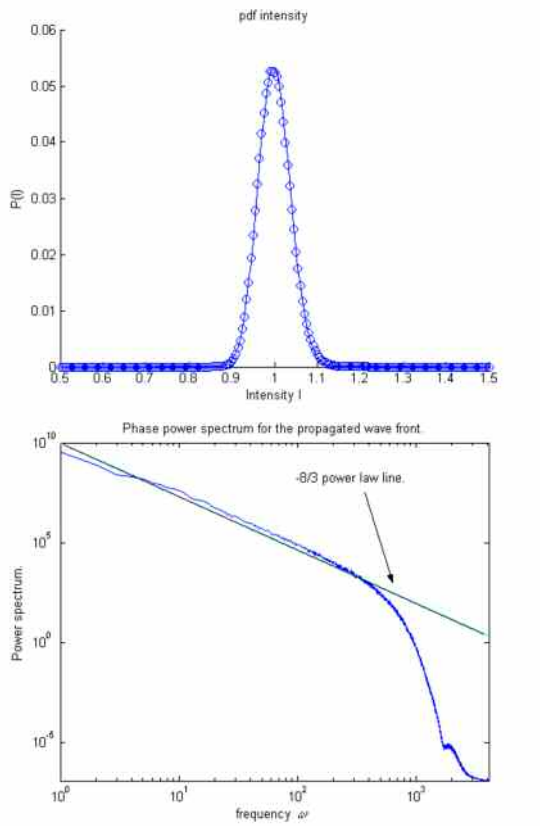

Figures 4.19 and 4.20, -ln(*q*) = -8, the Fresnel zone, no structure to be seen at high frequencies. Note that the initial beam was a plane wave of unit intensity.

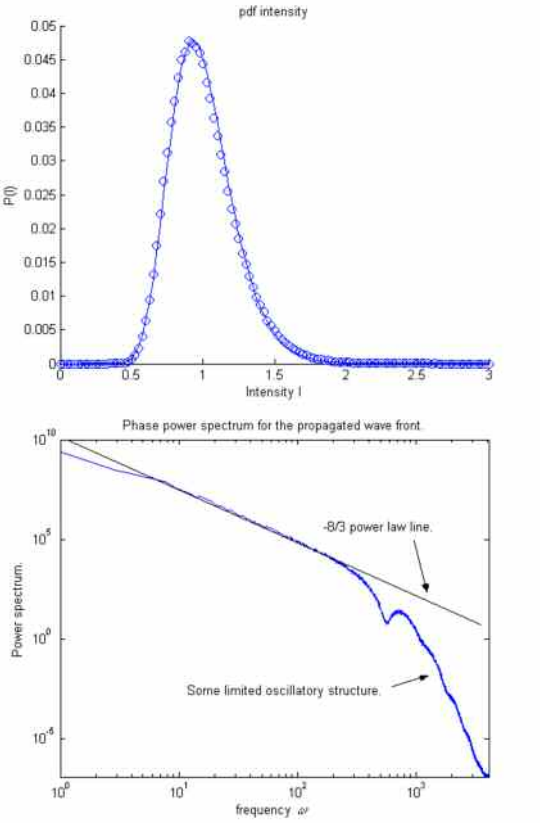

Figs 4.21 and 4.22, -ln*(q)* = -6, the Fresnel zone, some structure at high frequencies.

Figures 4.19 and 4.20 give results of propagations into a very short propagation distance; as can be seen from the pdf plot of the intensity. Figure 4.20 is almost identical to figure 4.18. Figures 4.21 and 4.22 show some structure that has hitherto not been observed. The log normal distribution fits the data in figure 4.21 while giving high frequency behaviour similar to the oscillatory pattern seen in the weak turbulence propagations in section 4.1.2. This pattern is not as well-developed.

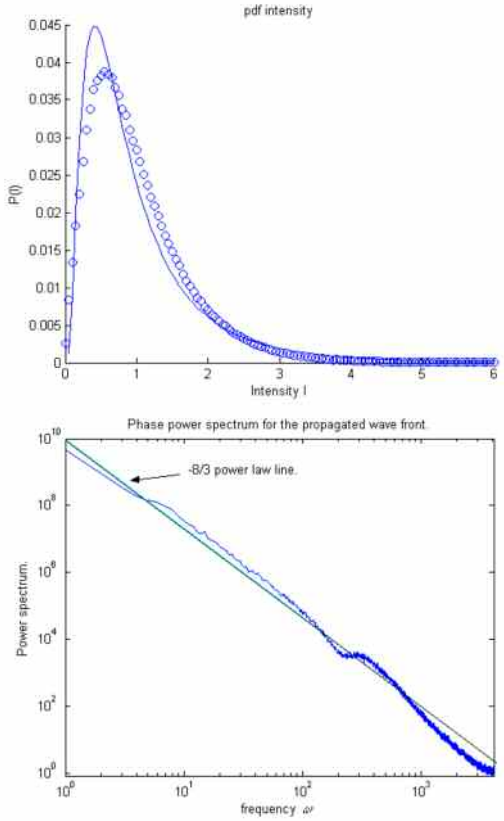

Figures 4.23 and 4.24, -ln*(q)* = -4, the focussing regime.

Figures 4.23 and 4.24 show the focussing regime, the log-normal model is no longer as accurate a model for the intensity statistics as in figures 4.19 and 4.21. There is a large change in the phase power spectrum in the high frequency region in figure 4.24. The existence of the high frequency cut-off, normally present due to the inner scale, has been swamped by the strength of the turbulence.

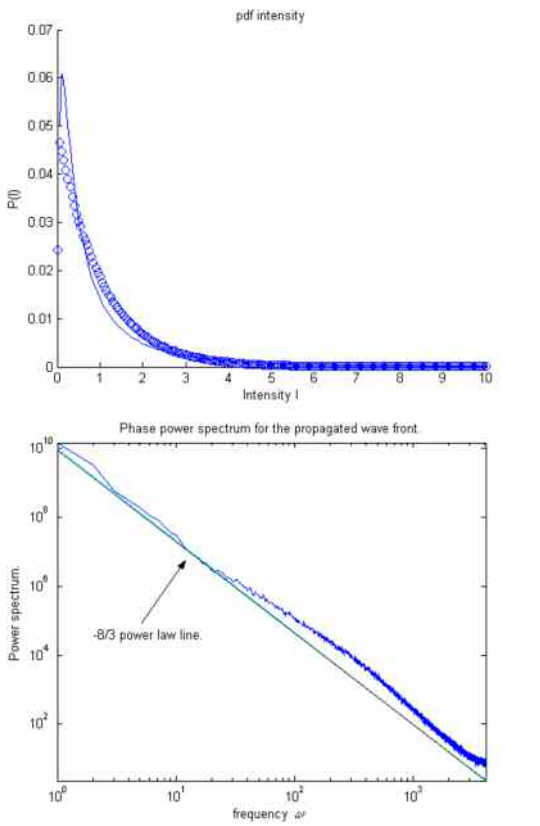

Figures 4.25 and 4.26, -ln*(q)* = -2, the Fraunhofer zone, spectrum maintains the -8/3 power law line over the full range of frequencies.

Figure 4.26 indicates that the -8/3 power law line, which is associated with the Kolmogorov theory of turbulence, is now dominating over the entire range of frequencies. Any oscillatory behaviour remaining in figure 4.24 has been totally eliminated. Figure 4.25 also confirms negative exponential statistics in the intensity, i.e. this propagation regime is giving a Gaussian saturation.

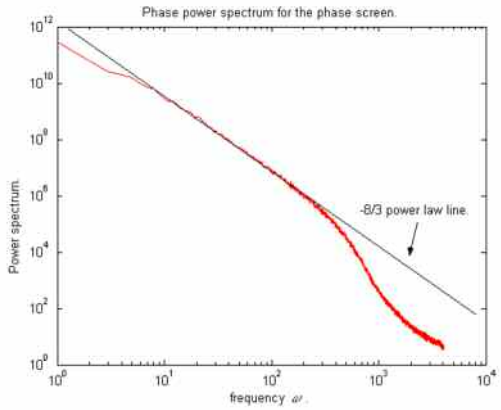

Fig. 4.27, the phase power spectrum of a single, corrugated phase screen using ϕ_0 = 100. Note the -8/3 power law dependence and the high / low frequency cut-offs.

Attention is now turned to simulations using stronger screens of ϕ_0 = 100. The spectrum for the such screens (see figure 4.27) is several orders of magnitude larger than the equivalent intermediate turbulence spectrum due to the higher level of turbulence. The high-frequency cut-off, despite still being visible, is not as pronounced as before (figure 4.18). Here the spectrum at high frequencies decreases by about 5 orders of magnitude with respect to the low frequencies, while for weaker turbulence the drop was closer to 10 orders of magnitude (see figure 4.1).

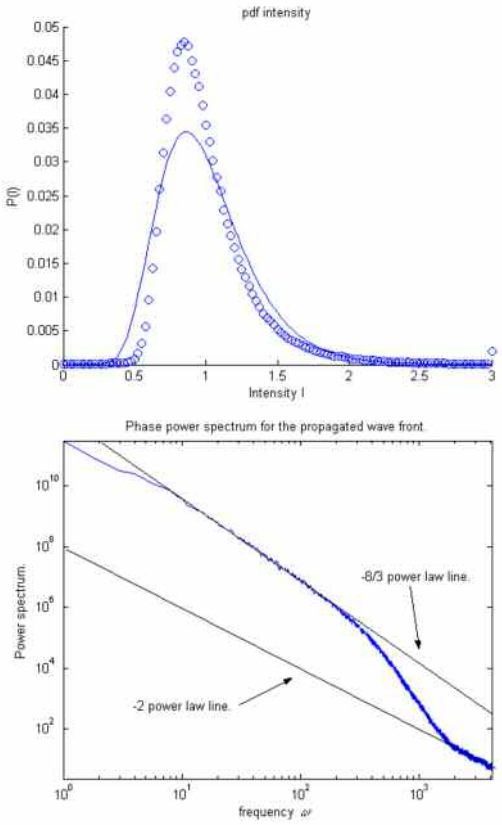

Figures 4.28 and 4.29, the spectrum in the Fresnel zone (*-ln(q)* = -6).

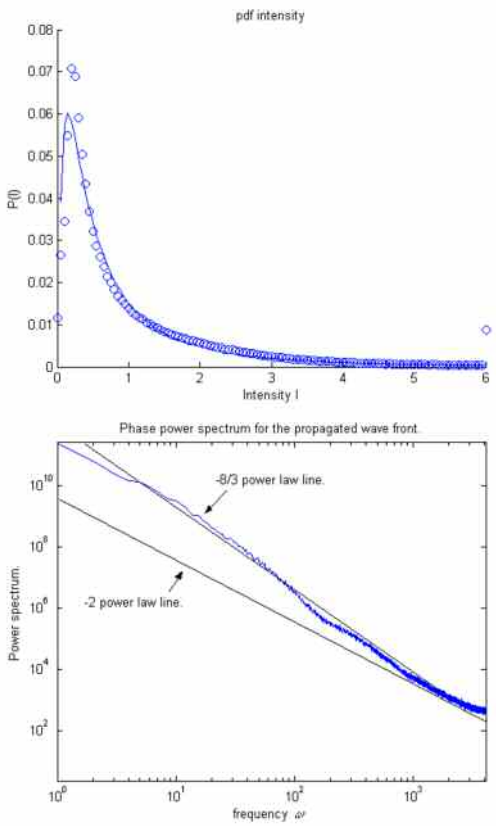

Figures 4.30 and 4.31, the spectrum in the focussing regime (*-ln(q)* = -4).

Figures 4.28 through to 4.31 show the phase power spectra in the Fresnel zone and the focussing regime. The spectrum in figure 4.29 is equivalent to that given in figure 4.27, inferring therefore that very little scintillation or diffraction effects have occurred in the beam. The log normal model for the pdf of the intensity is no longer a good fit now that a strongly turbulent regime is being considered, this has been noted by several other researchers [58, 59]. The most interesting artefact appears in figure 31, which contains a change from the usual -8/3 power law behaviour in the spectrum to an apparent -2 power law behaviour in the high frequency regime.

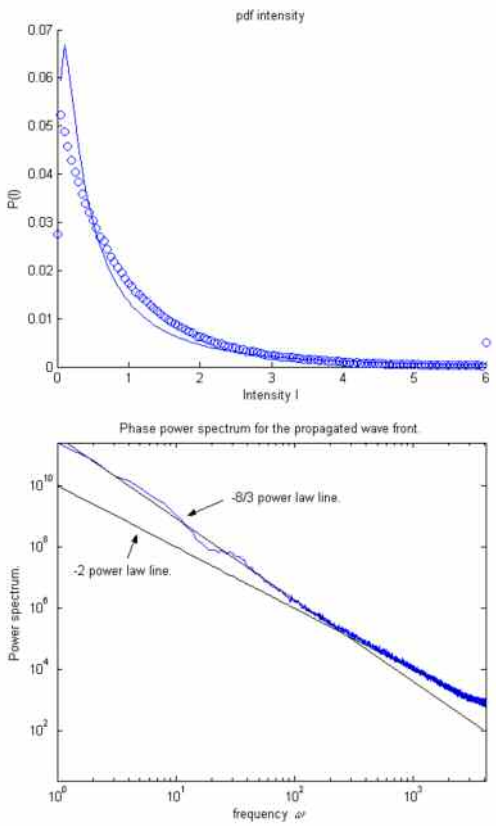

Figures 4.32 and 4.33, the spectrum in the Fraunhofer regime (*-ln(q)* = -2).

Figure 4.33 differs from figure 4.31 in that the transition from -8/3 to -2 power law occurs at a lower frequency. This is significant as the -2 power law regime extends into the inertial subrange of the spectrum, whereas in figure 4.31 it only appears outside the high frequency cut-off. Note the intensity statistics in figures 4.32 and 4.34 indicate a Gaussian saturation regime.

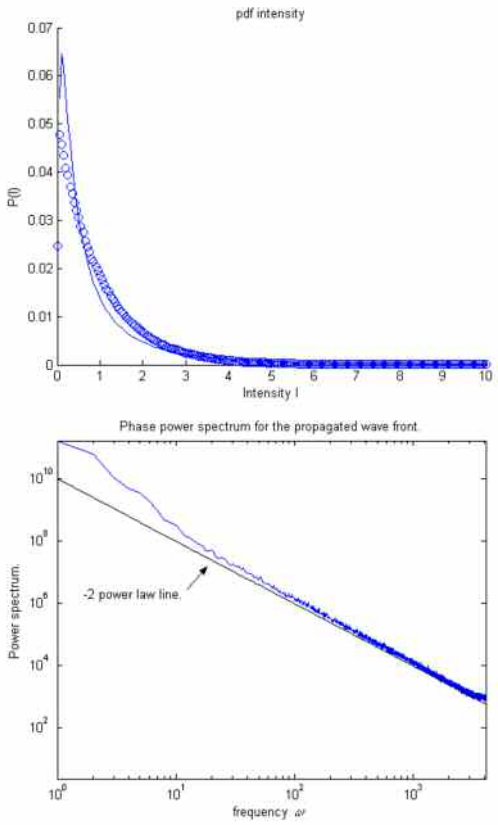

Figures 4.34 and 4.35, the spectrum in the Fraunhofer regime (*-ln(q)* = 0).

Figure 4.35 indicates even stronger evidence that the -2 power law feature is a significant artefact, here the entire spectrum is now dominated by this behaviour. It is postulated, based on the evidence presented here, that a coherent wave front which propagates into the far field and experiences strong turbulence will have a phase power spectrum which exhibits, at least in certain regimes, a -2 power law behaviour. It is further postulated that propagating a beam over longer distances will cause the -2 power law to be observed over a greater range of frequencies. This assertion will be revisited in more detail in chapter 5.

This behaviour could be the result of aliasing occurring in the simulation process (section 2.3). Although 'padding' space has been left for the beam to diffract into, it is possible that aliasing is occurring regardless. An approximation for the level of aliasing that one can expect in a 1 dimensional phase screen simulation is derived in [21], a Gaussian correlation function is used with correlation length ξ and depth ϕ_0. The minimum length of screen required to avoid aliasing effects (i.e. such that one element of the screen doesn't interact with itself by diffracting through the periodicity

of the Fourier transform) is $D(L)=\frac{\phi_0 L\sqrt{2}}{k\xi}$. Using a Von Karman filter function requires that this formula be multiplied by a factor of 4; this takes into account the fact that the rate of change of the phase across the screen is estimated to be 16 times as high (in an RMS sense) in a Von Karman screen as in a Gaussian one. Choosing the strongest propagation geometry used (i.e. figures 4.34 and 4.35), and approximating the correlation length ξ to the outer scale L_0, gives ϕ_0 = 100 and $L \approx 10^7$. This gives a minimum screen length of approximately 800 units[10]. Given that screens used are of size 2^{13} (i.e. 8192) points in length, one can conclude that no aliasing effects are being observed.

4.3.2. PPS for propagation through an extended medium, strong turbulence.

The use of extended media is important in retaining accurate qualitative behaviour in phase spectrum simulations. Differences have been seen in the use of a single and multiple screens. In section 4.3.1 a single strong screen was used, and oscillatory patterns in the high frequency range were found for ϕ_0 = 10. The extended medium is now considered for these strongly turbulent situations. This structure is expected to be 'washed out' in a similar way to the effects seen for weak turbulence.

The following simulations were performed in much the same way as those described in section 4.2.3. The way that one calculates the number of phase screens to be used is different. The weak-fluctuation irradiance variance no longer applies as it relies on a weak turbulence assumption, it is still possible, however, to satisfy Martin and Flatté's condition, $\sigma_I^2(\delta z) \le 1.1$, on the percentage of the total scintillation occurring between each screen. In section 4.3.1 it was shown that, in this strongly turbulent propagation problem, the far field begins at approximately $-\ln(q) \ge -1$. It is well-known that the scintillation index, σ_I^2, of the beam saturates at 2 in the Fraunhofer regime, and so to retain an inter-screen distance δz such that $\sigma_I^2(\delta z) \le 1.1$ one must

[10] Note that the 'units' here are the sampling lengths of the phase screen. This is because, unlike in the simulations discussed in section 4.2, the distances in these simulations are normalised to the sample length of the screen Δx rather than standard S.I. units.

use $-\ln(q) \approx -6$. Thus if the propagation range is restricted to no more than $-\ln(q) = -1$, the required condition is that $L/\delta_z = 150$. Thus maintaining 200 independent phase screens will satisfy the Martin / Flatté condition for all propagation problems of strong turbulence. Note that this will satisfy the separation condition on the screens if $200\xi < L$, where ξ is the correlation length of the phase screens.

The results shown in the figures below were achieved by performing simulations that used 200 independent phase screens with the total mean square phase shift ϕ_0 = 10.

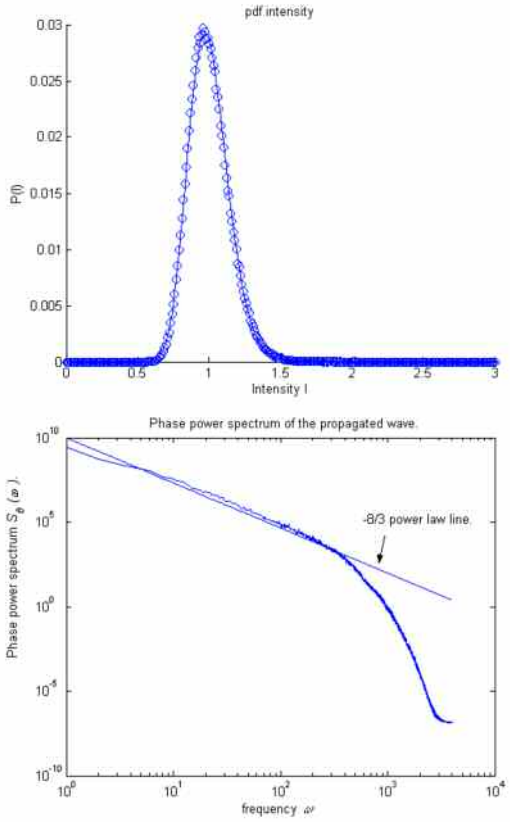

Figures 4.36 and 4.37, -ln(*q*) = -6, the Fresnel zone, note the contrast between figure 4.37 and figure 4.22.

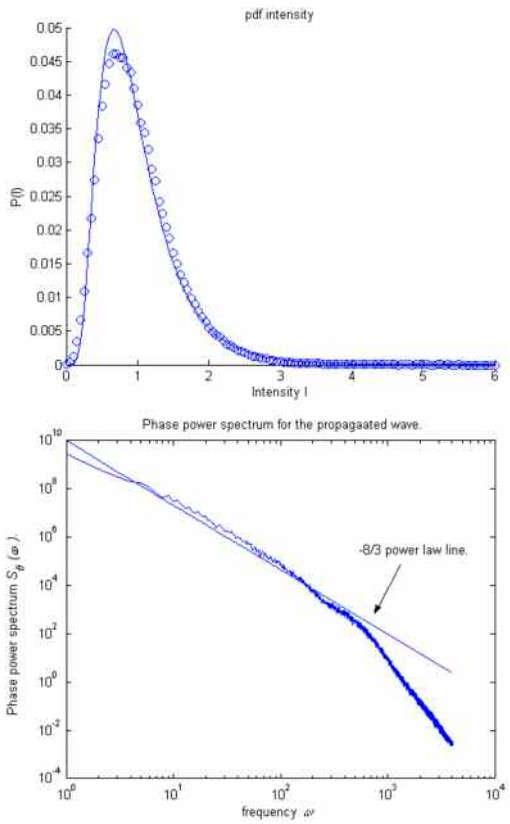

Figures 4.38 and 4.39, -ln(*q*) = -4, the focussing regime, note the contrast between Fig 4.39 and Fig 4.24 with regards to the high frequency oscillations.

The most important result here is a confirmation of the conclusions drawn in 4.2.4 in which the use of an extended medium was seen to eliminate unphysical oscillations in the spectrum in the high frequency regime. Figures 4.36 and 4.38 show that the intensity statistics are log normal while figures 4.37 and 4.39 show no evidence of oscillatory behaviour. The -2 power law behaviour remains an artefact in these extended medium simulations. Comparing figures 4.41 and 4.43 (below) to figures 4.31 and 4.33 respectively shows very similar behaviour, the -2 power law behaviour is begins to dominate over the range of frequency values as the propagation distance increases.

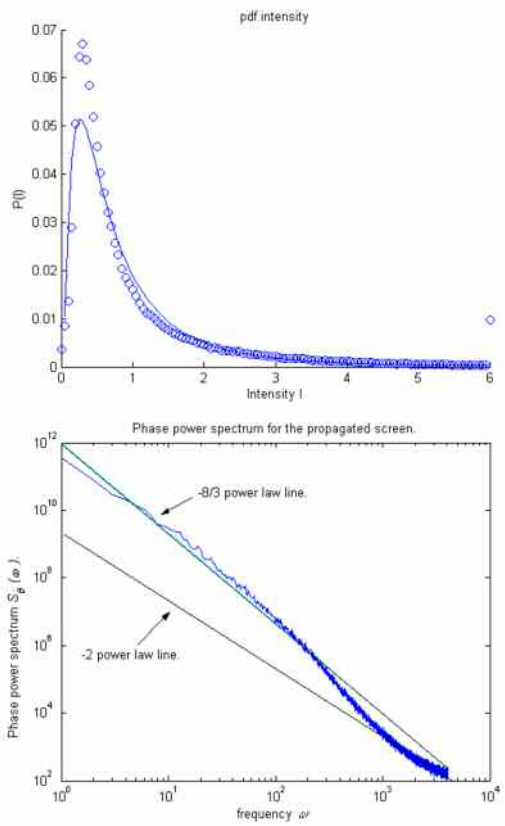

Figures 4.40 and 4.41; -ln*(q)* = -2, the focussing regime. -2 power law line behaviour is present in the high frequency region.

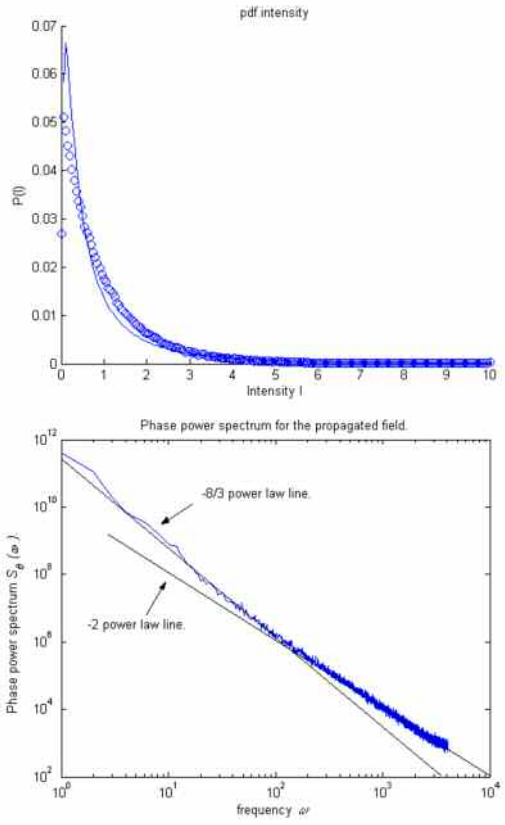

Figures 4.42 and 4.43, -ln*(q)* = 0, the Fraunhofer zone. -2 power law dominates. Fig 4.42 shows a Gaussian saturation regime.

Multiple and single phase screen simulations differ significantly in temporal spectra produced. It should also be possible to see this in 3D models, while the power law behaviours found should be observable in experimental data.

4.4. Conclusions.

This chapter has introduced and investigated a very important area in remote detection and LIDAR systems, namely the study of $S_\theta(\omega)$. Simulations were restricted to plane wave propagations in two-dimensions using one-dimension phase screens.

Simple weak turbulence models were considered first, some theoretical results exist in this case. Numerical simulations were used to compare the phase power spectrum in the scattered far field with that of the screen, qualitative evidence was found to back up the validity of the simulation technique. Extended medium simulations were also performed using multiple phase screens, equally-spaced, having equal mean square phase shift values and obeying the Martin / Flatté limit for inter-screen scintillation. These numerical experiments compared favourably with the work of Lee & Harp as well as Clifford. These calculations allow the inference that a single screen may introduce unphysical artefacts into the high-frequency regime of the spectrum.

The modelling of the phase power spectrum for strong and intermediatly turbulent layers was considered. No theoretical results exist that are applicable to such problems; thus numerical modelling must be used. The phase power spectrum for a strongly turbulent propagation in the Fresnel zone behaves in much the same way as a weakly turbulent case, in that the spectrum of the propagated field is almost equivalent to that of the screen. Indeed it is through this property that experimentalists study the structure of the spectral components of atmospheric turbulence as shall be seen in the following chapter. The basic -8/3 power law observed is a direct result of the Kolmogorov turbulence model used in filtering the phase screens. The high and low frequency cut-offs are arbitrary, the relationship

between the real atmosphere and the phase spectrum will be dealt with in the next chapter.

There are several important conclusions to be drawn from these two-dimensional simulations using strong turbulence. The first is that the magnitude of the spectrum is much larger when strong turbulent is present; this is perhaps to be expected, but is a good indicator as to the level of turbulence present in the atmosphere. Clearly it is harder to measure a weak signal under strong turbulence conditions. The second is seen in the way the spectrum changes to have a -2 power law at high frequencies. This artefact was visible to different degrees for all simulations apart from those at short propagation ranges. The -2 power law begins to dominate the spectrum at lower frequencies as the propagation range increases, this is a similar pattern to the transition frequencies noted in Clifford's theory in section 4.2.2. Aliasing, as a cause of this effect, has been ruled out. The significance of the shift in power law behaviour is currently unknown.

5: 3D simulation techniques and applications to LIDAR.

The applications of coherent radiation systems are varied and widespread, ever since the first ruby lasers were developed there have been many proposed uses for such systems [6, 53]. A general LIDAR system consists of a set of output optics, containing a lens and filters, and at least one receiving device such as a photo-detection unit. The best laser for use in a system designed to operate in the atmosphere needs to take into account several factors; safety, bandwidth, wavelength and power levels being examples. The development of lasers has allowed the development of remote detection systems that have similar characteristics to radar systems, using very short and powerful pulses[11] that allow for such applications as ranging and absorption detection. It is essential that a LIDAR uses a laser with a narrow bandwidth and with acceptable levels of power and beam spread in order to maintain safety in the surrounding environment. A LIDAR system uses a small amount of its output power to create a frequency-shifted beat signal with which the received radiation can be compared. Upon the photo-detection of a returned signal, the local oscillator is mixed with the frequency of the received field. This heterodyne technique allows the frequency spectrum of the received field to be detected. The receiver optics in a LIDAR system can be situated in a different (bi-static) location or share an aperture with the transmission optics (mono-static). Due to the necessity of using of a local beat signal to detect frequency information, the mono-static system is most commonly used. The receiving optics in a mono-static system are on the axis of the propagated beam, consequently one expects to see noise due to back-scattering from the medium immediately in front of the apparatus. A bi-axial system (which uses a receiving plane away from the transmission optics) can be used to correct this.

Different applications of LIDAR systems use different scattering effects in the atmosphere. Resonance scattering (absorption and emission of laser radiation) is used in the detection of trace elements in the upper atmosphere. Raman scattering (where the emission of laser energy is accompanied by a corresponding change in frequency) has an extremely small scattering cross section and can be used in absorption / detection systems when the density of atmospheric aerosols is likely to be high.

[11] Although LIDAR systems often use continuous detection.

The use of lasers in LIDAR systems is crucially different their use in differential absorption (DIAL) systems in that all atmospheric events effect the system as noise, frequency shifts, that might be imparted on the beam by the target or sensing equipment, are of interest. The greatest source of noise present in any LIDAR system is scattered solar radiation. Using a narrow bandwidth and adjusting the receiving optics such that they detect only a very narrow band around the laser wavelength, the LIDAR system eliminates this source of noise. The sources of noise modelled by the phase screen are those which have the most profound impact on the laser propagation; refractive index fluctuations, air currents, thermal flows and temperature gradients are all included in the Kolmogorov theory of turbulence. The familiar $-11/3$ power law in the three-dimensional spectrum of such fluctuations applies to each of these noise sources (see section 2.2.2).

The simulation of laser beam propagation using numerical techniques is intrinsically linked to experimentation with real systems in the physical world. It is therefore important to link these simulations to LIDAR systems. In this chapter the use of three-dimensional simulations is introduced to 'experiment numerically' with the LIDAR system. Physical values are used in these simulations while the use of dimensionless parameters is completely abandoned. Gaussian profile beams will be used in addition to plane waves; beam-spreading and wander phenomena will be considered. These numerical studies also allow an investigation of the long-standing problem of finding an accurate turbulence model to represent the real atmosphere by comparing and contrasting the models to experimental data. Experiments results, performed using LIDAR equipment, are presented at the end of the chapter and compared with numerical simulation.

5.1. Contrasting simulation techniques in two and three dimensions.

Three-dimensional simulations are carried out in the same way as those in two dimensions (section 2.4). Here, a three-dimensional grid of Gaussian random numbers is defined and filtered using the Wiener-Khintchine technique as discussed previously. The main differences are in the use of screens containing many more points ($2^7 \times 2^7$ in the sample plots that follow in section 5.2) and a requirement of a

much more subtle interpretation of the 'moving' screen. One cannot simply equate the spatial and temporal co-ordinates in the 3-dimensional case as has been done previously. This is because it is possible to move the screens in more than one direction. Therefore phase derivative statistics cannot be calculated by taking a simple difference in the phase across the wave-front in the far field.

Instead, the phase derivative is calculated by moving the phase screens within the simulation itself, i.e. transposing the matrices representing the phase screens at each time step. The beam is allowed to propagate at each time step before moving the screens (transposing the matrices) once more. After each transposition and propagation, i.e. at each time step, the data is recorded in the far field. In this way a data set is built up containing the temporal evolution of the beam in the far field. From this it is easy to find the required statistics such as intensity moments or temporal phase spectra. This technique lends itself to extended medium simulations, as each screen can be moved independently between each time step if needed. In the simulations that follow, all screens move in the same direction at a constant speed *v*. It would be a simple matter though, in a future study perhaps, to use a more complex model for the motion of the air by allowing the screens to move according to some distribution of velocities $v(x)$. Any number of screens can be used in this model, limited only by the memory available and the outer scale length of the turbulence.

Three-dimensional simulations naturally use more memory than two-dimensional ones. While the simulations performed in chapter 2 made use of 2^{14} points in a screen and produce accurate statistics, each screen used in section 5.2 is an array of size $2^7 \times 2^7$. This still amounts to 2^{14} data points in the simulation. Chapter 4 considered 3 decades of information (i.e. 2^{14} data points) in the temporal phase spectrum of a two-dimensional simulation. In three-dimensional simulations of size $2^7 \times 2^7$, using the same number of data points, only 2 decades of information (i.e. 2^7 data points) are available. To make use of three-dimensional simulations that would give 3 decades of information one would have to use $2^{14} \times 2^{14}$ (= 268 million !) points; a quantity of data which, given the number of fast Fourier transforms that need to be performed, would take an almost unfeasibly long time to process. Solutions to these practical problems in the simulation of phase spectra are discussed in section (5.4).

5.2. Three dimensional simulations, plane waves and extended media.

Now consider some simple 3-dimensional simulations that make use of plane waves and extended media modelled by multiple phase screens.

Figs 5.1 (below) indicate the changing intensity profile (lighter areas represent greater intensity in the beam, darker areas indicate that the intensity is approaching zero) for a plane wave propagated through 5 independent phase screens with a simple three-dimensional Gaussian correlation function

$$\rho_{\phi}(\underline{r}) = \phi_0^2 \exp\left(\frac{-|\underline{r}|^2}{\xi^2}\right). \qquad (5.1)$$

Each screen has an individual depth of $<\phi_0^2>$ = 1 and correlation length ξ = 10, giving a total root mean square phase shift for all 5 screens of $\sqrt{5}$. The first row image shows the intensity in a Fresnel zone close to the first phase screen, the middle row indicates the focussing regime and the bottom row shows the Gaussian saturation regime. The range of propagation increases from left to right in each row, with the top-left image giving the propagation closest to the first screen while the bottom-right image gives the propagation range furthest from the initial screen.

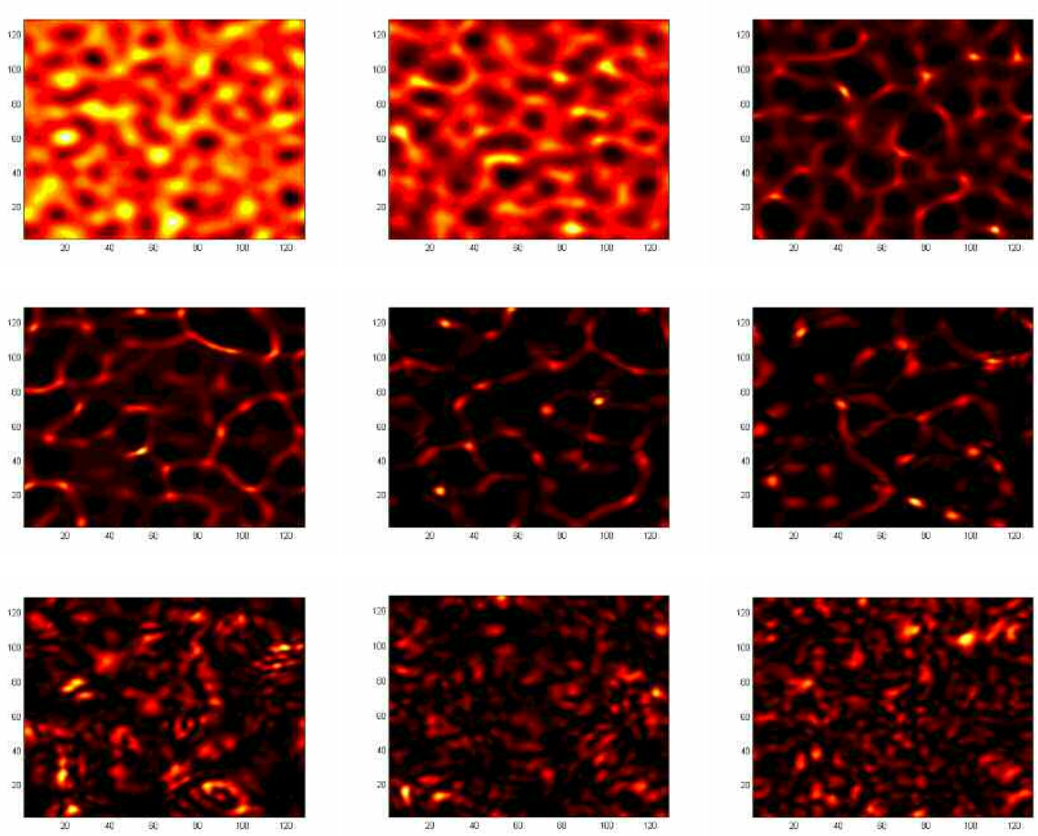

Figures 5.1, a sequence of images showing the resultant intensity of a three-dimensional propagation through an extended medium propagation at increasing distances.

Figs 5.2 show the pdfs of the intensity for the above regions, characteristics that were present in the simulations performed in section 2.6.1 are also visible here.

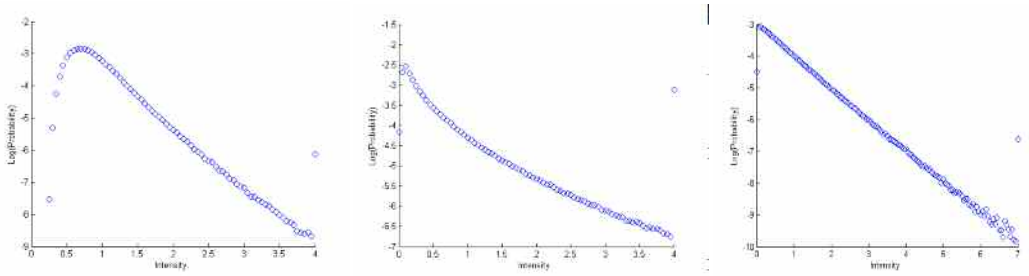

Figures 5.2, log-linear plots for the intensity pdf for the top-left, centre-middle and bottom-right images in figs 1 respectively.

One can clearly see the regimes of propagation in the figures above, the top left figure in figure 5.1 is in the Fresnel zone and as such shows very little departure from the intensity near the last screen. The central row of figures show the focussing regime, the features in the plot include bright ridges (caustics) which are reminiscent of the

patterns of light seen at the bottom of a pool of water. The Gaussian saturation regime (Fraunhofer zone) becomes apparent in the bottom row, indeed this is clear from looking at the probability density functions for the intensity in figures 5.2. The negative exponential curve being an important indication of the saturation regime.

Figs 5.3 demonstrate the same as figs 5.1, here a Von Karman spectrum (equation 2.14) is used to filter the phase screen data.

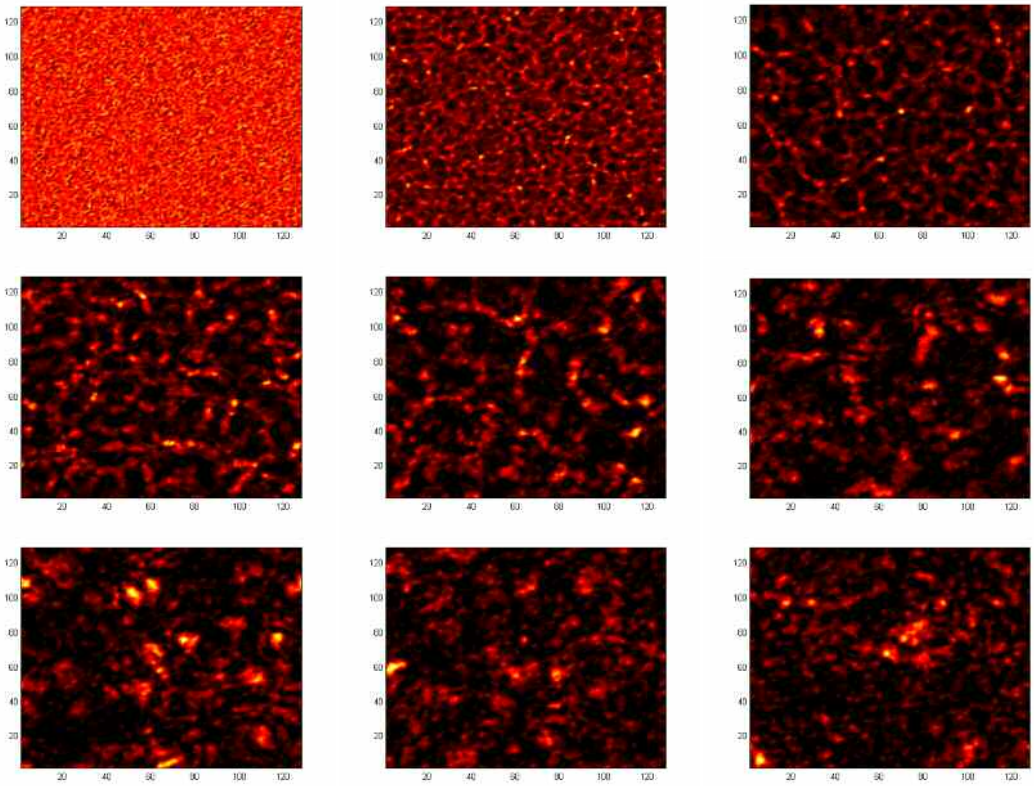

Figs 5.3, same as figs 5.1 but using phase screens filtered with a Von Karman function. Note the focussing and caustics, but they are less well-defined than in figs 5.1.

Here, 5 Von Karman phase screens were used, each with normalised mean square phase shifts of $\left\langle \phi_0^2 \right\rangle = 1$ and inner and outer scales such that $\kappa_I / \kappa_O = 50$. It is clear that figures 5.3 exhibit patterns similar to those created by the Gaussian correlated phase screens in figures 5.1, the caustics in the focussing regime are less well-defined though. This is due to the nature of the Von Karman screens which contain fine detail and a self-similar behaviour.

5.3. Beams solutions to the paraxial equation.

The previous section examined plane wave propagation through multiple phase screens. These simulations are useful for investigating the propagation regimes and testing some simple theories. The goal is to compare simulation to experiment, and as such beam profiles (as used in LIDAR systems) should be considered over and above plane waves. Whereas the plane and spherical waves used in analysis are idealised cases, the Gaussian beam is a more realistic model. The Gaussian beam arises as a solution to the paraxial equation of wave propagation (equation 2.6). The Gaussian beam solution can, however, be factored into a set of basis functions known as the Hermite polynomials. The Hermite polynomials $H_m(x)$ are solutions to the differential equation

$$H_m'' - 2\left(\frac{x}{q}\right)H_m' + 2mH_m = 0, \quad m = 0,1,2,..., \tag{5.2}$$

The solution to the paraxial equation, *U*, can then be expressed as

$$U_{m,n}(x,y,z) \sim H_m\left(\frac{\sqrt{2}x}{W_x(z)}\right)H_n\left(\frac{\sqrt{2}y}{W_y(z)}\right)\exp\left(-\frac{x^2}{W_x^2}-\frac{y^2}{W_y^2}\right)\times\{phase\ \ factors\} \tag{5.3}$$

where $U = \sum_m \sum_n U_{mn}$ and the properties of the beam are different in the two transverse directions *x* and *y* such that $W_{x,y}$ is the width (i.e. the 1 / *e* power point) of the beam in the appropriate direction.

A LIDAR system makes use of a Gaussian beam in order to concentrate the power of the laser in a central region, the Gaussian beam is so called because the field at the point of emission has a Gaussian shape, $E(x,y) = A\exp\left(\frac{-\left(x^2+y^2\right)}{W_0^2}\right)$ (fig 5.4), in the case of the lowest order solution $n = m = 0$. The beam is initially collimated, so there are no phase factors present until interaction with a phase screen.

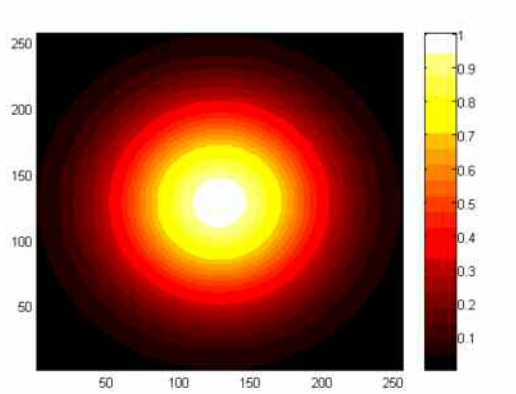

Fig. 5.4: A Gaussian beam with W_0 = 20cm, the size of the aperture is 1m.

Beam spreading is a phenomenon associated with diffraction. A beam propagating in free space will experience a level of spreading characterised by the angular spreading of the beam. This angle is of order λ / ($2W_0$), where λ is the wavelength and W_0 the initial radius of the beam. The level of spreading will increase with the addition of further phase factors and these in turn will increase with greater levels of turbulence.

A beam will naturally tend to diverge without focussing, a focussing parameter f_0 can be included in order to represent the effects of a lens being applied to the beam upon emission such that $E(x,y) = A\exp\left(\frac{-(x^2+y^2)}{W_0^2}\right)\exp\left(-i\frac{k(x^2+y^2)}{2f_0^2}\right)$. A value of $f_0^2 = \infty$ refers to a collimated beam (fig. 5.5), as used in these simulations.

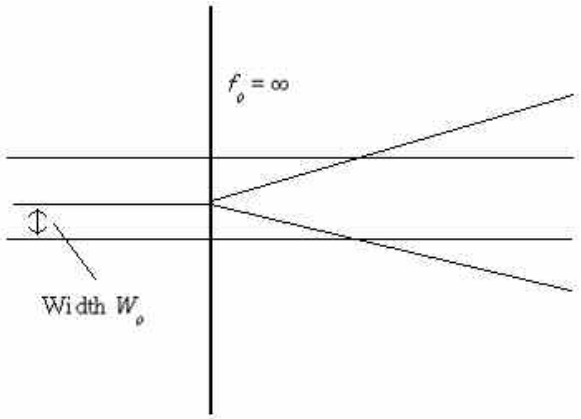

Fig. 5.5; a collimated Gaussian beam geometry. The focal point is at infinity, beam spreading occurs as the beam propagates.

5.3.1. Beam spreading and wander.

As noted above, spreading is a natural consequence of beam propagation, even in a vacuum, which increases in effect with the introduction of a strongly turbulent medium. Such a medium also causes wander as a result of the motion of eddies across the wave front. Theoretical analyses of spreading and wander phenomena have led to a number of results which can be tested using the 3-dimenional beam propagation algorithm. Yura [52, 67] and others calculated expressions for the beam spread in both 'long' and 'short' terms. The long term (LT) beam spreading includes the effects of beam wander while the short term (ST) spread considers spreading of the beam around the instantaneous beam centre, i.e. the effects of wander are removed.

The beam width $W(z)$ is the sum of the free space width and the turbulence induced beam spread. It can be shown that this is [52]

$$W^2(z) = W_0^2\left[1-\frac{z}{f_0^2}\right]^2 + \frac{z^2}{k^2 W_0^2} + \frac{8z^2}{k^2\rho_0^2}, \tag{5.4}$$

where W_0 is the initial beam radius, f_0^2 the focal length and ρ_0 the spherical wave coherence diameter given by

$$\rho_0 = \left[0.42k^2\int_0^L C_n^2(z)\left(\frac{z}{L}\right)^{5/3}dz\right]^{-3/5}. \tag{5.5}$$

In the case of a collimated wave, and upon defining $z_0 = \frac{\pi W_0^2}{\lambda}$,

$$W_{LT}^2(z) = W_0^2\left[1+\left(\frac{z}{z_0}\right)^2\right] + 2\left(\frac{2z}{k\rho_0}\right)^2 \tag{5.6}$$

This result is the LT beam radius, referred to henceforth as $W_{LT}^2(z)$. Yura [52] also looked at the short term radius $W_{ST}^2(z)$, he defined the spherical wave coherence diameter for the short term radius in terms of the above ρ_0, such that

$$\rho_0^{ST} = \rho_0^{LT}\left[1+0.37\left(\frac{\rho_0^{LT}}{4W_0}\right)^{\frac{1}{3}}\right]. \tag{5.7}$$

Using this it is possible to perform the same analysis as for the long term spread and arrive at an expression for the short term spread

$$W_{ST}^2(z) = W_0^2\left[1+\left(\frac{z}{z_0}\right)^2\right]+2\left(\frac{4z}{k\rho_0}\right)^2\left[1-0.26\left(\frac{\rho_0}{W_0}\right)^{1/3}\right]^2. \tag{5.8}$$

5.3.2. Numerical simulations, spreading and wander.

Numerical simulation is used to test the validity of equations (5.6) and (5.8). The simulation algorithm used here and throughout this chapter makes use of physical values rather than dimensionless parameters. Thus all simulations in this section use phase screens of $1m^2$ sampled by 2^8 points, Gaussian TEM_{00} beams with a radius of W_0 = 7cm and Von Karman filtered Gaussian random noise where the ratio of the inner to the outer scale is 50. Belmonte [7] performed a similar analysis to what follows, therefore similar values for the wavelength and the refractive index structure parameter are used. Single phase screens are used, as opposed to Belmonte's use of an extended medium modelled by 20 screens, to model the turbulent atmosphere.

Data was taken on the beam spreading and wander for several propagation conditions over a range of propagation distances.

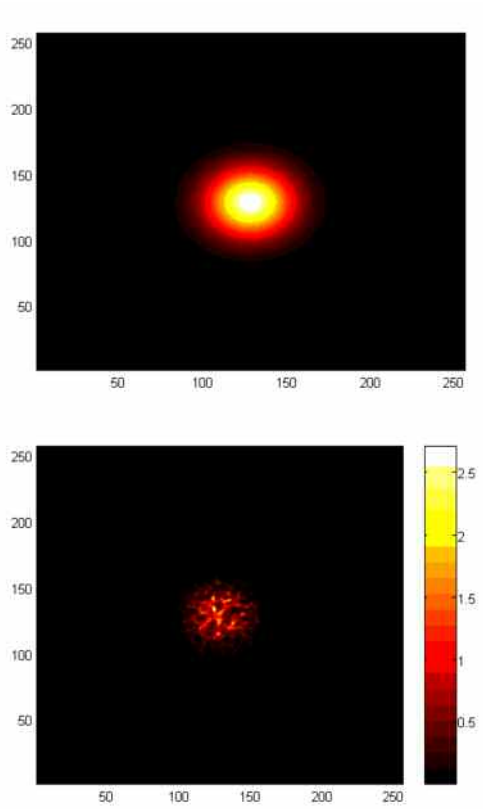

Figures 5.6 and 5.7: The initial Gaussian beam and the same beam at 100 metres ($C_n^2 = 10^{-12}$ m$^{-2/3}$ i.e. very strong turbulence, $\lambda = 10^{-6}$m).

The beam wander β is calculated by taking a simple sum over the intensity data in the propagated beam

$$\beta(z) = \frac{\sum_{all\ \rho} \rho EE^*}{\sum_{all\ \rho} EE^*}, \tag{5.9}$$

where E is the electric field and ρ is the radial distance of a point in the screen from the centre. I.e. $\rho^2 = x^2 + y^2$, $x = y = 0$ is at the initial beam centre. The width of the beam is calculated by averaging over the intensity profiles of several hundred sample beams and interpolating a best-fit quartic curve to the resulting profile. It is then possible to extract the point at which the intensity falls to the 1 / e value. The algorithm used to perform these tasks makes use of the polynomial interpolation package in *Matlab* v. 6.1.

Averaging over several hundred realisations allows for a smoothing of the statistics obtained. Figures 5.6 through to 5.9 show sample beam propagations that are used in the following simulations, the spreading of the beam at large propagation distances is clearly visible. Less obvious, perhaps, is the beam wander, although in figures 5.8 and 5.9 one can see the that brightest spot in the beam (i.e. the greatest concentration of power) is no longer located at the centre of the image.

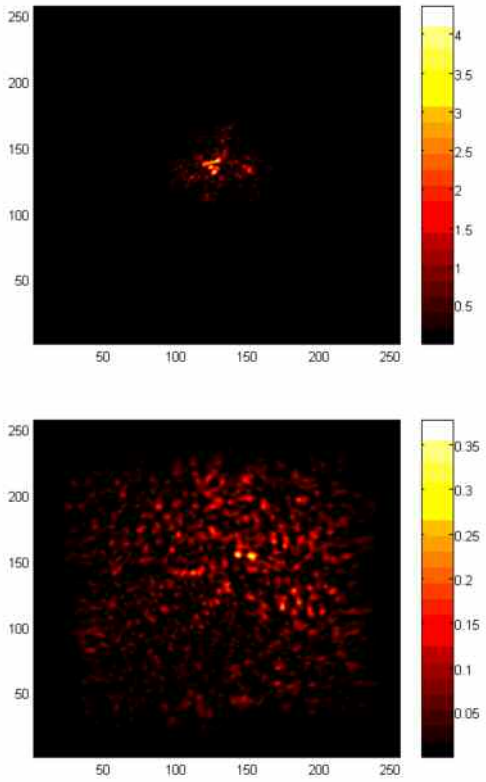

Figures 5.8 and 5.9; The Gaussian beam (fig 7) propagated to 500m and 1.5km ($C_n^2 = 10^{-12}\,\mathrm{m}^{-2/3}$, $\lambda = 10^{-6}$m).

Figures 5.10 and 5.11 show the beam spreading for two different strengths of turbulence. Note first that the spreading in the beam requires a greater distance to develop in weaker turbulence.

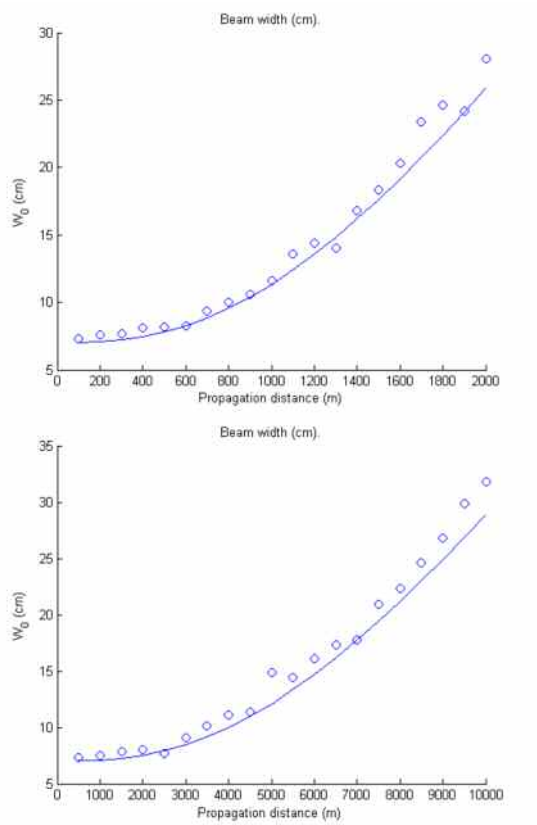

Figs 5.10 ($C_n^2 = 10^{-12}$, strong turbulence) and 5.11 ($C_n^2 = 10^{-14}$, medium turbulence).

The simulation data in figures 5.10 and 5.11 is represented by symbols, theory (equation 5.6) is the unbroken line. There is a good match between theory and data.

Figures 5.12 and 5.13 (below) show the beam wander results for the same simulations a those described above. The theoretical curves for the wander are developed in [7] as the difference between the long term and short term beam spread. Here there is some discrepancy between simulation and theory.

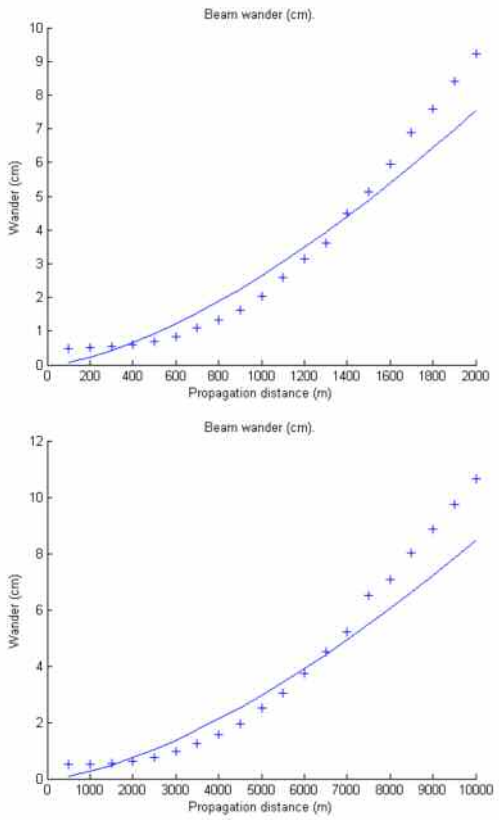

Figs 5.12 ($C_n^2 = 10^{-12}$, strong turbulence) and 5.13 ($C_n^2 = 10^{-14}$, medium turbulence).

There exists some divergence in the Fraunhofer regime between theory and simulation. This can be explained by noting that in the far field the beam no longer has a Gaussian shape; therefore one cannot expect the theory (which is reliant on the fact that the beam is a Gaussian) to be accurate in that regime. Note also that the theory uses a pure power law Kolmogorov spectrum, which fails to model the effects of the large eddies caused by the presence of an outer scale. The motion of large eddies across the wave front has an important effect on the beam wander, the inclusion of an outer scale in the turbulence model is causing discrepancies between theory and simulation at large propagation distances.

5.4. Temporal phase statistics in 3-dimensional simulations.

The beam spread and wander statistics examined in section 5.3 are spatial statistics. To examine temporal statistics a temporal variation must be included in the model as discussed in chapter 4. In three dimensions this is done by transposing the phase screens and allowing the beam to propagate to the observation screen at each

transposition. Thus a complete picture of the evolution of the beam is built up as the turbulence develops, in this way the 'frozen-in' turbulence present in the phase screens is used to represent a block of turbulence moving across the wave front. The screens move at a velocity *v*.

5.4.1. Use of rectangular screens in temporal phase statistics.

Section 5.1 included a discussion of the memory considerations involved in performing three-dimensional simulations. This becomes a greater drain on computer resources when setting the screens in motion. These memory problems can be addressed by using phase screens which are elongated in the direction of motion. A typical example involves an aperture of $2^8 \times 2^8$ sampling points with a screen of $2^8 \times 10 \times 2^8$ sampling points such that there are 10×2^8 points in the direction of motion. This will result in 3 decades of information in a spectral plot without having to perform a simulation that uses a series of $2^{14} \times 2^{14}$ screens.

The use of rectangular phase screens presents a neat solution to these memory problems. The use of square phase screens of size 2^n by 2^n can abandoned in favour of the use of rectangular screens of size 2^n by $m2^n$ if the following conditions hold[12]:

- The aperture size is 2^n by 2^n.
- Any 2^n by 2^n segment of the rectangular screen has the same statistics as a 2^n by 2^n screen produced by method detailed in section 2.3.
- The frozen-in turbulence only moves in one direction, i.e. along the *y*-direction of the rectangular screen.
- The number of samples in the temporal evolution of the propagated field is equal to $(m-1)2^n$.

[12] The length of size 2^n is the '*x*' direction, the side of length $m2^n$ is the '*y*' direction

Figure 5.14 (below) gives a simple pictorial representation of the simulation technique using rectangular phase screens.

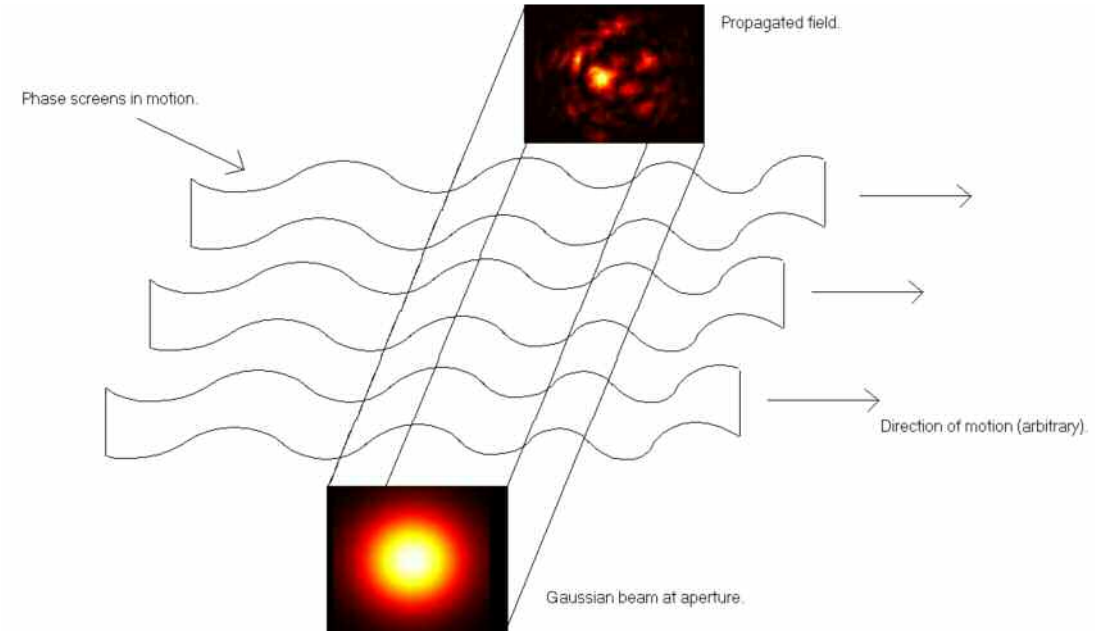

Fig. 5.14. Three rectangular phase screens pass in front of the Gaussian beam wave front producing a perturbed field. The screens move from left to right.

One can see the aperture (size 2^n by 2^n) and the screens of size 2^n by $m2^n$ passing through the propagating field. Multiple phase screens are used, just as in two-dimensions, to model an extended medium. The simulation process for a three-dimensional model simulating an extended medium using multiple rectangular screens is then as follows:

- Generate an array of pseudo-random Gaussian random numbers of size $2^n \times m2^n$ (one for each required phase screen).
- Use an appropriate filter to give the screens the correct statistics.
- Set up the beam in a $2^n \times 2^n$ aperture.
- The beam propagates through a 2^n by 2^n segment at one edge of the rectangular screens. Record the propagated field at the observation screen.
- Transpose each of the phase screens one step in the *y* axis.
- Perform the next propagation and record the field data.
- Cycle through the previous 2 steps until reaching the far end of the rectangular phase screens (i.e. $(m-1)2^n$ times).

- The resulting data set gives the field's temporal evolution over $(m-1)2^n$ time steps.

Using this simulation technique allows for the investigation of temporal phase statistics, given an assumption of frozen-in turbulence.

5.5. An alternative to the Kolmogorov pure power law; subharmonics.

Before proceeding to some simulation results using rectangular screens, it is instructive to note some interesting characteristics about these screens. Firstly, the overall phase change from one side of the screen to the other (along the length, *y*) can be very large. Secondly, phase fluctuations that occur over the entire *y* axis of the screen must be modelled, rather than being restricted to those bounded by the *x* axis. This is important because fluctuations over very long ranges are possible and their inclusion in the simulations are crucial to the validity of statistics.

Hitherto the Von Karman spectrum has been used as a filter for the phase screens when modelling Kolmogorov turbulence. This model has the advantage that it imposes high and low frequency cut-offs to the spectrum which attempt to model the effects of the outer and inner scales. The disadvantage is that the locations of such cut-offs are arbitrary and suppress spectral information at very low and very high frequencies. This removal of low frequency components from the spectrum prevents large scale features in the turbulence, i.e. fluctuations occurring over the entire *y* axis, from being modelled accurately. A method of including such fluctuations in rectangular screens is required.

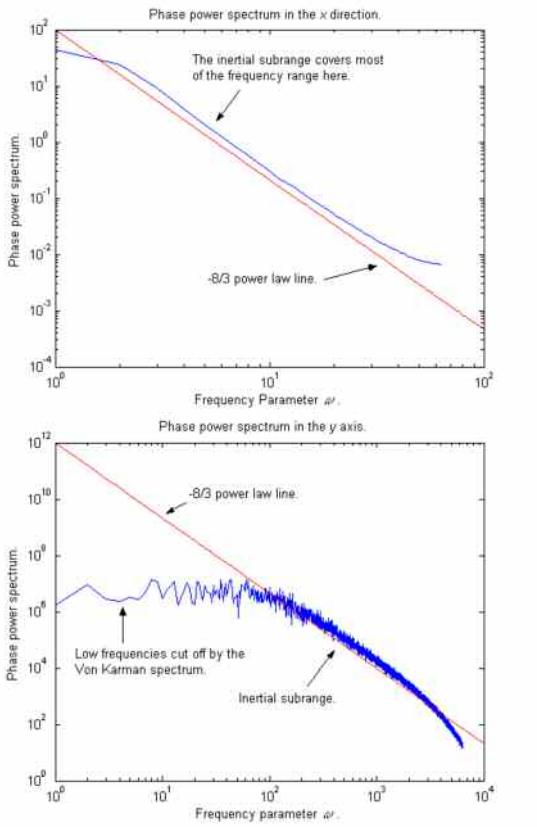

Figs 5.15 and 5.16, showing phase power spectra averaged over the two different sides of a rectangular phase screen.

Consider figures 5.15 and 5.16, which illustrate the problem. A rectangular phase screen of size $2^8 \times 100.2^8$ was created using a Von Karman (equation 2.14) filter with outer and inner scales. Comparing the phase spectrum of the screen along the *x* axis (fig. 5.15) with the same spectrum in the *y* axis (fig. 5.16) indicates how low frequencies are being suppressed. This loss of power at low frequencies represents an absence of any long range fluctuations in the *y* direction of the phase screen.

A theory which allows for the accurate sampling of low frequencies in the Kolmogorov spectrum was proposed in [20], developed further in [23] while being used in [37] . It is impossible to sample a pure power law Kolmogorov spectrum, i.e. $\Phi_n(\kappa) \sim \kappa^{-11/3}$, to arbitrarily low frequency space values[13] because the spectrum diverges as κ tends to 0. The use of 'subharmonics' in the sampling of the spectrum

[13] The sampling of low frequencies is essential for long range fluctuations to be modelled in the phase screen. The sample size used in the grid puts a natural limit on the length of fluctuations that can be observed in the screen. In order to accurately sample 'long' phase screens it is necessary to include these low frequencies.

is proposed [20] as a method of avoiding this problem. The technique is so named because it involves splitting the sample located at $\kappa = 0$ (i.e. the point at which $\Phi_n(\kappa) \to \infty$) into a number of smaller samples as indicated in figure 5.17.

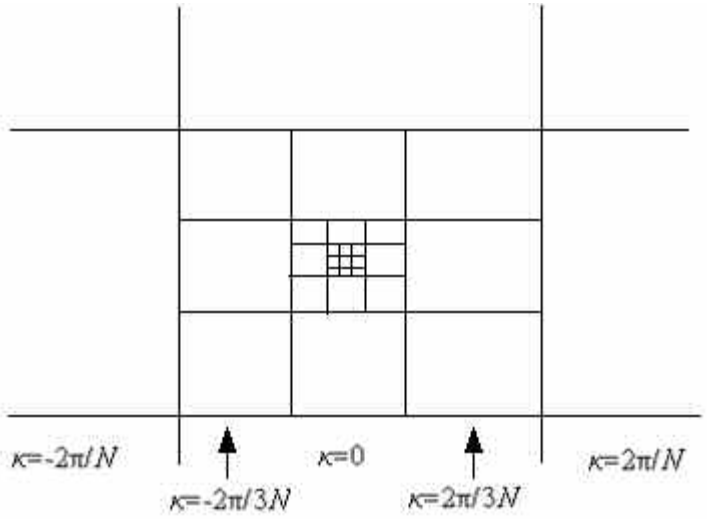

Figure 5.17. Showing the two-dimensional sampling grid close to κ = 0.

The large central square in figure 5.17 represents the sample for $\kappa = 0$ in the two-dimensional grid from which the Kolmogorov spectrum is sampled. To the left and right are the first non-zero samples; given that there are *N* samples in the grid these are multiples of $\pm 2\pi/N$. Note that $\pm 2\pi/N$ is used in an idealised dimensionless case where the total frequency domain is $\kappa \in (-\pi, \pi)$. In a physically realistic simulation, the frequency domain is $\kappa \in (-\pi N/L, \pi N/L)$ such that the sampling interval is $2\pi/L$ where *L* is the length of the phase screen. Returning to figure 5.17, the central sample at $\kappa = 0$ has been divided into 9 smaller squares, each of which has side $2\pi/3N$. The most central square is still located at $\kappa = 0$. It is possible to include further levels of subharmonics by continuing to divide the central square into smaller and smaller segments, the second level of subharmonics is shown within the central square of figure 5.17. The size of the p^{th} level of harmonic will be $2\pi/3^p N$. Thus it is possible to sample the element in the grid that would otherwise give an infinite value for $\Phi_n(\kappa)$. Of course one cannot sample these harmonics infinitely, and eventually a central square will be left at $\kappa = 0$ (albeit representing a very small sample space) which can be set to $\Phi_n(\kappa) = 0$. Doing this will allow the inclusion of

longer range and lower frequency fluctuations into the phase screens, thus eliminating the loss of information seen in figure 5.16.

An alternative algorithm, for the calculation of the subharmonic contribution ϕ_{sub} to the phase screens, has been proposed to cope with the modified sampling technique [23]. The standard fast Fourier transform algorithm assumes that the sampling interval is constant; the new algorithm weights the subharmonic samples based on the size of each sample. The proposed fast Fourier transform algorithm is

$$\phi_{Sub}(j\Delta x, l\Delta y) = \sum_{p=1}^{N_{SH}} \sum_{n_x=-1}^{1} \sum_{n_y=-1}^{1} \phi\left(p, n_x, n_y\right) \exp\left[\frac{2\pi i n_x j}{3^p L_x} + \frac{2\pi i n_y l}{3^p L_y}\right], \tag{5.10}$$

where Δx and Δy are the sampling widths in the x and y directions, L_x and L_y are the lengths of the screen in the x and y directions. $\phi\left(p, n_x, n_y\right)$ are random complex Gaussian processes that have been given the correct autocorrelation properties, N_{SH} refers to the number of subharmonics that will be taken while n_x and n_y are references to the 3 by 3 grid on which the subharmonics are sampled. The greater the value of N_{SH}, the more accurate the statistics will be, but the longer the simulation will take. The remaining samples in $\kappa \in \left(-\pi N/L, \pi N/L\right)$, excluding $\kappa = 0$, are used to calculate a phase screen ϕ_{screen} in the normal way. The resulting subharmonic screen is simply the sum $\phi_{sub} + \phi_{screen}$.

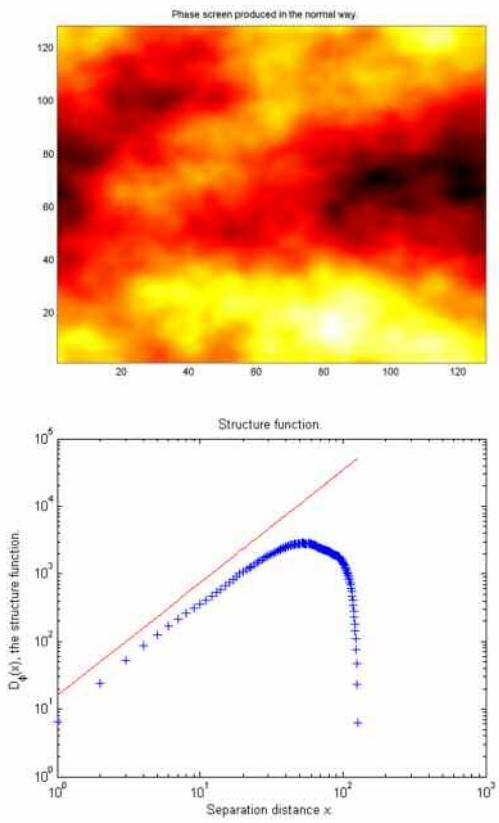

Figures 5.18 and 5.19. A Kolmogorov phase screen and associated structure function, symbols indicate simulation, solid line is theory [23].

Figure 5.18 shows a Kolmogorov phase screen produced in the normal way with $\Phi_n(\kappa) \sim \kappa^{-11/3}$, i.e. with the central $\kappa = 0$ sample set to zero to avoid an infinity. Note that the screen is periodic, this is clear as the structure function (figure 5.19) returns to zero as the separation distance approaches the size of the screen. This is due to the periodic nature of the fast Fourier transform methods used to produce the screen.

Consider figure 5.20 (below). The phase screen in figure 5.20 clearly has non-periodic behaviour. The structure function (figure 5.21) shows a 5/3 power law behaviour for all separation distances *x*. The phase screen in figure 5.20 therefore contains long range phase fluctuations; this is in stark contrast to the phase screen in figure 5.18 where all fluctuations are contained within the confines of the periodicity of the screen.

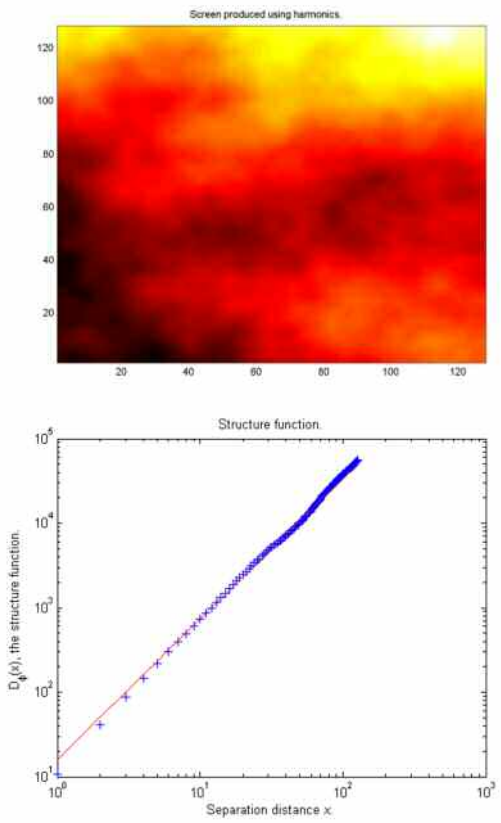

Figures 5.20 and 5.21. A Kolmogorov phase screen produced using the subharmonics algorithm, structure function (equation 2.10) is also displayed.

These are the properties which are required in rectangular screens. More accurate statistics are expected for low frequencies when using the subharmonic screen generation.

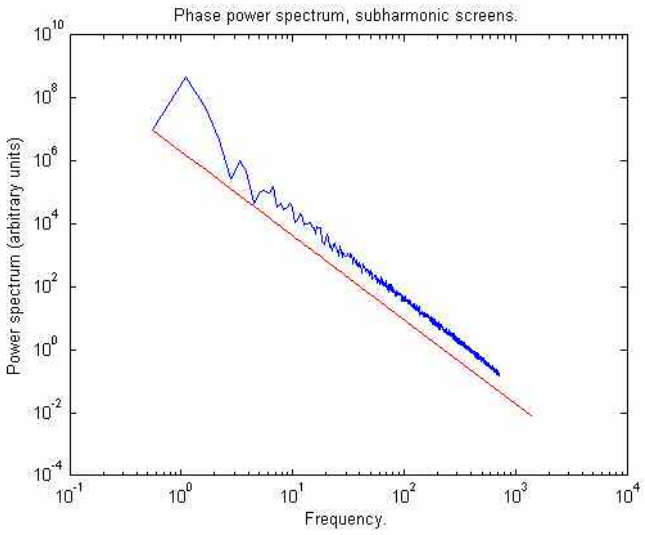

Figure 5.22. The phase power spectrum along the *y* axis of a phase screen using $2^8 \times 10.2^8$ points.

The sample phase power spectrum shown in figure 5.22 indicates that the additional low frequencies have been added to the phase screen. Comparison with figure 5.17 shows a marked difference in the low frequency behaviour of this spectrum, the subharmonic algorithm has successfully corrected for the loss of power at low frequencies associated with a Von Karman spectrum.

5.6. Temporal phase spectra, analysis.

5.6.1. Beam analysis.

In a series of papers written in the late 1960's [35, 69, 70, 71 and 72], Ishimaru performed an analysis of the temporal properties of a focussed beam propagating through atmospheric turbulence. He argued that beams are much more useful than plane or spherical waves for probing atmospheric characteristics because one can adjust the focussing and aperture size easily. His analysis begins with an assumption of weak turbulence (i.e. $n(r,t)=1+n_1(r,t)$ where $n_1 << 1$) and that the refractive index fluctuations obey the Taylor frozen-in hypothesis (i.e. $n_1(r,t)=n_1(r-vt,0)$) where v is the average wind velocity. Application of the Rytov approximation (see equations (1.1) to (1.3))expresses the propagated field in terms of a phase fluctuation

$$\Psi_1(r,t)=\frac{k^2}{2\pi U_0(r)}\int_{V'} n_1(r',t)U_0(r')\frac{\exp\{ik|r-r'|\}}{|r-r'|}dV' \qquad (5.11)$$

where the initial field U_0 and the final field U are related by

$$U(r,t)=U_0(r)\exp\{\Psi_1(r,t)\}. \qquad (5.12)$$

One can write Ψ_1 in terms of its real (χ, the log-amplitude) and imaginary (S, the phase) parts and derive certain statistical quantities. The interesting result concerns the temporal correlation function for the log amplitude χ,

$$B_\chi(\tau) = A\int_0^\infty \mathrm{K}d\mathrm{K}\int_0^1 dz' J_0(q\omega_0\tau)\sin^2\left[\frac{z'q^2(1-\delta_1 x')}{2}\right]\Phi_n(\mathrm{K})\exp\left[-\delta_2 z'^2 q^2\right] \qquad (5.13)$$

where $A = 2\pi^2 k^2 L$, $q = \mathrm{K}\sqrt{L/k}$, $z' = z/L$ and $\omega_0 = V\sqrt{k/L}$, z is the direction of propagation, L the total propagation distance, k the wave number and it is assumed that the initial field U_0 is a Gaussian. Re-working Ishimaru's calculation to obtain the phase (S) equivalent to equation (5.13) and taking the cosine transform (see section 4.2.1) gives an integral expression for the temporal spectrum of the phase, i.e.

$$W_\phi(\omega) = 8\pi^2 k^3 \int_{\omega/\omega_0}^\infty qdq\int_0^1 dz' \frac{\Phi_n(\mathrm{K})}{\sqrt{q^2\omega_0^2 - \omega^2}}\cos^2\left[\frac{z'q^2(1-\delta_1 x')}{2}\right]\exp\left[-\delta_2 z'^2 q^2\right] \qquad (5.14)$$

where δ_1 and δ_2 arise from the beam parameters [72]. Notice that this can be reduced to the form given by Tatarski [36] by setting $\delta_1 = \delta_2 = 0$ (plane wave). An analytical solution to this equation for arbitrary $\delta_{1,2}$ appears to be impossible to calculate. One can proceed by integrating numerically after choosing an appropriate form for the spectrum of refractive index fluctuations ($\Phi_n(\kappa) \sim C_n^2 \kappa^{-11/3}$ the pure power law Kolmogorov or $\Phi_n(\kappa) \sim C_n^2 \kappa^{-11/3}\exp\left(-\kappa^2/\kappa_I^2\right)$ the Tatarski spectra[14]) and values for the beam parameters δ_1 and δ_2.

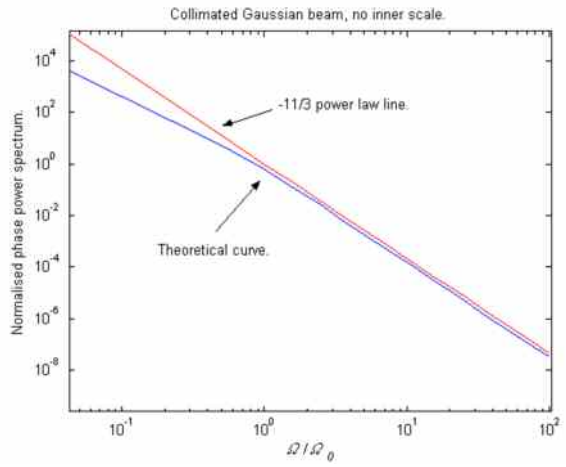

8

[14] Fante and Frehlich [44 and 45] discussion the importance of the inner scale κ_I and its effect on intensity statistics under strong turbulence conditions. Several papers [40 and 43] also discuss experimental methods used to measure the inner scale using log-intensity variances.

Figure 5.23: The theoretical curve is a numerical integration of equation 5.14 using δ_1 = 0.04 and δ_2 = 0.2 (collimated beam) for a pure power law Kolmogorov spectrum.

The crucial feature in figure 5.23 is the power law behaviour of the power spectrum, a $-11/3$ law occurs as opposed to the $-8/3$ power law predicted in the case of a plane or spherical wave (see section 4.2.1). This can also be seen in figure 5.24 (below) for a Tatarski spectrum.

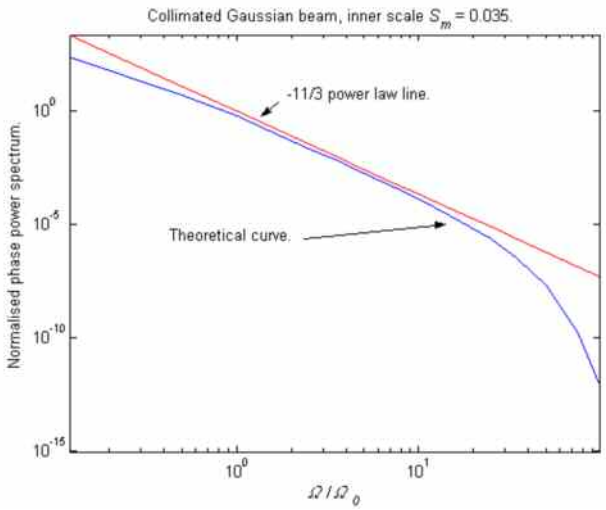

Figure 5.24: as figure 5.23 but using Tatarski refractive index spectrum.

Figure 5.24 shows the high frequency cut off imposed by the Tatarski spectrum as well as a $-11/3$ power law behaviour in the inertial subrange. The conclusion is that, for a Gaussian beam (under conditions where a Rytov approximation is valid), a $-11/3$ power law behaviour is expected in the phase / log amplitude power spectra rather than a $-8/3$ behaviour (as one would expect for plane or spherical waves [36]).

5.6.2. Spherical wave analysis.

Clifford [30] calculated the phase power spectrum for a plane wave propagating through a weakly turbulent layer characterised by a pure power law Kolmogorov spectrum. This calculation can be performed again using a Tatarski spectrum in order to find a spherical wave limit to Ishimaru's result (equation 5.14). It is important to

find out whether the $-11/3$ behaviour seen in figures 5.23 and 5.24 is solely a result of the presence of a beam or the a result of the use of a Tatarski spectrum.

The pure power law Kolmogorov spectrum used by Clifford is

$$\Phi_n(\kappa) = 0.033 C_n^2 \kappa^{-11/3}, \tag{5.15}$$

including Tatarski's inner scale modification obtains

$$\Phi_n(\kappa) = 0.033 C_n^2 \kappa^{-11/3} \exp\{-\kappa^2/\kappa_I^2\} \tag{5.16}$$

where κ_I is the inner scale equal to $2\pi/l_0$. Incorporating this spectrum into Clifford's calculation (equation 12 in [30]) gives

$$W_{\chi,S}(f) = A\Omega^{-\frac{8}{3}} \int_0^1 du \int_0^\infty \frac{\sigma^{-\frac{1}{2}} d\sigma}{(\sigma+1)^{11/6}} \left\{ 1 \text{m} \cos\left(-\frac{\Omega^2}{4}(\sigma+1)(1-u^2) \right) \right\} \exp\left(-S_m^2 \sigma\right) \tag{5.17}$$

where $S_m = \dfrac{2\pi f}{\kappa_I}$, $\Omega = \dfrac{f}{v}\sqrt{2\pi\lambda L}$, $\dfrac{u+1}{2} = \dfrac{z}{L}$, $\sigma + 1 = \left(\dfrac{kv}{2\pi f}\right)^2$, z the propagation distance, L the distance to the observation plane, k the wave number, f the frequency parameter and $A = 0.132\pi^2 k^{2/3} L^{7/3} C_n^2 v^{-1} \exp\left(-(2\pi f)^2/\kappa_I^2\right)$.

This integral is completed by first splitting it the sum of two parts $W_{\chi,S}(f) = W_{\chi,S}^1(f) + W_{\chi,S}^2(f)$. The first of these integrals has no u-dependence,

$$\begin{aligned} W_{\chi,S}^1(f) &= A\Omega^{-\frac{8}{3}} \int_0^1 du \int_0^\infty \frac{\sigma^{-\frac{1}{2}} d\sigma}{(\sigma+1)^{11/6}} \exp\left(-S_m^2 \sigma\right) \\ &= A\Omega^{-\frac{8}{3}} \left\{ \frac{\sqrt{\pi}\Gamma\left(\frac{1}{3}\right)}{2\Gamma\left(\frac{11}{6}\right)} {}_1F_1\left(\frac{3}{2}, \frac{2}{3}, S_m^2\right) + S_m^{2/3}\Gamma\left(-\frac{1}{3}\right) {}_1F_1\left(\frac{11}{6}, \frac{4}{3}, S_m^2\right) \right\} \end{aligned} \tag{5.18}$$

where ${}_1F_1$ is a hypergeometric function [75]; the second integral can be written as

$$W^2_{\chi,S}(f) = A\Omega^{-\frac{8}{3}} \int_0^1 du\, \mathrm{Re}\left\{ \int_0^\infty \frac{\sigma^{-\frac{1}{2}} d\sigma}{(\sigma+1)^{11/6}} \exp\left(-\frac{i\Omega^2}{4}(\sigma+1)(1-u^2) \right) \exp\left(-S_m^2 \sigma\right) \right\}. \quad (5.19)$$

Integration over σ gives

$$W^2_{\chi,S}(f) = A\Omega^{-\frac{8}{3}} \int_0^1 du\, \frac{\exp(iz)}{2\Gamma\left(\frac{11}{6}\right)} \left\{ \sqrt{\pi}\Gamma\left(\frac{1}{3}\right) {}_1F_1\left(\frac{3}{2}, \frac{2}{3}, S_m^2 - iz\right) + \mathrm{K} \right. \quad (5.20)$$
$$\left. \mathrm{K}\, 2\Gamma\left(-\frac{1}{3}\right)\Gamma\left(\frac{11}{6}\right)\left(S_m^2 - iz\right)^{1/3} {}_1F_1\left(\frac{11}{6}, \frac{4}{3}, S_m^2 - iz\right) \right\}$$

where[15] $z = -\frac{\Omega^2}{4}\left(u^2 - 1\right)$. This integral differs from those calculated by Clifford in appendix A of [30] because of the inclusion of the inner scale term S_m^2 in the hypergeometric functions. Noting a property of the hypergeometric functions:

$$e^{-x} {}_1F_1(a,b,x) = {}_1F_1(b-a,b,-x)$$
$$\Rightarrow \exp(-iz) {}_1F_1\left(a,b,S_m^2 + iz\right) = \exp\left(-S_m^2 - iz\right) {}_1F_1\left(a,b,S_m^2 + iz\right)\exp\left(S_m^2\right)$$
$$= \exp\left(S_m^2\right) {}_1F_1\left(b-a,b,-\left(S_m^2 + iz\right)\right)$$

the subsequent integral over u can be written as an integral in z:

$$W^2_{\chi,S}(f) \sim \int_0^t t^{-1/2}(t-z)^{-1/2} dz \left\{ \frac{\sqrt{\pi}\Gamma\left(\frac{1}{3}\right)}{2\Gamma\left(\frac{11}{6}\right)} {}_1F_1\left(-\frac{5}{6}, \frac{2}{3}, -\left(S_m^2 - iz\right)\right) + \mathrm{K} \right. \quad (5.21)$$
$$\left. \mathrm{K} + 2\Gamma\left(-\frac{1}{3}\right)\left(S_m^2 - iz\right)^{1/3} {}_1F_1\left(-\frac{2}{3}, \frac{4}{3}, -\left(S_m^2 - iz\right)\right) \right\}$$

[15] z is not the propagation distance here, rather a normalised frequency parameter defined in Clifford's work [30]. The propagation distance information is contained in u.

where $t = \frac{\Omega^2}{4}$. There are two different class of integral here, setting $-\left(S_m^2 - iz\right) \to ix$ gives

$$W_{\chi,S}^2(f) \sim t^{-1/2} \int_{iS_m^2}^{iS_m^2+t} \left(t + iS_m^2 - x\right)^{-1/2} {}_1F_1\left(-\frac{5}{6}, \frac{2}{3}, ix\right) dx + \mathrm{K}$$
$$\mathrm{K} + t^{-1/2} \int_{iS_m^2}^{iS_m^2+t} \left(t + iS_m^2 - x\right)^{-1/2} (-ix)^{1/3} {}_1F_1\left(-\frac{2}{3}, \frac{2}{3}, ix\right) dx \qquad (5.22)$$

These integrals are the same as the ones obtained by Clifford [30] (apart from some additional constants introduced by the shift in the integration limits and different hypergeometric coefficients). Therefore, given that the integration of equation (5.18) resulted in a $-8/3$ power law, the power law behaviour of $W_{\chi,S}(f) = W_{\chi,S}^1(f) + W_{\chi,S}^2(f)$, i.e. $-8/3$, in the inertial subrange will be unchanged from Clifford's result. There is a fundamental difference between the phase spectrum resulting from a Gaussian beam and that resulting from a plane or spherical wave. This fundamental difference is causing the power law behaviour seen in figures 5.23 and 5.24.

5.7. Simulation results.

A series of numerical simulations are presented that use the techniques discussed above. Multiple phase screens in two dimensions are used to model three-dimensional propagation problems. Screens are set in motion across the plane of propagation at speed *v*, the aperture is defined of size $n \times n$ while the phase screens used are of size $n \times mn$. Several propagation geometries are simulated, the temporal phase spectra produced are then analysed.

5.7.1. Plane waves, pure power law spectra.

Parameters used in these simulations are λ = 1μm and v = 2ms^{-1}. The observation screen is located at L = 10km, thus the observed wave is expected to be in the far

field. The size of the aperture is 40cm while the plane wave is 20cm by 20cm. These simulations use 20 phase screens of size $n \times mn$ where $n = 2^8$ and $m = 5$.

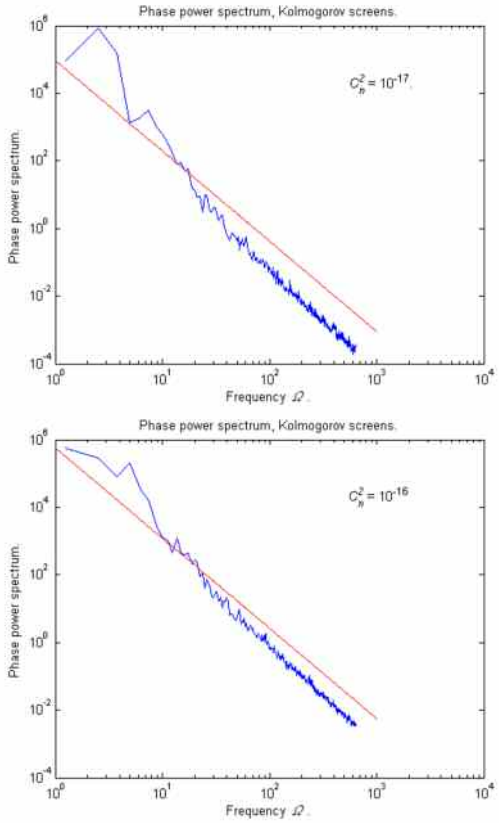

Figures 5.25 and 5.26. Weak turbulence, note the -8/3 power law behaviour across the entire range of frequencies.

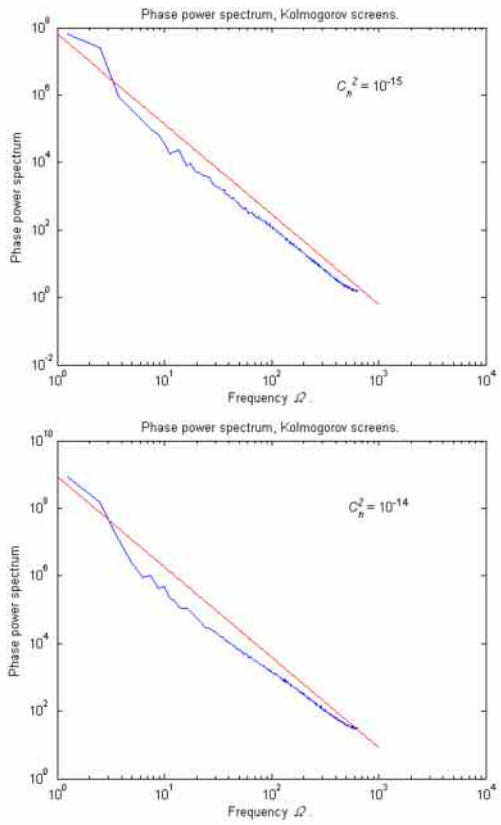

Figures 5.27 and 5.28. Intermediate and strong turbulence. Figure 5.28 shows a familiar increase in the power law for high frequencies.

Note that, contrary to previous simulations using Von Karman spectra, there is no high-frequency cut-off in the spectrum resulting from the lack of an inner scale filter in the pure power law Kolmogorov spectrum. All four figures show no flattening of at low frequencies, a result of the subharmonic algorithm. Each figure, except figure 5.28, displays a clear $-8/3$ power law with the absolute value of the spectra increasing with stronger turbulence. Figure 5.28, $C_n^2 = 10^{-14}$, shows a departure from the $-8/3$ law at high frequencies. This has been seen in the two-dimensional simulations of section 4.3 and will be encountered again in the following sections.

5.7.2. Plane waves, Tatarski spectra.

The following simulation results were performed using a Tatarski spectrum (equation 5.15) to filter the phase screen data. Identical parameters were used in these simulations as in section 5.7.1.

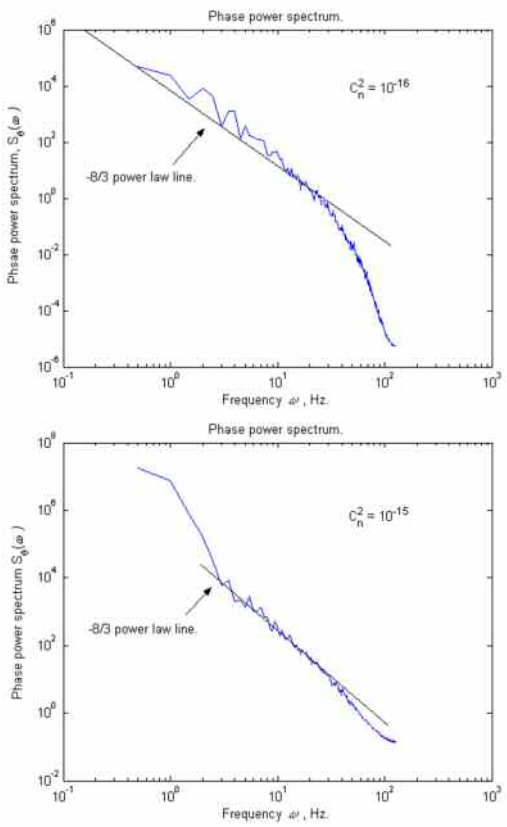

Figures 5.29 and 5.30. Weak propagation regimes are shown, note the -8/3 power law behaviour in the inertial subrange.

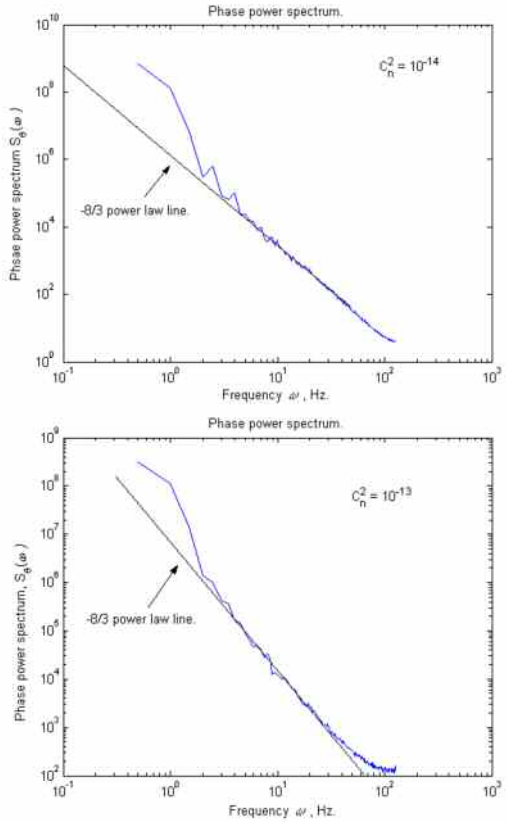

Figures 5.31 and 5.32. Intermediate and strong propagation regimes. Note a -8/3 power law regimes and a higher power law behaviour at higher frequencies.

Figures 5.29 and 5.30 clearly indicate a roll off in the spectrum at high frequencies, this is expected as the Tatarski spectrum includes a filter at the inner scale. Note that this roll off in the spectrum disappears in the strong turbulence cases (figures 5.31 and 5.32) and a departure from the $-8/3$ power law is seen at high frequencies. Once again all figures clearly show no cut-off at low frequencies as expected from the subharmonic filtering technique.

5.7.3. Gaussian Beams, pure power law spectrum.

Now consider Gaussian beams in an extended medium with statistics governed by the pure power law Kolmogorov spectrum (5.14). An aperture of size 40cm is used as well as a TEM_{00} Gaussian beam with parameters W_0 = 7cm and $f_0 = \infty$. 20 independent phase screens are used with the following parameters: λ = 1μm, l_0 = 5mm, L_0 = 30cm, , $v = 2\text{ms}^{-1}$, $n = 2^8$, m = 5 and z = 4km.

It has been shown (figures 5.23 and 5.24 and [72]) that a $-11/3$ power law is expected under conditions of weak turbulence. For each propagation geometry a sample beam and the phase power spectrum is considered.

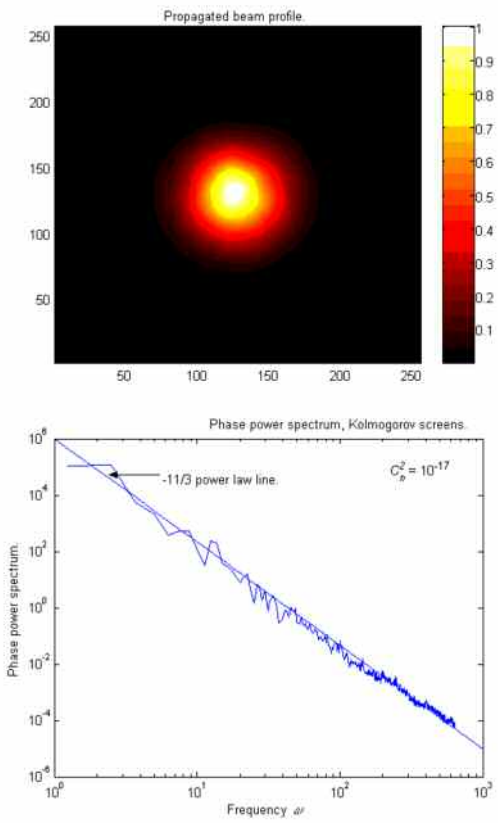

Figures 5.33 and 5.34, $C_n^2 = 10^{-17}\text{m}^{-2/3}$. The phase power spectrum follows a -11/3 power law.

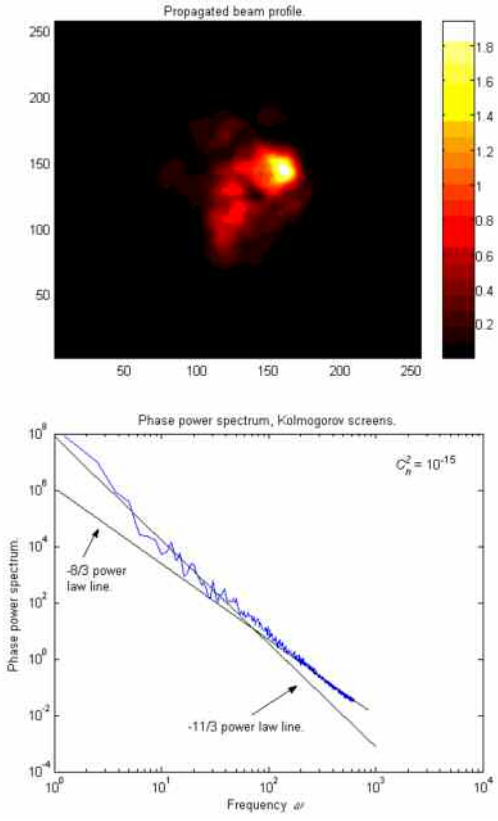

Figs 5.35 and 5.36, $C_n^2 = 10^{-15}\text{m}^{-2/3}$. The phase power spectrum follows a -11/3 power law at low frequencies before adjusting to a -8/3 behaviour as the frequency ω increases.

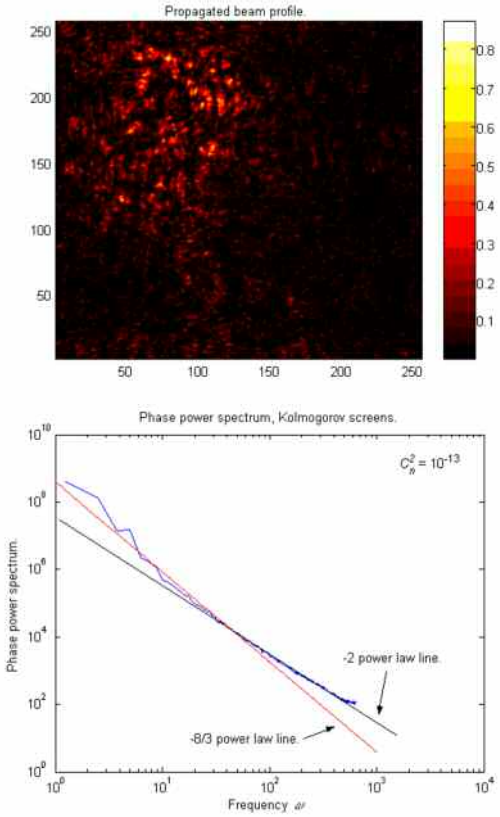

Figs 5.37 and 5.38, $C_n^2 = 10^{-13}\text{m}^{-2/3}$. Under this strong propagation condition, there is evidence of wander in the beam and the phase power spectrum reaching a -2 power law.

Sample images of the propagated field are shown in each case. Figures 5.33 and 5.34 show a weak propagation region, and indeed the $-11/3$ power law regime is present. Moving into an intermediate regime (figures 5.35 and 5.36) the picture is less clear, there are two distinct regions; a low frequency one with a $-11/3$ power law, and a higher frequency regime where there is evidence of a $-8/3$ power law. In the case of a much higher level of turbulence (figures 5.37 and 5.38), there is a -2 power law at high frequencies. Figure 5.37 shows the extent of the spreading and wander in the beam under such conditions, it is clear that this is the far field.

5.7.4. Beam waves, Tatarski spectrum.

These simulations use the same conditions as those in section 5.7.3, in addition the phase screens have the statistical properties of a Tatarski spectrum (5.15). Figures

5.39 and 5.40 confirm Ishimaru's prediction concerning the $-11/3$ power law behaviour under weak turbulence conditions. Now contrast figures 5.41 and 5.42 (below) with figures 5.35 and 5.36 (above). In figure 5.42 the phase power spectrum does not undergo a transition to a $-8/3$ power law at high frequencies, in contrast to the spectrum in figure 5.36. The behaviour is likely due to the use of a Tatarski spectrum (introducing a high frequency cut-off) as opposed to a pure power law.

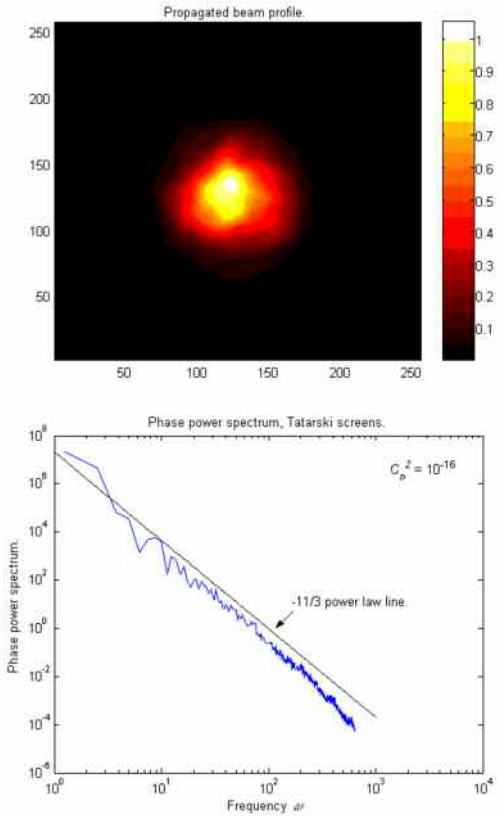

Figures 5.39 and 5.40, $C_n^2 = 10^{-16}\text{m}^{-2/3}$. The phase power spectrum follows a -11/3 power law and has a slight drop-off at high frequencies.

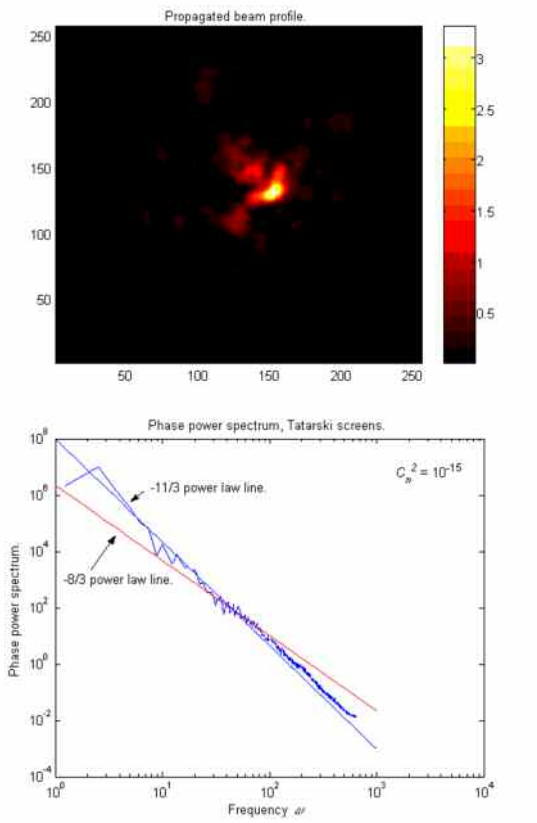

Figures 5.41 and 5.42, $C_n^2 = 10^{-15}m^{-2/3}$. The phase power spectrum follows a -8/3 power law, this is similar to what was seen in figure 37.

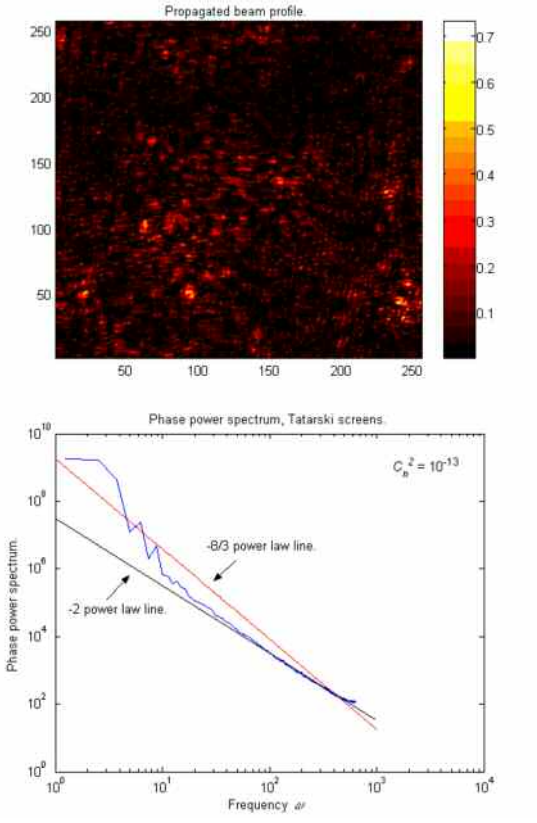

Figures 5.43 and 5.44, $C_n^2 = 10^{-13}\mathrm{m}^{-2/3}$. The phase power spectrum follows a -2 power law at high frequencies.

Figures 5.43 and 5.44 show the result of a strongly turbulent propagation geometry. Once more, a -2 power law is observed in the power spectrum (figure 5.44) at high frequencies.

5.7.5. Gaussian beams in a single phase screen limit.

Hitherto in this chapter, simulations have made exclusive use of extended media modelled by multiple phase screens as discussed earlier. It is interesting to look for a physical interpretation of the presence of the $-11/3$ power law behaviour in the temporal frequency spectra of propagated beams. The most interesting aspect of this behaviour is that it seems to be that it is restricted to a Gaussian beam and is independent of the form of the spectrum of refractive index fluctuations. The work of Ishimaru and Clifford has been expanded to show that they both correspond to different limits of the same effect (section 5.6). Consider now a physical explanation for the differences, and a reason why this behaviour disappears in the case of plane or spherical waves.

Consider a simple Huygens Fresnel formulation for wave propagation similar to that used in section 4.1.1. The electric field is

$$E(r,t) = \frac{ik}{2\pi z}\int_{-\infty}^{\infty} \exp\left(\frac{-ik|r-r'|^2}{2z}\right)\exp\left(-\frac{r'^2}{W_0^2}\right)\exp(i\phi(r',t))d^2r' \qquad (5.24)$$

where a TEM_{00} Gaussian beam of width W_0 has been included, other symbols are defined in section 4.1.1. Consider the small $\phi(r')$ limit

$$E(r,t) = \frac{ik}{2\pi z}\left\{\int_{-\infty}^{\infty} \exp\left(\frac{-ik|r-r'|^2}{2z} - \frac{r'^2}{W_0^2}\right)d^2r' + i\int_{-\infty}^{\infty} \exp\left(\frac{-ik|r-r'|^2}{2z} - \frac{r'^2}{W_0^2}\right)\phi(r',t)d^2r'\right\}$$

where the first integral is independent of time and therefore becomes a δ-function when taking the temporal Fourier transform. Considering the second integral, one can make a co-ordinate substitution (equation 4.5) and simplify by assuming that the screen and beam are 1-dimensional (in x) while measuring the field at the centre of the beam where $x = 0$; this gives

$$E(x=0)=\frac{(1-i)}{2}\sqrt{\frac{k}{\pi z}}\int_{-\infty}^{\infty}\exp\left(\frac{-ikx'^2}{2z}-\frac{x'^2}{W^2}\right)\phi(x')dx'. \tag{5.25}$$

Now transform to temporal co-ordinates and take the Fourier transform to give the power spectrum of the field. Proceeding in a similar vein to section 4.1.1 gives

$$\int_{-\infty}^{\infty}E(t)\exp(-i\omega t)dt=\frac{(1-i)}{2}\sqrt{\frac{k}{\pi z}}\int_{-\infty}^{\infty}dx'\int_{-\infty}^{\infty}dt\exp\left(\frac{-ikx'^2}{2z}-\frac{x'^2}{W^2}-i\omega t\right)\phi(x'+vt) \tag{5.26}$$

where v is the speed of the motion of the phase screen across the wave front. Now perform a co-ordinate transform $x'+vt\rightarrow x''$, giving

$$\hat{E}(\omega_t)=\frac{(1-i)}{2}\sqrt{\frac{k}{\pi z}}\left\{\int_{-\infty}^{\infty}\phi(x'')\exp(-\omega_x x'')dx''\int_{-\infty}^{\infty}dt\exp\left(\frac{-ik(x''-vt)^2}{2z}-\frac{(x''-vt)^2}{W^2}\right)\mathrm{K}\right.$$
$$\left.\mathrm{K}\exp(-i[\omega_t t-\omega_x x''])\right\}$$

where $\hat{E}(\omega_t)$ is the Fourier transform of the field. Integrating gives

$$\hat{E}(\omega_t)=\frac{(1-i)}{2}\sqrt{\frac{k}{\pi z}}\hat{\phi}(\omega_t)\frac{\sqrt{\pi}}{\sqrt{\frac{ik}{2z}+\frac{1}{w^2}}}\exp\left\{\frac{-\omega_t^{\,2}}{4v^2\left(\frac{ik}{2z}+\frac{1}{w^2}\right)}\right\} \tag{5.27}$$

where $\hat{\phi}(\omega_t)$ is the Fourier transform of the phase screen. Consider now the power spectrum of the field in two different limits of the width of the beam, a Fraunhofer limit and a limit in which the curvature of the beam is important.

Case I, $\frac{z}{kw^2} >> 1$.

This limit implies a far field regime, i.e. the propagation distance *z* is very large. In this regime the width of the beam is much smaller than the Fresnel zone, meaning that the field is comparable to a point source. In the far field a spherical wave emanating from a point source resembles a plane wave. Calculating the power spectrum of the field in this limit gives

$$S_E(\omega_t) = \left|\hat{E}(\omega_t)\right|^2 = \frac{kw^2}{2z}\left|\hat{\phi}(\omega_t)\right|^2 \exp\left(-\frac{w^2\omega_t^2}{2v^2}\right) \tag{5.28}$$

At large frequencies ω_t the spectrum of the field will be proportional to the spectrum of the phase screen, modified by a term depending on the propagation parameters *z*, *k* and *W*.

Case II, $\frac{z}{kw^2} << 1$

Here the beam width is larger than the Fresnel zone. Turbulence passing into and out of the beam will produce an effect in the power spectrum in the far field, this in addition to the turbulence passing through the beam. Using this limit gives

$$S_E(\omega_t) = \left|\hat{E}(\omega_t)\right|^2 = \left|\hat{\phi}(\omega_t)\right|^2 \exp\left(-\frac{z^2\omega_t^2}{v^2k^2w^2}\right) \tag{5.29}$$

where in contrast to (5.28) the *z*-dependence of the spectrum is contained within the exponential term.

Case II describes the Gaussian beam simulations performed in sections 5.7.3 and 5.7.4. Consider if the condition stipulated in Case II were to hold along the entire length of the beam, equation (5.29) can then be integrated over *z* (i.e. considering an extended medium rather than a single screen approx), such that

$$S_E(\omega) = \int_0^L \left|\hat{\phi}(\omega)\right|^2 \exp\left(-\frac{z^2\omega^2}{v^2k^2w^2}\right)dz = \left|\hat{\phi}(\omega)\right|^2 \sqrt{\frac{\pi}{2}}\frac{vkw}{\omega} erf\left(\frac{L\omega}{wkv}\sqrt{2}\right) \tag{5.30}$$

where the error function is defined by $erf(x) = \frac{2}{\sqrt{\pi}}\int_0^x \exp(-t^2)dt$. The error function can be approximated to unity if $x \approx 1$, given that Case II assumed $\frac{z}{kw^2} << 1$, large frequencies are required for this condition to hold. In this regime one can write

$$S_E(\omega) \approx \left|\hat{\phi}(\omega)\right|^2 \sqrt{\frac{\pi}{2}}\frac{vkw}{\omega} \sim \left|\hat{\phi}(\omega)\right|^2 \omega^{-1}. \tag{5.31}$$

Compare this result to equation (4.9) which showed how the power spectrum in the far field is modified by an oscillatory term in the frequency ω. Here the far field spectrum proportional to the phase screen spectrum multiplied by ω^{-1}. Thus, given that the spectrum of the phase screen data will have a $-8/3$ power law behaviour, it follows that the propagated field will have a spectrum with a $-11/3$ power law.

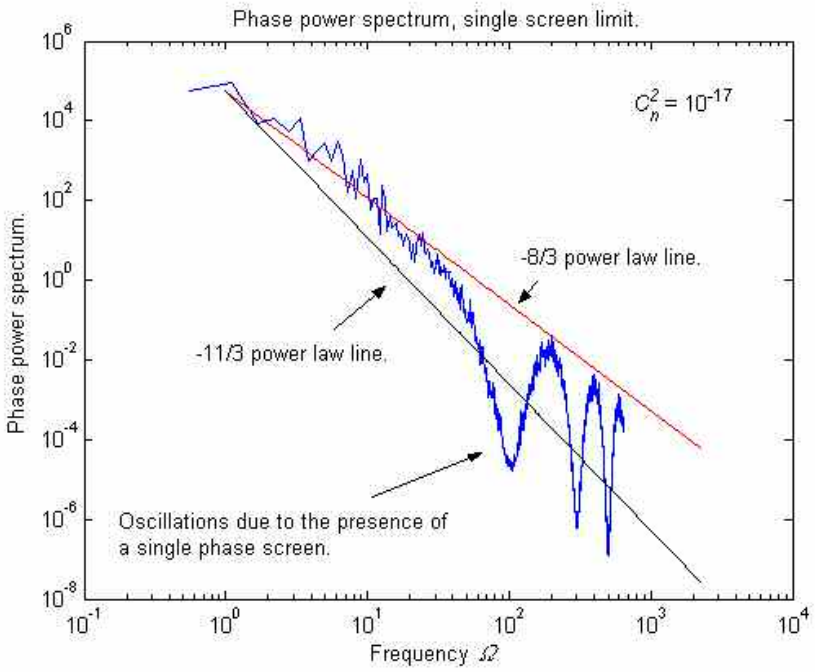

Figure 5.45. The phase power spectrum using the same parameters as figure 5.34 and a single phase screen instead of an extended medium.

The important thing to note in the derivation of equation (5.31) is that it requires an extended medium. Enforcing this condition assured that the result cannot hold in the case of a single phase screen. Thus one expects the $-8/3$ power law to hold in the case of a single phase screen, even when using a Gaussian beam (see figure 5.45 above).

Figure 5.45 shows a phase power spectrum plot taken from a simulation that used the same parameters as the simulation given in figure 5.34, the only difference being the use of a single phase screen rather than multiple phase screens to represent a turbulent layer. Note the appearance of a $-8/3$ power law behaviour modified by an oscillatory term, this is similar to what has been seen in the two-dimensional case (section 4.1.2). Therefore the presence of a $-11/3$ power law behaviour in the power spectrum is not only a feature of a beam (in contrast to a plane or spherical wave) but also a feature of an extended medium in contrast to a single phase screen (see figures 2.2 through to 2.9).

5.8. Experimental Results.

Modern experimental techniques allow the investigation of the structure of atmospheric turbulence by looking at the phase properties of a received laser beam. A heterodyne detection system can investigate the phase fluctuations of the received wave front. Heterodyne means the mixing of 2 frequencies to produce an intermediate frequency. A heterodyne detector in a LIDAR system looks at a returned signal in which the phase contains a frequency shift based on the frequency of the output signal and that of any vibrations on the reflecting surface. The heterodyne system interprets received electromagnetic radiation and allows an operator to record the phase fluctuations straight on to an appropriately set-up computer. The laboratory apparatus keeps a ‘beat’ signal so that the demodulation process can retrieve the frequency information imparted by the reflecting surface and intervening turbulence. Any and all phase fluctuations in the apparatus, as well as those in the atmosphere and the target of interest, will effect the phase retrieved from the received field. It is

possible to eliminate such effects within the equipment as they occur on a very slow time scale in comparison with phase shifts imposed by turbulence.

It is only in recent times that accurate methods for measuring the received phase have been developed in the laboratory, therefore much of the theoretical work performed in the 1960s and 70s by Clifford and Ishimaru on the properties of the temporal frequency spectrum and other phase-related statistics has, until now, been buried in the literature for want of a practical application. Experimental work performed at the time of these analyses [51] were often restricted to the measurement of spatial phase differences between two receivers.

The work performed for this thesis has been done in collaboration with researchers at the department of optronics at Qinetiq. Their group has published several studies in which they have investigated the properties of phase fluctuations imparted on a beam by turbulence. A study in which a heater was used to simulate turbulence [76] investigated the structure function of the turbulence and the properties of the far field. Another study, which used an 80m outdoor single pass for a laser beam [77], looked at the properties of the phase difference (in spatial terms) and the phase derivative (in temporal terms). They report on the phase difference power spectra in which they note a familiar -8/3 power law behaviour as well as an unexplained -11/3 power law behaviour at high frequencies. It is interesting to look at these experimental results in the light of simulations performed in section 5.7.

Data is reported on that was taken on two specific dates over the winter months of 2003. On the 23rd of January strong turbulence was encountered, on the 10th of February the turbulence was much weaker. The experimental set up involved the use of a 1.55micron laser emitted from the laboratory window and propagating to a corner cube reflector mounted on a site atop a hill some 17.5km distant, thus the experiment constituted a 35km double pass. The reflected beam was then collected by a pair of probes, thus 2 channels of data were received for each double pass.

5.8.1. Intermediate / weak turbulence, 10th February 2003.

Data collected on the 10th of February 2003 shows signs of weak / intermediate turbulence, a sample phasor of this data is given in figure 5.46 below. By looking at the phase / log amplitude power spectrum and making some simple assumptions about the inner (~ 1mm) and outer scales (~ 1m) of the turbulence, one can approximate the strength of the refractive index structure constant to $3\times10^{-16} m^{-2/3}$ [31]. This level of turbulence is consistent with the above assertion of weak turbulence. Meteorological surveys indicate that the average wind speed on this day was v = 2.2 ms^{-1}. The scintillation indices were calculated as 1.9379 and 2.5865 for the two channels.

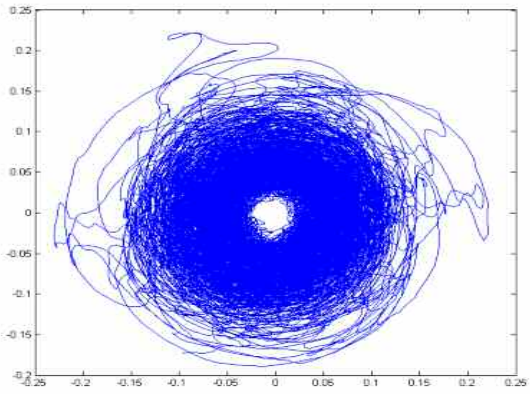

Fig. 5.46, sample phasor of one channel. Real and Imaginary parts of the field shown.

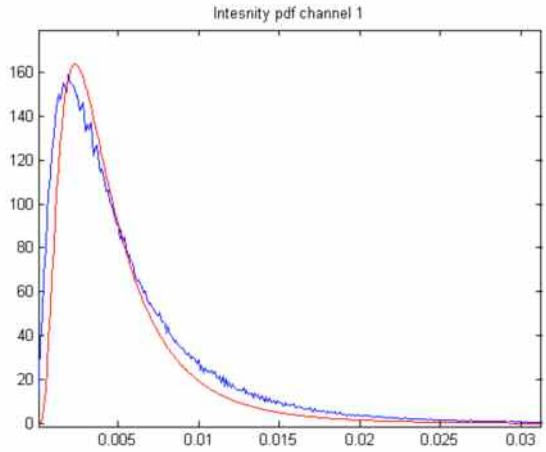

Fig. 5.47, the probability density function for the intensity of the data from 1 channel.

Figure 5.47 gives a log / linear plot of probability density function of the intensity, a log-normal curve (equation 2.28) has been fitted to the experimental data. The shape of the pdf of the phase derivative in figure 5.48 (below) is consistent with figure 2.7. Both these figures are consistent with the fact that weak turbulence was present on the 10th of February.

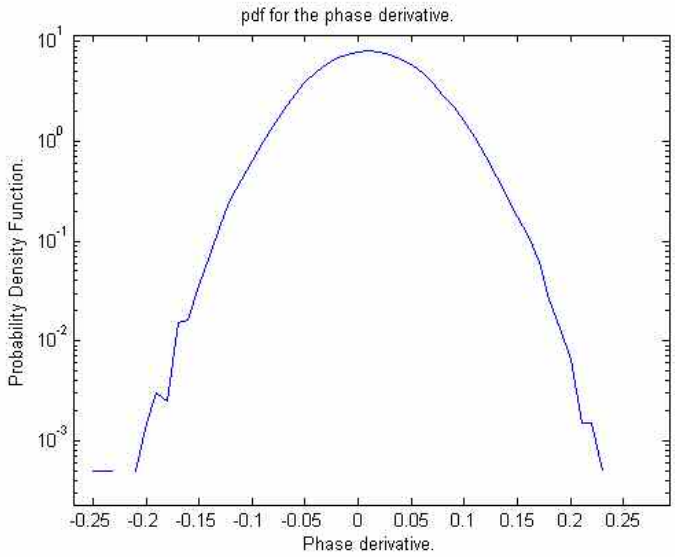

Figure 5.48, the probability density function of the phase derivative.

Figures 5.47 and 5.48 are exactly what one might expect from weak turbulence. One can look at information contained within the phase by calculating the power spectrum of the phase derivative. A comparison of the spectra produced by using the phase derivative and the *J* statistic show the effects of smoothing produced by intensity weighting that have been predicted [16, 76].

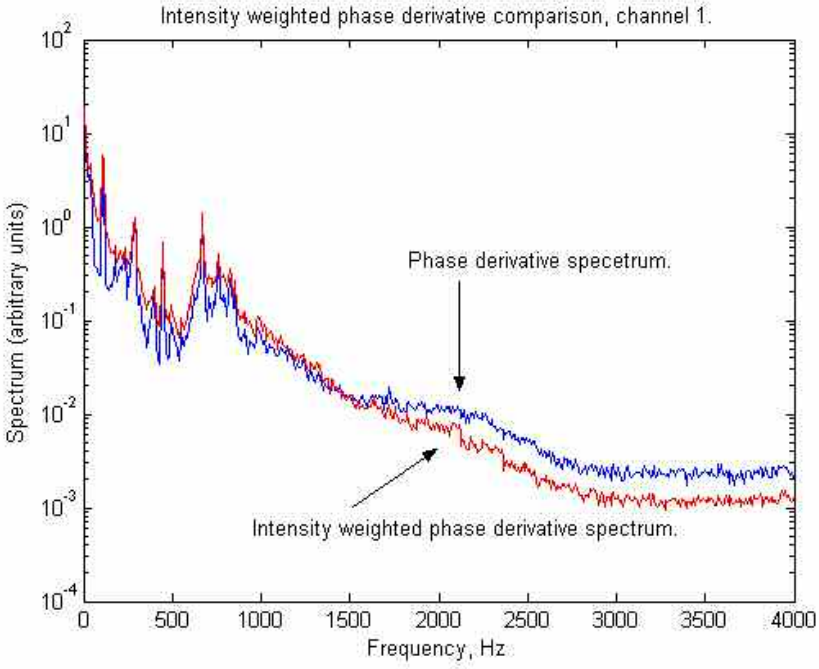

Figure 5.49, comparison between the phase derivative spectrum and the *J* spectrum.

Figure 5.49 indicates a smoothing of noise sources at high frequencies, i.e. the noise floor in the spectrum is lower and effects at high frequencies will be easier to detect. It is clear also from figure 5.49 that there are no high frequency artefacts in the data while several spikes are prominent in the frequency domain below 1kHz.

5.8.2. Strong turbulence, 23rd January 2003.

Data collected on this date show evidence of strong turbulence, figure 5.50 indicates a sample phasor of the data obtained on the 23rd of January 2003.

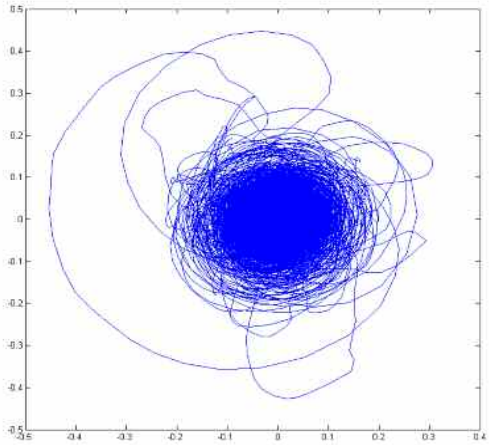

Fig 5.50: Strong turbulence indicated by the 'filling in' of the gap in the phasor's centre.

The level of the scintillation index was very high on this day, calculated values were 17.5943 and 13.3127 for the two channels. Several explanations for this level of scintillation have been suggested, one involves a possible misalignment in the optical receiving equipment. A second is that the experiment was performed at a height above ground (10m) such that turbulent layers between the ground and higher levels of the atmosphere were causing effects as yet unaccounted for. It is also possible that a double pass geometry through very strong turbulence caused such high scintillation levels. Figures 5.51 and 5.52 indicate log / log and log / linear plots the pdf of the intensity. Theoretical K – distributions are plotted alongside the pdfs; the K – distribution was proposed by Jakeman and Pusey [60, 79] as a model for intensity fluctuations in many different turbulent systems including thermal plumes [80] and sea echoes [60]. The intensity under a K-distribution is described by

$$P(I) = \frac{b}{\Gamma(\nu)\sqrt{I}}\left(\frac{b\sqrt{I}}{2}\right)^{\nu} K_{\nu-1}\left(b\sqrt{I}\right) \tag{5.32}$$

where K_n is a modified Bessel function of the second kind and b and ν are related to the moments of the intensity [79].

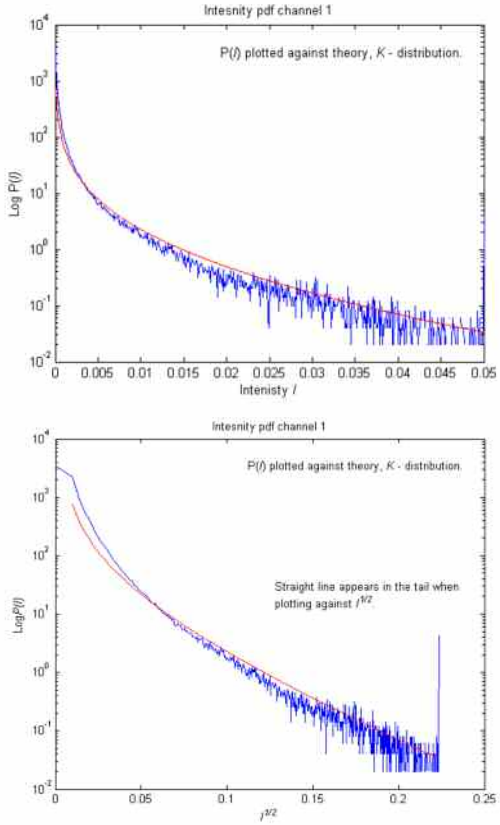

Figures 5.51 and 5.52, log / linear plots of I and $I^{1/2}$ against P(I).

Figure 5.51 shows good agreement between experiment and theory, looking at the tails of the distribution in figure 5.52 one can see a straight line when plotting against $\sqrt{I}$, this is the behaviour expected of the K – distribution for large I.

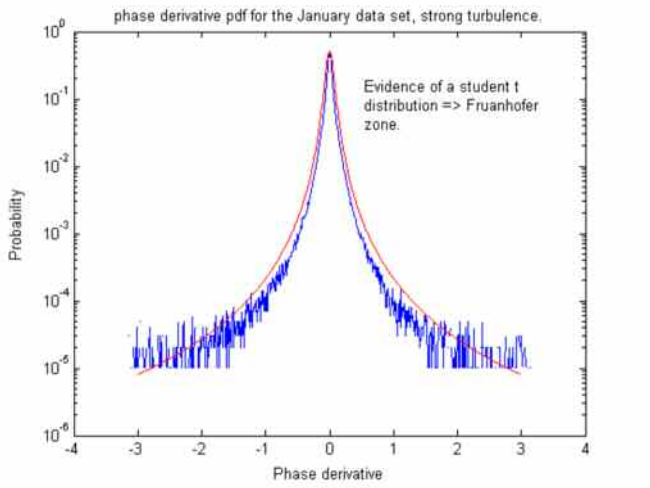

Figure 5.53 a log / linear plot of the phase derivative.

In figure 5.53 the pdf of the phase derivative is approximated reasonably well by a student - *t* distribution (equation 1.10). This is a characteristic of Gaussian statistics. Figures 5.51 and 5.52 show that the statistics are not Gaussian, it is well known [76] that the student - *t* behaviour in the phase derivative is not restricted to a Gaussian process. It is possible that a regime corresponding to *K* – distributed noise also yields student - *t* statistics in ϕ.

The most interesting result arising from the stronger turbulence is a comparison between the phase derivative spectra given in figure 5.54 (below). The noise floor for the intensity weighted phase derivative is much lower than that of the un-weighted statistic. This is what was expected. Frequency information that would be swamped under strong turbulence will be visible when using intensity weighting, this corroborates what was seen in [76].

Note a strong spike in the spectrum at approximately 100Hz, this indicates a feature in the frequency data which will be visible in spectra presented in the next section.

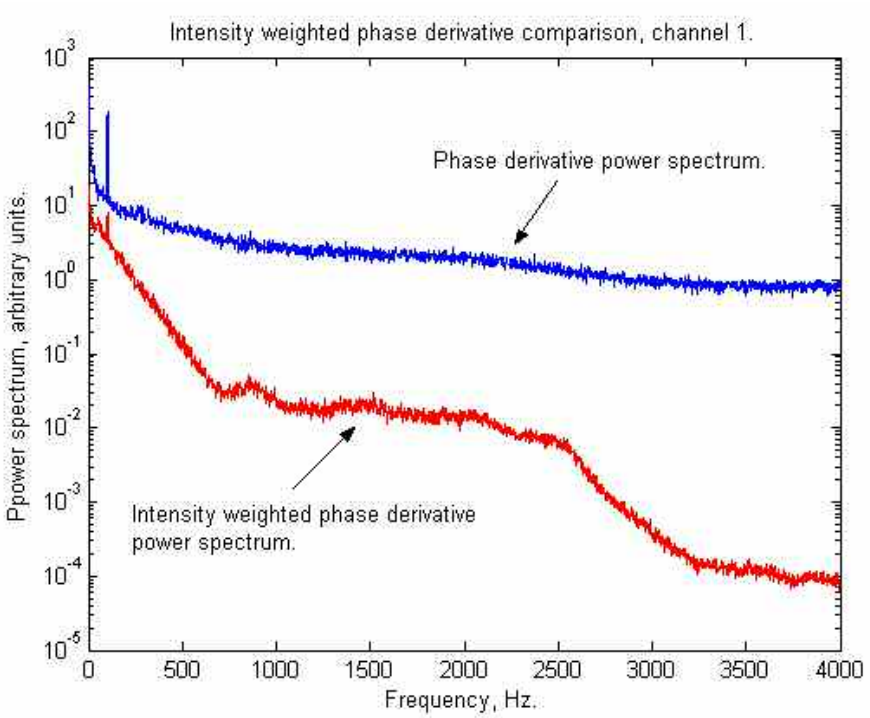

Fig. 5.54, comparison between the spectra of the phase derivative and the intensity weighted phase derivative.

5.8.3. Phase power spectra.

The received laser beam was sampled at a rate of 8000 samples per second. The January data set contains 3×10^6 points while the February data set contains approximately 1×10^7 points. Using the sampling rate one can calculate the phase power spectrum and look at the distribution of the power across the frequencies in the beam. A Hanning window (figure 3.14) is used to remove spurious high frequency elements while a linear interpolation method was used to reduce the effects of problems associated with the heating of the laboratory equipment.

Figure 5.55 shows the phase power spectrum for the data collected under strong turbulence. Note a $-8/3$ power law behaviour in the spectrum across the majority of the frequencies incorporating a very small -2 power law tail at high frequencies. The strength of the turbulence has smoothed out a lot of noise which is often seen in the

spectrum. The spike at 100Hz is attributed to vibrations present in the laboratory equipment. This was present in all simulations and was probably the result of some systematic influence on the LIDAR equipment in the laboratory.

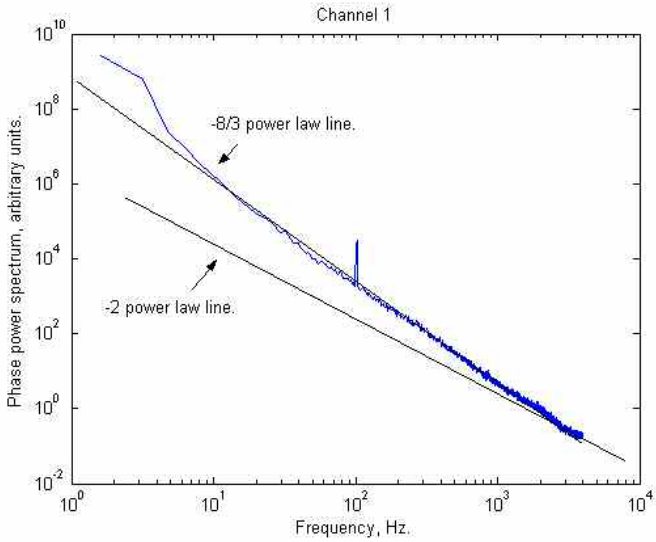

Fig. 5.55, The phase power spectrum for the January (stronger turbulence) data set.

Figure 5.56 (below) shows the phase power spectrum calculated for the weaker turbulence. Here it is possible to see more noise in the spectrum, this is manifested in the presence of many more spikes in the data than in figure 5.55. This shows how various vibrations and frequencies in the equipment and reflecting surface are being picked up by the beam and transferred into the receiving devices. This is the essence of LIDAR.

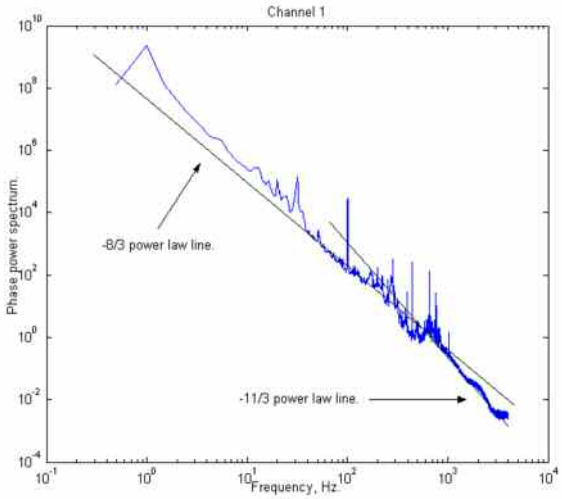

Fig. 5.56, the phase power spectrum for the February (weaker turbulence) data set.

Crucially one can see the appearance of a -11/3 power law behaviour in the high frequency regime of the spectrum, this corresponds to the computer simulation results of beam propagations under weak turbulence conditions (section 5.7.4, and below in section 5.8.4). A peak in the phase power spectrum remains in the first couple of points in the plot, this is despite the removal of spurious low frequency heating effects from the data.

5.8.4. Conclusions.

The data collected and analysed in this section have given a number of useful insights into the challenges facing numerical simulation of beam propagation. Data was collected on a day when weak turbulence was expected, plots of the pdf of the intensity (figure 5.47) phase derivative (figure 5.48) clearly indicate a weak turbulence regime, as indeed does the limited impact of the intensity weighting on the phase derivative spectrum (figure 5.49). It has been suggested, however, that a slight mis-alignment in the receiver optics may cast some doubt over the validity of the pdf plots

The second set of data concerned much stronger levels of turbulence; an attempt to estimate the strength of the turbulence by calculating σ_I^2 has given unusually high values. The plot for the pdf of the phase derivative (figure 5.53) gives a good match to a student - *t* distribution while the plots of the pdf for the intensity (figures 5.51 and 5.52) show a correlation with a K – distribution (equation 5.32).

Both phase power spectra (figures 5.55 and 5.56) show evidence of a $-8/3$ power law over a range of frequencies. Figure 5.56 shows a tendency to a $-11/3$ power law at approximately 300 or 400 Hz. There is also a clear shift at about 30Hz which could be due to Clifford's '½' (section 4.2.1), although $\omega_c \approx 4\,\text{Hz}$ based on the parameter values used in the experiment. Note also the presence of a large amount of power at low frequencies; something which, as already noted, is absent in the Von Karman model for atmospheric turbulence. One can conclude that any model using long rectangular phase screens to simulate temporal variation in frozen-in turbulence, without using the subharmonic technique, will be inaccurate at low frequencies. The

subharmonic fast Fourier transform technique replaces (or 'fills in') these lost low frequency components.

The phase power spectrum calculated for the weak turbulence (figure 5.56) can be compared with results from section 5.7.4, in which a Tatarski spectrum was used correcting for low frequencies with the subharmonic technique. Figures 5.42 and 5.44 give spectra using parameters very similar to those found on the day of the experiment (albeit over a shorter distance). Note figure 5.43 in particular and the behaviour of the power law regimes in the plot; the $-8/3$ power law becomes a $-11/3$ law at high frequencies while still retaining a lot of power at low frequencies. The equivalent simulation for a pure power law Kolmogorov (figure 5.36) shows the spectrum returning to a $-8/3$ power law at high frequencies. The experimental evidence presented here leads to the conclusion that the Tatarski spectrum plus a subharmonic addition at low frequencies provides a reasonably accurate description of the atmospheric turbulence on that day. It seems unlikely that any further detail can be wrung out of the experiment data with regard to the atmospheric structure. There is simply too much acoustic noise at high frequencies.

Considering the strong turbulence; the experimental evidence shows the possibility of a -2 power law at very high frequencies. The spectrum, however, bears little resemblance to any of the strongly turbulent simulations in section 5.7. This could be due to a possible misalignment of equipment or the presence of an as-yet unknown atmospheric effect.

5.9. Conclusions to chapter 5.

This chapter has provided a wide ranging review and investigation into the role of temporal phase statistics in coherent imaging systems. The use of Gaussian beams in such systems was considered, a number of numerical simulation techniques were developed. The use of rectangular screens (section 5.4) provides a novel method of simulating motion of frozen-in turbulence in an extended medium or a single screen approximation. A natural limitation on these screens has been successfully corrected

for by using an alternative fast Fourier transform algorithm to introduce missing low frequency components into the phase screen data (section 5.5).

Section 5.3.2 looked at spreading and wander in 3 dimensional beam simulations. The single screen limit was shown to be appropriate for modelling the spreading and wander of a Gaussian beam. The importance of the outer scale on beam wander was also verified.

The most interesting results in this chapter concern the temporal frequency spectrum. The theoretical developments of both Clifford and Ishimaru have been compared and contrasted. Each theory was shown to apply in an extended medium while a single screen approximation is inadequate. It has been shown, by considering Clifford's calculation (section 5.6.2) with a Tatarski spectrum, that a $-11/3$ power law in the temporal frequency spectrum arises from the use of a Gaussian beam rather than a Tatarski spectrum. It was initially thought that the $-11/3$ power law may in fact be a facet of the inner scale cut-off introduced into the Tatarski spectrum. The plane and beam solutions to the paraxial approximation differ fundamentally in their temporal frequency statistics regardless of the form of the spectrum of refractive index fluctuations. Simulation results in sections 5.7.2 and 5.7.4 agree with this assertion in that both show results of simulations using Tatarski spectra, only the beam wave simulations give a $-11/3$ power law, plane waves result in a $-8/3$ power law. Results of simulations using a Gaussian beam under differing turbulence models (sections 5.7.3 and 5.7.4), all give a $-11/3$ power law under weak turbulence conditions.

Results in section 5.8 led to the conclusion that a Tatarski spectrum with a subharmonic correction is the best model for atmospheric turbulence when one expects the turbulence to be weak. Simulation results using strong turbulence are more difficult to interpret in the light of the experimental evidence. Several simulations (sections 5.7 and 4.3) have indicated the possibility of a -2 power law in the phase power spectrum under strong turbulence condition. Given that there are no theoretical results with which to compare simulations, and that the experimental data

shows only minor evidence of -2 power law behaviour at high frequencies, the possibility of aliasing effects needs to be addressed.

Consider a simple calculation involving beam wander. Belmonte [7] gives the beam wander β of a Gaussian beam as the difference between the long and short term beam width (see section 5.3.1). Assuming a Kolmogorov pure power law allows for an approximation for wander to be written as

$$\beta = \frac{2z}{k\rho_0}\left\{0.52\left(\frac{\rho_0}{W_0}\right)^{1/3} - 0.26^2\left(\frac{\rho_0}{W_0}\right)^{2/3}\right\}^{1/2}, \tag{5.33}$$

where each of the terms above is as defined in section 5.3. It is known that aliasing will occur if a part of the beam is diffracted to such an extent that it exits the edge of the simulation and (due to the periodic nature of the fast Fourier transform algorithm) re-enters the simulation to interfere with itself again. One might expect this to happen if the beam wander is of the order of the aperture width. In all simulations in section 5.7, a beam of width 7cm and an aperture of width 40cm were used. Restricting the wander of the beam to be less than 40cm, allows a condition

$$0.5 \geq \left(C_n^2\right)^{1/2} z^{3/2}\left\{1.26 - 0.57\left(C_n^2\right)^{-1/5} k^{-2/5} z^{-1/5}\right\}^{1/2} \tag{5.34}$$

to be defined which must be met such that aliasing will not occur. Applying (5.34) to the most strongly turbulent simulations in sections 5.7.3 and 5.7.4 (i.e. λ = 1μm, z = 4km, C_n^2 = 10^{-13}m$^{-2/3}$) shows that all simulations are well within this limit[16]. Therefore is should be possible to rule aliasing out as a causal factor for the -2 power law behaviour.

At present it is unclear if such power law behaviour might become apparent in experiments that use higher levels of turbulence, or indeed if there exists some fundamental shift in the behaviour of temporal statistics under strong turbulence that

[16] Specifically, using the constants given, equation (5.34) yields 0.5 > 0.0868.

is unaccounted for in current theories of atmospheric turbulence. Further experiment is required in order to resolve such differences.

6: Conclusions.

This thesis has looked at analytical, numerical and experimental methods for modelling coherent imaging systems, including LIDAR and remote sensing devices that employ coherent radiation sources. Although both amplitude and intensity statistics have been looked at, the work has concentrated upon phase and phase derivative statistics. This has been motivated by modern heterodyne detection techniques which allow for the accurate collection of temporal phase data in coherent imaging. In comparison to the quantity of material in the literature on amplitude statistics, there is comparatively little on temporal phase statistics. A number of numerical techniques for the simulation of temporal statistics in wave propagation problems have been designed and developed in this thesis. Results of simulations have compared favourably with experiment and theory.

This thesis has provided an overview and validation of the numerical simulation process by building on previous work and looking at different statistical measures (including moments and probability density functions) in different propagation regimes. A major development in this thesis has been the use of phase screens to allow the simulation of temporal motion in Taylor's frozen-in turbulence hypothesis. The problems of temporal variation in three-dimensional simulations were addressed in sections 5.4 and 5.5 rectangular phase screens were used with low frequency information being supplemented by a subharmonic technique. These phase screens were then used in the simulation of plane and beam wave propagation.

In chapter 3 the properties of the phase derivative and related measures in weak turbulence were investigated by modelling the field in the Fraunhofer zone as a Rician process. This was shown to be a successful model in the case of a plane wave by looking at a comparison between simulation and theory. Expressions were derived, based on this model, for the correlation function of the phase derivative and the normalised second moment of J (sections 3.2 and 3.3 respectively). A relationship has also been found between the behaviour of ϕ and marginal fractal distributions.

A new development has been the use of multiple phase screens to represent a temporally varying extended medium. The single phase screen approximation is unrealistic when considering temporal statistics, as phase fluctuations occur throughout the length of the propagation path as the beam evolves rather than being imposed before any diffraction / refraction effects. Experimental work has shown that amplitude statistics under strong atmospheric conditions (section 5.8.2) differ from what was predicted under simple phase screen assumptions (section 2.5.1). Under real turbulence a *K*-distribution is a better approximation to the intensity statistics than the negative exponential saturation regime predicted in the case of a simple Gaussian correlated random process. Notable differences between the single screen approximation and experiment occur when one looks at the differences between the spectral representations of various statistics. Section 4.1 showed how the use of a single phase screen resulted in an oscillatory behaviour in the phase power spectrum; work in chapter 5 has shown that this is un-physical. In addition, the power law behaviour seen in the case of a Gaussian beam (section 5.6) is only present in the case of an extended medium, and disappears when one uses a single screen approximation.

Various models of atmospheric turbulence have been compared and contrasted. It was shown that the Van Karman model puts unnecessary restrictions on the outer scale of the turbulence (section 5.5) while the pure power law Kolmogorov model does not adequately sample frequencies outside the inertial subrange (section 2.2). The Tatarski spectrum (equation 5.16) provides the best model, for the purposes of simulating power spectra, in that it includes an inner scale cut-off while the absence of low frequency power can be accounted for by the use of additional subharmonics (section 5.8.4). Andrews [81] has suggested an alternative form for the refractive index spectrum based on Clifford and Hill's [27] evidence of a 'bump' at high frequencies. It would not be difficult to investigate this in a future study.

These simulations have agreed strongly with the assertion of several theoretical and experimental studies, which suggest that the phase power spectrum should exhibit a $-8/3$ power law in the inertial subrange of frequencies. They also agree with Ishimaru's calculation [71, 72] on the differences between plane and beam waves in the spectral form of the phase / log amplitude obtained. It is not the case that

Ishimaru used a Tatarski spectrum (as opposed to a pure power law) in his calculation that results in a $-11/3$ power law; rather, the fact that a Gaussian beam was used rather than a plane or spherical wave (section 5.6). The appearance of an unexplained -2 power law in the phase power spectrum has been noted at high frequencies when using strong levels of turbulence. This is visible only in a limited form in experimental data although it is prominent in many simulations. It has been postulated that this result is not the effect of aliasing or some equivalent problem due to the periodic nature of the fast Fourier transform process, and therefore that it is a genuine artefact of very strong turbulence conditions.

There are several avenues for further work in this field. More work is required on the effect of strong turbulence on coherent radiation; an explanation for the discovery of a -2 power law in the phase power spectrum under such conditions is strongly desirable so that one might understand the physical processes causing it. There are further applications of the work in coherent imaging; LIDAR systems of the type used in the experiments operate on the principle of a double pass of a coherent beam which has been reflected from a vibrating surface. Similar numerical simulation work to that presented here could be performed for a double pass through frozen-in turbulence with a receiver at the same location as the emitter. It has been shown (section 4.1.2) that one can demodulate a single constant frequency offset from the phase power spectrum and it should be possible to demodulate a more general signal using the same technique in addition to intensity-weighting. This is important in the recovery of a range of frequencies from a vibrating target.

Appendix A.

The phase power spectrum, $S_\phi(\omega)$, is defined as being the Fourier transform of the correlation function $B_\phi(\rho)$, where ω is a frequency and ρ a length parameter representing the distance between two points in the observation screen. The relationship between these quantities was formalised by Tatarski [36], giving

$$S_\phi(\omega) = 4\int_0^\infty \cos[2\pi\omega\rho] B_\phi(\rho) d\rho \,. \tag{A1}$$

We proceed in a similar vein to Clifford [30] and Lee and Harp [33], who calculated the phase power spectrum via $B_\phi(\rho)$, except that we employ a geometric optics formulation to provide the expression for the correlation function. The geometric optics formulation of wave propagation (for a field $u(x, y, z)$) ignores diffraction by making the simplifying assumption that the wavelength of the beam is much shorter than the inner scale of the turbulence, thus allowing a simplification of the wave equation (equation (2.3)) to

$$\nabla^2 u + k^2 n^2(r) u = 0 \tag{A2}$$

where u is any one of the three spatial components of the field, n is the refractive index and k is the wave number. Now assume $u = A\exp(i\phi)$ and perform perturbation theory on the amplitude A and phase ϕ. Tatarski [36] shows that one can develop an expression for the spectral density $F_\phi(\kappa,0)$ of the structure function $D_\phi(\rho)$ of the phase ϕ. The use of a pure power law Kolmogorov spectrum for the fluctuations of the refractive index (equation (2.14)) allows one to obtain $F_\phi(\kappa,0) = 0.21k^2 LC_n^2 \kappa^{\frac{-11}{3}}$.

$F_\phi(\kappa,0)$ is related to the correlation function $B_\phi(\rho)$ by

$$B_\phi(\rho) = 2\pi \int_0^\infty J_0(\kappa\rho) F_\phi(\kappa,0)\kappa d\kappa, \tag{A3}$$

where J_0 is the Bessel function of the first kind, order 0.

Thus the phase power spectrum is

$$S_\phi(\omega) = 5.28k^2 LC_n^2 \int_0^\infty \kappa^{\frac{-8}{3}} d\kappa \int_0^\infty J_0(\kappa\rho)\cos[2\pi\omega\rho] B_\phi(\rho) d\rho, \tag{A4}$$

and integrating over ρ gives

$$S_\phi(\omega) = 5.28k^2 LC_n^2 \int_0^\infty \left\{ \frac{\kappa^{\frac{-8}{3}}}{\left(\kappa^2 - [2\pi\omega]^2\right)^{\frac{1}{2}}} \right\} d\kappa. \tag{A5}$$

The lower limit of the integration here gives a singularity, changing the lower limit from 0 to $2\pi\omega$ (Clifford [30]) allows integration over κ, this gives

$$S_\phi(\omega) = 5.28Lk^2 C_n^2 \frac{\sqrt{\pi}}{2} \frac{\Gamma\left(4/3\right)}{\Gamma\left(11/6\right)} (2\pi\omega)^{\frac{-8}{3}} = 0.033Lk^2 C_n^2 \omega^{\frac{-8}{3}} \approx 4.43 L^{\frac{7}{3}} k^{\frac{2}{3}} C_n^2 \Omega^{\frac{-8}{3}},$$

after we have converted into Clifford's frequency notation $\Omega = \omega\sqrt{2\pi\lambda L}$.

This is the low frequency limit of Clifford's result (section 4.2.1), as required.

Appendix B.

The integration of (3.46) results in

$$\left\langle J^2 \right\rangle = \frac{-k^3 u^2}{8\pi z^3}\left\{\left[\frac{8\phi_0^2\pi z^3}{k^3\xi^2} + 2\pi\xi^4\phi_0^2 F_2(a)\right] + \mathrm{K} \right. \\ \left. \mathrm{K} + \frac{4z^2\pi\phi_0^2}{k^2}\left[2\phi_0^2 F_1(a) + \frac{8\phi_0^2}{\xi\left(\frac{4}{\xi^2}+\frac{k^2\xi^2}{z^2}\right)}\left\{\frac{4}{\left(\frac{4}{\xi^2}+\frac{k^2\xi^2}{z^2}\right)^{\frac{1}{2}}} - 1\right\}\right]\right\} \\ + \frac{8\phi_0^2\cos\left(\frac{1}{2}\tan^{-1}(f(a))\right)}{\left((4+a^2)+16a^2\right)^{\frac{1}{4}}} - \frac{4z}{k\xi^2}\Bigg] \Bigg\} \quad \text{(B1)}$$

where $a = k\xi^2/z$, $f(a) = 4a/4+a^2$ and the two functions F_1 (equation B2) and F_2 (equation B3) are defined by

$$F_1(a) = -\left\{\sqrt{a^2+24a+16}\cos\left(\frac{1}{2}\tan^{-1}(f(a))\right) + \left(4-a^2\right)\cos\left(\frac{3}{2}\tan^{-1}(f(a))\right) - \mathrm{K} \right. \\ \left. \mathrm{K}\, 4a\sin\left(\frac{3}{2}\tan^{-1}(f(a))\right)\right\} \Big/ \left(4+a^2\right)^{\frac{3}{2}}\left(1+f(a)^2\right)^{\frac{3}{4}}$$

and

$$F_2(a) = \frac{\left\{a^2\sqrt{1+\frac{16}{a^2}}\cos\left[\frac{1}{2}\tan^{-1}\left(\frac{4}{a}\right)\right] + \left(4-a^2\right)\cos\left[\frac{3}{2}\tan^{-1}\left(\frac{4}{a}\right)\right] - 4a\sin\left[\frac{3}{2}\tan^{-1}\left(\frac{4}{a}\right)\right]\right\}}{a^3\left(1+\frac{16}{a^2}\right)^{\frac{3}{4}}}$$

Appendix C.

We require a large ϕ_0 expansion of y_2 (equation 3.30). We need only consider the situation where $\tau' \approx 0$, as when $\tau' > 0$, both k and p tend to 0 and the fact that y_2 tends to 0 quickly follows. First re-write p (equation 3.31) and k (equation 3.32) by assuming a Gaussian correlation function

$$\rho(\tau) = \exp\left(-\tau'^2\right)$$

and $\phi_0 >> 1$, this results in

$$p = \exp\left(-\phi_0^2\right) \approx 0,$$

$$k \approx \frac{1-\tau'^2\phi_0^2 - \exp\left(-\phi_0^2\right)}{1-\exp\left(-\phi_0^2\right)} \approx 1-\tau'^2\phi_0^2$$

and

$$\frac{p}{k} = \frac{1}{\exp\left(-\phi_0^2\left[1-\tau'^2\right]\right)-1} \approx \exp\left(-\phi_0^2\left[1-\tau'^2\right]\right)$$

where we have assumed $\tau' << 1$. Now substituting these expressions into equation (3.30) and taking $\phi_0 >> 1$ gives

$$y_2 = -\exp\left(-\phi_0^2\left[1-\tau'^2\right]\right)\ln\left(1-k^2\right)-1+\frac{2}{\tau'^2\phi_0^2}\exp\left(-\exp\left(-\phi_0^2\right)\right)-\mathrm{K}$$

$$\mathrm{K}\,\frac{2-\tau'^2\phi_0^2}{\tau'^2\phi_0^2}\exp\left(\frac{-2\exp\left(-\phi_0^2\right)}{2-\tau'^2\phi_0^2}\right)$$

$$y_2 = 0-1+\frac{2}{\tau'^2\phi_0^2}\exp\left(-\exp\left(-\phi_0^2\right)\right)-\left(\frac{2}{\tau'^2\phi_0^2}-1\right)\exp\left(-\exp\left(-\phi_0^2\right)\left\{1+\frac{1}{2}\tau'^2\phi_0^2\right\}\right)$$

$$y_2 = -1+\frac{2}{\tau'^2\phi_0^2}-\left(\frac{2}{\tau'^2\phi_0^2}-1\right) = 0.$$

Bibliography.

1. H. Taub and D. L. Schilling, 'Principles of Communication Systems', (McGraw-Hill, 1986).
2. H.G.Booker, T.A.Ratcliffe and D.H.Schinn, 'Diffraction from an irregular screen with applications to ionospheric problems', Phil.Trans.Roy.Soc. A, **242**, 579-609, (1950).
3. R.P.Mercier, 'Diffraction by a screen causing large random phase fluctuations', Proc. Camb.Phil.Soc. A **58**, 382-400, (1962).
4. E. Jakeman, J.G. McWhirter, 'Correlation function dependence of the scintillation behind a deep random phase screen', J. Phys, A: Math. Gen. **10**, 1599-1643, (1977).
5. M Schwartz, 'Information transmission, modulation and noise.', (McGraw-Hill, 1990).
6. O Svelto, 'Principles of Lasers', 3rd Ed, (Plenum Press, 1993).
7. A. Belmonte, 'Feasibility study for the simulation of beam progagation: consideration of coherent lidar performance.' Applied Optics, **39**, 5426-5445, (Oct 2000).
8. J. M. Martin, S. M. Flatte, 'Simulation of point-source scintillation through three-dimensional random media.', J. Opt. Soc. Am., A **7**, 838-847 (1990).
9. K. D. Ridley, E. Jakeman, 'Incomplete phase conjugation through a random phase screen.' J. Opt. Soc. Am., A **13**, 2393-2402, (1996).
10. E. E. Salpeter, 'Interplanetary scintillations: Theory.' Astrophys. J. **147**, 433-448, (1967).
11. E. N. Bramley, 'Diffraction of an angular spectrum of waves by a phase-changing screen.' J. Atmos. Terr. Phys., **29**, 1-28, (1966).
12. Lord Rayleigh, 'On the resultant of a large number of vibrations of the same pitch and of arbitrary phase.' Phil. Mag. **10**, 72-78, (1880).
13. S. O. Rice, 'Statistical properties of a sine wave plus random noise.' Bell Syst. Tech. J. **27**, 109-157, (1948).
14. B. J. Uscinski, 'Wave propagation and scattering', (Oxford university, 1986).

15. J. M. Martin, S. M. Flatte, ‘Intensity images and statistics from numerical simulation of wave propagation in 3-D random media.’, Applied Optics, **72**, 2111-2126, (1998).
16. E. Jakeman, S. M. Watson, K. D. Ridley, ‘Intensity- weighted phase-derivative statistics.’, J. Opt. Soc. Am, **18**, 2121-2131, (Sept 2001).
17. J. F. Miller, K. Schatzel, B. Vincent, ‘The determination of very small electrophoretic mobilities in polar and non-polar colloidal dispersions using phase analysis light scattering.’ J. Colloid. Interface Sci. **143**, 532-554 (1991).
18. E. Parzen, ‘Stochastic Processes’, (Holden-Day, 1962).
19. C. Macaskill, T. E. Ewart, ‘Computer Simulation of Two-dimensional Random Wave Propagation.’, IMA J. Appl. Math. **33**, 1-15 (1984).
20. R. G. Lane, A. Glindemann, J. C. Dainty, ‘Simulation of a Kolmogorov phase screen’, Waves in random Media 2, 209-224, (1992).
21. S. Watson, ‘Frequency Demodulation in the presence of Multiplicative Speckle Noise.’, PhD Thesis 2002, University of Nottingham.
22. H. A. Priestley, ‘Introduction to Complex Analysis’, (Oxford University Press, 1985).
23. R. Frehlich, ‘Simulation of laser propagation in a turbulent atmosphere’, Applied Optics, **39**, 393-397, (Jan 2000).
24. J. C. Dainty, ‘Laser speckle and related phenomena’, (Springer-Verlag, 1975).
25. S. M. Flatte, J. S. Gerber, ‘Irradiance-variance behaviour by numerical simulation for plane-wave and spherical-wave optical propagation through strong turbulence.’, J. Opt. Soc. Am., **17**, 1092-1097, (June 2000).
26. H. Kogelnik, T. Li, ‘Laser Beams and Resonators’, Applied Optics, **5**, 1550-1567, (October 1966).
27. R. J. Hill, S. F. Clifford, ‘Modified spectrum of atmospheric temperature fluctuations and its application to optical propagation’, J. Opt. Soc. Am., **68**, 892-899, (July 1978).
28. A.M. Oboukhov, ‘Some specific features of atmospheric turbulence.’ Fluid Mechanics, **13**, 82-85, (1962).
29. A. N. Kolmogorov, ‘A refinement of previous hypotheses concerning the local structure of turbulence in a viscous incompressible fluid ad high Reynolds number.’ Fluid Mechanics, **13**, 77-81, (1962).

30. S. F. Clifford, ‘Temporal-Frequency Spectra for a Spherical Wave Propagating through Atmospheric Turbulence.’ J. Opt. Soc. Am., **61**, 1285-1292, (October 1971)
31. L. C. Andrews, R. L. Phillips, ‘Laser Beam Propagation through Random Media.’ (SPIE 1998).
32. I. S. Gradshteyn, I. M. Ryzhik, ‘Table of Integrals, Series and Products.’ (Academic Press 2000).
33. R. W. Lee, J. C. Harp, ‘Weak scattering in random media, with applications to remote processing.’ Proc IEEE, **57**, 375-378, (1969).
34. R. S. Lawrence and J. W. Strohbehn, Proc IEEE, **58**, 1523, (1970).
35. A. Ishimaru, ‘Wave Propagation and Scattering in Random Media’, (Academic Press 1978).
36. V. I. Tatarski, ‘Wave Propagation in a Turbulent Medium.’, (McGraw-Hill, 1961).
37. G. Sedmak, ‘Performance analysis of and compensation for aspect-ratio of fast-Fourier-transform-based simulations of large atmospheric wave fronts.’ Applied Optics, **37**, 4605-4613, (July 1998).
38. L. C. Andrews, R. L. Phillips, A. R. Weeks, ‘Propagation of a Gaussian-beam wave through a random phase screen.’, Waves in Random Media, **7**, 229-244, (1997).
39. V. V. Voitsekhovich, ‘Outer scale of turbulence: comparison of different models.’, J. Opt. Soc. Am. A., **12**, (June 1995).
40. R. J. Hill, G. R. Ochs, ‘Inner-scale dependence of scintillation variances measured in weak scintillation.’, J. Opt. Soc. Am. A., **9**, 1406-1411, (August 1992).
41. L. C. Andrews, R. L. Phillips, B. K. Shivamoggi, J. K. Beck, ‘A statistical theory for the distribution of energy dissipation in intermittent turbulence.’, Physics of Fluids A, **1**, 999-1006, (June 1989).
42. A. M. Prokhorov, F. V. Bunkin, K. S. Gochelashvily, V. I. Shishov, ‘Laser Propagation in Turbulent Media.’, Proc. IEEE, **63**, 790-811, (May 1975).
43. E. Azoulay, V Thiermann, A Jetter, A Kohnle, Z Azar, ‘Optical measurement of the inner scale of turbulence.’, J. Phys. D: Appl. Phys., **21**, S41-S44, (1988).

44. R. L. Fante, ‘Inner-scale size effect on the scintillations of light in the turbulent atmosphere.’, J. Opt. Soc. Am., **73**, 277-281, (March 1983).
45. R. G. Frehlich, ‘Intensity covariance of a point source in a random medium with a Kolmogorov spectrum and an inner scale of turbulence.’, J. Opt. Soc. Am. A., **4**, 360-365, (February 1987).
46. R. J. Hill, S. F. Clifford, ‘Theory of saturation of optical scintillation by strong turbulence for arbitrary refractive index spectra.’, J. Opt. Soc. Am., **71**, 675-686, (June 1981).
47. J. H. Churnside, R. J. Lataitis, ‘Wander of an optical beam in the turbulent atmosphere.’, Applied Optics, **29**, 926-930, (March 1990).
48. A. Hewish, ‘The diffraction of radio waves in passing through a phase-changing ionosphere.’ Proc. Roy. Soc. London. Ser. A, **209**, 81-96, (1951).
49. A. Hewish, ‘The diffraction of galactic radio waves as a method of investigating the irregular structure of the ionosphere.’ Proc. Roy. Soc. London. Ser. A, **214**, 494-514, (1952).
50. E. N. Bramley, ‘The diffraction of waves by an irregular refracting medium.’ Proc. Roy. Soc. London. Ser. A, **225**, 515-518, (1954).
51. S. F. Clifford, G. M. B. Bouricius, G. R. Ochs, M. H. Ackley, ‘Phase variations in atmospheric optical propagation.’ J. Opt. Soc. Am., **61**, 1279-1284, (October 1971).
52. H. T. Yura, ‘Short-term average optical-beam spread in a turbulent medium.’ J. Opt. Soc. Am., **63**, 567-572, (May 1973).
53. R. M. Measures. ‘Laser Remote Sensing.’ (Wiley-Interscience, 1984).
54. D. K. Evans ‘Laser applications in Physical Chemistry’ (New York, 1989).
55. J. L. Barrett, P. A. Budni, ‘Laser beam propagations through strong turbulence’ J. Appl. Phys. **71**, 1124-1127, (February 1992).
56. H. A. Whale, ‘Diffraction of a plane wave by a random phase screen.’ Journal of Atmospheric and Terrestrial Physics, **35**, 263-274, (1973).
57. R. Buckley, ‘Diffraction by a random phase-changing screen: A numerical experiment.’ Journal of Atmospheric and Terrestrial Physics, **37**, 1431-1446, (1975).
58. J. H. Churnside, R. J. Hill, ‘Probability density of irradiance scintillation for strong path-integrated refractive turbulence.’ J. Opt. Soc. Am. A., **4**, 727-733, (April 1987).

59. R. L. Phillips, L. C. Andrews, 'Universal statistical model for irradiance fluctuations in a turbulent medium.' J. Opt. Soc. Am., **72**, 864-870, (July 1982).
60. E. Jakeman, P. N. Pusey, 'A model for Non-Rayleigh Sea Echo.' IEEE trans. on antennas and propagation, **AP-24**, 806-814, (November 1976).
61. H. G. Booker, J. A. Ferguson, H. O. Vats, 'Comparison between the extended-medium and the phase-screen scintillation theories.', Journal of Atmospheric and Terrestrial Physics, **47**, 381-399, (1985).
62. E. N. Bramley, 'Accuracy of computing ionospheric radiowave scintillation by thin-phase-screen approximation', Journal of Atmospheric and Terrestrial Physics, **39**, 367-373, (1977).
63. H. G. Booker, G. Majidiahi, 'Theory of refractive scattering in scintillation phenomena.', Journal of Atmospheric and Terrestrial Physics, **43**, 1199-1214, (1981).
64. J. W. Goodman, 'Statistical optics.', (John Wiley & Sons 1985).
65. K. D. Ridley, E Jakeman, 'Signal-to-noise analysis of FM demodulation in the presence of multiplicative and additive noise.', Signal Processing, **80**, 1895-1907, (2000).
66. M. I. Toral , N. Lara, J. Narvaez, P. Richter, 'Screening of some transition metal ions and quantitative determination of copper, cadmium and zinc by solid phase derivative spectrophotometry', Journal of the Chilean Chemical Society, **49,** 163-168, (June 2004).
67. R. F. Lutomirski, H. T. Yura, "Propagation of a finite optical beam in an inhomogeneous medium.", Appl. Opt. **10**, 1652-1658 (1971).
68. R. Rao, S. Wang, X. Liu, Z. Gong, 'Turbulence spectrum effect on wave temporal-frequency spectra for light propagating through the atmosphere.', J. Opt. Soc. Am. A. **16**, 2755-2762, (November 1999).
69. A. Ishimaru ,'Wave Propagation and scattering in random media.', (Academic Prees, 1978).
70. A. Ishimaru, 'Temporal frequency spectra of multifrequency waves in turbulent atmosphere', IEEE Trans. Antennas Propagat. **AP-20**, 10-19, (1972).
71. A. Ishimaru, 'Fluctuations of a beam wave propagation through a locally homogeneous medium', Radio Science, **4**, 295-305, (1969).

72. A. Ishimaru, ‘Fluctuations of a Focused Beam Wave for Atmospheric Turbulence Probing.’, Proc. IEEE, **57**, 407-414, (April 1969).
73. B. Chytil, L Sumichrast, ‘Log-amplitude temporal frequency spectra of a beam wave propagating through weak turbulence.’, Optica Acta, **25**, 605-618, (1978).
74. V. P. Lukin, V. V. Pokasov, ‘Optical wave phase fluctuations.’, Applied Optics, **20**, 121-135, (1981).
75. A. Erdelyi, ‘Tables of Integrals Transforms.’, (McGraw-Hill, New York, 1959).
76. K. D. Ridley, S. M. Watson, E. Jakeman, M. Harris, ‘Heterodyne measurements of laser light scattering by a turbulent phase screen.’, Applied Optics, **41**, 532-542, (2002).
77. K. D. Ridley, E. Jakeman, D. Bryce, S. M. Watson, ‘Dual-channel heterodyne measurements of atmospheric phase fluctuations.’, Applied Optics, **42**, 4261-4268, (2003).
78. P. Coles, P. Dineen, J. Earl, D. Wright, ‘Phase correlations in cosmic microwave background temperature maps.’, Mon. Not. R. Astron. **350**, 989 – 1004, (2004).
79. E. Jakeman. ‘K – distributed noise.’, J. Opt. A., **1**, 784-789, (1999).
80. E. Jakeman, ‘Speckle statistics with a small number of scatterers.’, Proc. SPIE, **243**, 9-19, (1980).
81. L. C. Andrews, ‘An analytical model for the refractive index power spectrum and its application to optical scintillations in the atmosphere’, J. Mod. Opt., **39**, 1849-1853 (1992).
82. J. Strohbehn, ‘Laser Beam Propagation in the Atmosphere.’, (Springer, New York 1978).
83. M. V. Berry, ‘Diffractals.’, J. Phys. A: Math. Gen., **12**, 781-797 (1979).